EXPERIMENTAL AND COMPUTATIONAL STUDIES OF ARTICULAR CARTILAGE AT HIGH RESOLUTIONS

by

SYEDA S BATOOL

A dissertation submitted in partial fulfillment of the
requirements for the degree of

DOCTOR OF PHILOSOPHY IN BIOMEDICAL SCIENCES: MEDICAL PHYSICS

2023

Oakland University
Rochester, Michigan

Doctoral Advisory Committee:

Yang Xia, Ph.D., Chair
Bradley John Roth, Ph.D., Co-Chair
Susan Bowyer, Ph.D.
Steffan Puwal, Ph.D.
Alexey Tonyushkin, Ph.D.

Dedicated to
To my mother, and my late father

ACKNOWLEDGMENTS

My sincere gratitude and respect to my advisors Yang Xia Ph.D. and Bradley J. Roth Ph.D. for their valuable mentorship, guidance, and support. I am grateful to Susan Bowyer Ph.D., Steffan Puwal Ph.D., and Alexey Tonyushkin Ph.D. for being on my Doctoral Dissertation Committee and providing their useful feedback. I would also like to thank Rohit Mahar Ph.D. for MRI training; Adam Lauver Ph.D. (Michigan State University) for providing the stifles, Cliff Less D.V.M. Ph.D. for training on joint dissection, Farid Badar Ph.D. for guidance on imaging analysis, and Hannah Mantebea and Amanveer Singh for their valuable friendship and positive support in conducting experiments.

I am thankful to the National Institutes of Health (NIH) for the R01 grant (AR 069047), the Center for Biomedical Research and the Department of Physics at Oakland University for their funding and support which enabled me to pursue my dream to be part of scientific endeavor and advancement. I would also like to thank my family, husband, and in-laws for their unwavering support during this journey.

Syeda Saira Batool

ABSTRACT

EXPERIMENTAL AND COMPUTATIONAL STUDIES OF ARTICULAR CARTILAGE AT HIGH RESOLUTIONS

by

Syeda S Batool

Adviser: Yang Xia, Ph.D.

Articular cartilage is a thin layer of connective tissue covering the ends of bones in diarthrodial joints to minimize friction and distribute loads. The degradation of articular cartilage is the hallmark of osteoarthritis (OA), a complex joint disease that ranks as the number one cause of disability in the adult population. Conceptually, cartilage can be divided into three sub-tissue zones (the superficial zone SZ, the transitional zone TZ, and the radial zone RZ) across its thin thickness (depth), where each zone has a set of unique depth-dependent properties. These uneven structural and compositional variations across its thin thickness imply that any diagnostic technique should ideally have high resolution in imaging; otherwise, volume averaging within an image pixel could obscure any possibility of early disease detection. In this dissertation, we used quantitative microscopic magnetic resonance imaging (μMRI) combined with polarized light microscopy (PLM) to study the articular cartilage in rabbits and its potential use as an animal model for OA. The utilization of animals plays a vital role in OA research, which enables the examination of the degradation of OA before any procedures are used on humans in the clinic.

This dissertation has six chapters. Chapters 1 and 2 contain the introduction, the background, and the literature review. Chapter 3 is an experimental MRI and PLM study of rabbit cartilage at sub-10 μm resolution, which established quantitatively the baseline characteristics of healthy rabbit cartilage between μMRI and PLM. The results, which are useful for the future investigation of OA using the rabbit model, have been published in the *Journal of Orthopaedic Research* (Batool & Xia, 2020). Chapter 4 is an experimental study to characterize the structural variations at different anatomical locations of femoral cartilage in young rabbits (12-14 weeks old) using μMRI and PLM. Knowledge of location-specific structural differences in the collagen network over the joint surface can improve the understanding of local mechanobiology and provide insights into tissue engineering, and degradation repairs This study has been published in the journal *Cartilage* (Batool & Xia, 2022). Chapter 5 presents a computational study that used a mathematical model to describe the role of collagen fibril mechanics in articular cartilage under 1D axial compression. This study is being finalized for a peer-reviewed journal. The final Chapter 6 summarizes this dissertation.

TABLE OF CONTENTS

TABLE OF CONTENTS—Continued

TABLE OF CONTENTS—Continued

TABLE OF CONTENTS—Continued

TABLE OF CONTENTS—Continued

TABLE OF CONTENTS—Continued

LIST OF TABLES

LIST OF FIGURES

LIST OF ABBREVIATIONS

A	Anterior
AC	Articular cartilage
AS	Articular surface
C	Central
CBI	Cartilage Bone interface
CPMG	Carr-Purcell-Meiboom-Gill Sequence
CT	Computed Tomography
GBD	Global Burden of Disease
dGEMRIC	delayed gadolinium-enhanced MRI of cartilage.
2D	Two-Dimensional, 2-Dimensions
3D	Three-Dimensional
ECM	Extracellular matrix
EM	Electromagnetic
FCD	Fixed charge density
FTIRI	Fourier-transform infrared imaging
GAG	Glycosaminoglycan
Gd-DTPA^{-2}	Gadolinium diethylene triamine penta acetic acid
1H	Proton
MRI	Magnetic resonance imaging

MT	Magnetization transfer
MTR	Magnetization transfer ratio
MSME	Multi-slice multi-echo
μMRI	micro-MRI
NHANES	National Health and Nutrition Examination Survey
NIH	National Institutes of Health
NMR	Nuclear magnetic resonance
OA	Osteoarthritis
OARSI	Osteoarthritis Research Society International
P	Posterior
PG	Proteoglycan
PLM	Polarized light microscopy.
ROI	Region of interest
RZ	Radial zone
SZ	Superficial zone
TE	Echo time
TEc	Echo time of leading contrast segment
TSL	Spin lock period
T1	The spin-lattice (longitudinal) relaxation
T1ρ	The spin-lattice relaxation in the rotating frame

T2	The spin-spin (transverse) relaxation
TG	Trochlear groove
TR	Repetition time, Trochlear ridge
TZ	Transitional zone
UHF	Ultra-high-field scanners
σ	Stress
ε	Strain

LIST OF PUBLICATIONS

FIRST AUTHORED ARTICLES

1. **Batool, S**., Mahar, R., Badar, F., Tetmeyer, A., & Xia, Y. (2020). Quantitative μMRI and PLM Study of Rabbit Humeral and Femoral Head Cartilage at Sub-10 μm Resolutions. *Journal of Orthopaedic Research*, 38(5), 1052–1062.
2. **Batool, S**., Hammami, M., Mantebea, H., Badar, F., & Xia, Y. (2022). Location-Specific Study of Young Rabbit Femoral Cartilage by Quantitative μMRI and Polarized Light Microscopy. *Cartilage*, 13(1), 19476035221085144.
3. **Batool, S**., Roth, B., & Xia, Y. (2023). Depth-Dependent Strain Calculations for Anisotropic Fibril Structures in Articular Cartilage by Finite Difference Methods, to be submitted to a peer-reviewed journal.

The original articles have been reproduced with the permission of the copyright holders.

CO-AUTHORED ARTICLES

The author has also contributed to the following published work.

1. Mahar, R., Batool, S., Badar, F., & Xia, Y. (2018). Quantitative measurement of T2, T1ρ, and T1 relaxation times in articular cartilage and cartilage-bone interface by SE and UTE imaging at microscopic resolution. Journal of Magnetic Resonance (San Diego, Calif.: 1997), 297, 76–85. https://doi.org/10.1016/j.jmr.2018.10.008

2. Mantebea, H., Batool, S., Hammami, M., & Xia, Y. (2021). Structural Morphology of Rabbit Patella and Suprapatella Cartilage by Microscopic MRI and Polarized Light Microscopy. CARTILAGE, 13(2_suppl), 356S-366S.
3. Mantebea, H., Batool, S., Singh, A., Hammami, M., Badar, F., & Xia, Y. (2022). Structural differences between the immature and mature articular cartilage of rabbits by microscopic MRI and polarized light microscopy. Journal of Anatomy. 240(6):1141-1151. https://doi.org/10.1111/joa.13620.

CHAPTER ONE

INTRODUCTION

1.1 Introduction

Articular cartilage (AC) is a thin layer of avascular and aneural tissue on the articulating ends of long bones in joints (Marijnissen & Lafeber, 2003; Maroudas, 1968). The gradual degradation of articular cartilage is a hallmark of osteoarthritis (OA), which is a chronic disease and one of the leading causes of disability that affects millions of adults each year. The loss of articular cartilage weakens the effective distribution of mechanical load over the joint surface, which leads eventually to joint failure and the surgical need for joint replacement Currently, no disease-modifying drug has been approved for medical treatment, and most treatment guidelines only target symptom management. MRI is a non-invasive and non-destructive imaging tool with excellent soft tissue contrast to study the musculoskeletal system, including articular cartilage. Currently, the early diagnosis of osteoarthritis using clinical MRI is not achievable. There is a strong and unmet need in the clinic to find reliable and sensitive MRI-based imaging biomarkers, which are capable of detecting early degenerative changes for early intervention and tissue repair. At least three features of arthritic disease prevent the successful detection of early osteoarthritis in the clinic by clinical MRI.

1) Articular cartilage is thin (~2 mm in large human joints) and exhibits complex depth-dependent variations in both molecular structure and composition throughout its thinness. Conceptually, along with its thin thickness, cartilage can be divided into three histological zones (the superficial zone SZ, the transitional zone TZ, and the

radial zone RZ). Each zone has a characteristic thickness, a set of macromolecular concentrations, a unique orientation of the collagen fibrils, and a specific chondrocyte arrangement. These uneven structural variations across its thin thickness signify that any diagnostic technique, including MRI, requires high resolution imaging; otherwise, volume averaging in each image pixel could obscure any likelihood of early detection.

2) The image resolution in current diagnostic MRI is insufficient and lacks sensitivity to detect early changes in the tissue's fine structure and delicate functions, which precede the development of OA as a clinical disease.
3) OA is a slow-onset disease that spreads over many years. Because the tissue is avascular and aneural, early degradation remains silent to patients. By the time pain and stiffness are felt, chances for successful interventions in the initial stages may have been missed.

To overcome the first two obstacles, higher spatial resolution is required in the MRI of cartilage. Microscopic MRI (μMRI) is a high-resolution version of clinical MRI, which can have tens of microns in resolution and hence become potentially a useful tool to quantify microscopic details of cartilage degradation. To address the final obstacle, the use of animal models in OA research allows highly controlled and predicted outcomes. In a typical OA model, degradation can be initiated by a particular event, and the certainties in the timing and type of the disease initiation can enable careful studies of molecular and pathological changes during the subsequent degradation process (Bendele, 2001; Little & Zaki, 2012). With the step-by-step understanding of the degradation process from the early (the most vital period) to the late stage, an intervention at the early stages before the

point-of-no-return could be designed to ultimatelysave the joints in human. Although canines are likely the most studied OA model (Gregory et al., 2012; Paatsama, 1992; Pond & Nuki, 1973; Poole et al., 2010), the use of canines is being discouraged in recent years due to societal concerns and cost-effectiveness. Among other animal models (Bendele, 2001; Gregory et al., 2012; Lampropoulou-Adamidou et al., 2014; Little & Zaki, 2012; Poole et al., 2010), the use of rabbits is becoming popular because of its close phylogenetical and genetic resemblance to humans, as well as its sufficient thickness (~0.5 mm) for easier creation of local defects (better than small rodents ~0.1 mm), relative inexpensiveness, and less societal sensitivity (Batiste et al., 2004; Borrelli et al., 2009; Esteves et al., 2018).

We used quantitative protocols in μMRI combined with polarized light microscopy (PLM) to study the articular cartilage in rabbits as its potential use in an OA model. We aimed to test quantitative MRI at sub-10 μm resolution to elucidate topographical and zonal variations in the structural properties of rabbit articular cartilage. We used PLM as an independent imaging tool to validate the μMRI results. In addition to the experimental studies, a mathematical modeling project was carried out in this research to highlight the role of pre-stressed collagen fiber in the biomechanical compressive response of articular cartilage and calculating zonal strains in the tissue.

1.2 Organization of the Dissertation

This dissertation is divided into six chapters. The background is provided in Chapter 2 (articular cartilage and its composition, osteoarthritis, animal models, MRI and PLM imaging, biomechanics, and computational modeling). The original results are presented in Chapters 3, 4, and 5, which are based on the three individual projects, two of

which have been accepted by a refereed journal (Chapters 3 and 4), and a third has been submitted for a journal publication (Chapter 5). The final Chapter 6 provides the summary of the dissertation research and guidance for future work.

CHAPTER TWO

BACKGROUND

2.1 Articular cartilage

Articular cartilage (AC) is a thin layer (~0.1–3 mm, depending on the joint and animal of choice) of connective tissue that covers the articular ends of bones in diarthrodial joints to provide cushioning, protection, and load distribution during locomotion (Malda et al., 2013; Xia et al., 2016). Articular cartilage is also known as hyaline cartilage, named after the Latin word *hyalinus*, due to its smooth or glass-like appearance (Jeffrey & Watt, 2003). Mature cartilage contains no nerves or blood vessels and depends on internally self-diffusion and externally repetitive loading to intake nutrients and remove wastes (Mankin, 1994). Structurally, AC contains a small number of living cells (chondrocytes) and an extensive extracellular matrix (ECM) (Fig 2.1). The major constituents of its ECM are water (70-80% by wet weight), collagen (15-22% by wet weight), and proteoglycans (PGs) (4-15% by wet weight) (Fig 2.2) (Buckwalter & Mankin, 1998a; Maroudas, 1968, 1975a, 1975c; Maroudas & Venn, 1977; Buckwalter et al., 2005).

2.1.1 Water

Water is the most abundant molecular component of the ECM in cartilage, which has a depth-dependent concentration ranging from about 85% in the surface tissue to about 60% near the cartilage-bone interface. Judging by its molecular environment, at least two pools of water exist in AC: “bound” (a smaller pool) and “unbound” (a larger pool). When located close to the macromolecules in ECM, mainly PG and collagen, the water molecules have restricted and anisotropic mobility and hence are said to be bound;

further away from macromolecules water molecules are unrestricted and have more isotropic mobility, and hence can be considered unbound or free (Maroudas et al., 1991; Xia et al., 2016). Although water is a fluid, water molecules play an important role in the biomechanical properties of articular cartilage, by providing hydraulic pressure against external loads and forces. In addition, the flow of water through the ECM of cartilage and across the articular surface facilities the transportation of nutrients and the removal of wastes from the tissue (Buckwalter & Mankin, 1998b).

2.1.2 Proteoglycans

The most abundant macromolecules in adult cartilage are proteoglycan (PG), an aggrecan (Roughley & Mort, 2014; Sophia Fox et al., 2009) that consists mainly of a protein core covalently attached to negatively charged side chains of glycosaminoglycans (GAGs), chondroitin, and keratan sulfates. GAGs are macromolecular polysaccharides with a linear chain structure (Horkay, 2012). The core protein typically has a molecular weight of ~250 000 Da and can have more than 100 GAG molecules laterally bound to it in a branched, bottlebrush-like configuration. Because the GAG molecules are heavily sulfated, they carry negative charges and generate fixed charge density (FCD) through collagen-fibril interaction, which is the main source of cartilage swelling pressure (~0.05–0.35 MPa) and viscoelastic behavior (Maroudas, 1968, 1970; Maroudas & Bannon, 1981). In cartilage, the PG concentration is also known to vary continuously through the tissue depth (being least just below the surface) (Mittelstaedt & Xia, 2015; Xia, Zheng, et al., 2008; Yin et al., 2011). PGs are responsible for the hydration of the matrix, stabilization of collagen networks, and giving the tissue its ability to resist compression due to repulsion between the negative charges.

2.1.3 Collagen

Collagen fibers play a crucial role in the mechanical functionality of articular cartilage, via its unique depth-dependent structure and its interactions with the other ECM molecules, mainly water and proteoglycans (Basser et al., 1998). Collagen is a structural protein and the main solid component of cartilage's ECM, which contains several different types of collagens. The most abundant type of collagen in the ECM of adult cartilage is type II (Buckwalter & Mankin, 1998b), which is a fibrillar protein consisting of tropocollagen forming a triple helix configuration (Eyre, 1991) (Fig 2.1). The tropocollagen molecules are assembled into small prototypic fibrils with an axial repeat length D of ~65−67 nm that is called the D-period (Antipova & Orgel, 2010), which gives collagen its characteristic striated appearance in high-resolution electron microscopy images. Scanning electron microscopy (SEM) images have revealed that multiple collagen fibrils bundle into large collagen fibers. The thickness or diameter of collagen fibers has been reported to vary with the cartilage depth and lies in the range between 25 nm near the surface and 200 nm in deep cartilage (Gottardi et al., 2016).

Collagen type II, together with type IX and XI collagens, form a fibrillar meshwork through the depth of the tissue in a trizonal manner in mature cartilage, which is absent in immature or neonatal cartilage (Julkunen et al., 2009). A unique structural feature of the collagen fibers in mature articular cartilage is their depth-dependent orientation, which can be used to subdivide the noncalcified cartilage into three sub-tissue zones (Fig 2.1). The fibers are parallel to the surface in the superficial zone (SZ) (10–15% of overall thickness), without any predominant orientation in the transitional zone (TZ) (20–40%), and perpendicular to the surface in the radial zone (RZ) (60–70%).

The radial fibers anchor the cartilage to the subchondral bone (Aspden & Hukins, 1981; Benninghoff, 1925; Fox et al., 2009). Below RZ, there is a zone of mineralized calcified cartilage that attaches to the underlying subchondral bone. A mineral front, the *tidemark*, distinguishes between the non-calcified and calcified tissues.

The role of the collagen fibers' orientation has been predicted to be the primary factor modulating the crack morphology in cartilage under indentation loading (Moo et al., 2021). During growth and maturation, structural variations in the collagen network are observed to occur across tissue depth, from a monolayer in neonates to a mixed multizonal layer and finally the standard trizonal structure in mature tissue (Julkunen et al., 2010; Xia et al., 2003). It remains not clear that how these structural variations in the collagen fibril network contribute to the functional response of the tissue. A current understanding is that once the tri-zonal structure is established in mature tissue, the concentrations of macromolecules in ECM are responsible for the tissue's resistance to compressive stress (Guterl et al., 2010; Han et al., 2011), through osmotic swelling pressure and electrostatic repulsion between negatively charged PGs.

The PGs bind to the collagen fibers via their core proteins, with their GAG side chains shown to form bridges between adjacent collagen fibers (Lewis et al., 2010). Without the collagen framework, the PGs could dissociate into smaller molecules. At equilibrium, the ECM in healthy cartilage is known to be in a state of pre-stress required to balance the swelling pressure induced by negatively charged PGs, which is vital for tissue load-bearing strength and homeostasis. Any imbalance between the PG swelling pressure and the collagen fibers restraining stress could alter the normal mechanical function of the tissue and be a manifestation or initiation of degradation.

2.1.4 Chondrocytes

Chondrocytes are the only kind of living cells in AC (Buckwalter & Mankin, 1998b). They are the primary structural, functional, and metabolic units, responsible for the balance of the ECM catabolism and anabolism (Kuettner, 1992). A single cell or a small group of cells are surrounded by a pericellular matrix, which is embedded in the ECM. The cells are sparsely spaced (1%–2% of the total cartilage volume) in adult cartilage and vary in numbers, sizes (approximately ~10 μm), and shapes (oval to circular) through the depth of tissue (Choi et al., 2007; Quinn et al., 2013). The depth-dependent alignment of the collagen network in the ECM has been suggested to modulate the cell shape differently in different zones. Chondrocyte metabolism is chiefly controlled through mechanical stimuli generated in the surrounding matrix and can influence the biochemical conditions of the tissue (Mow et al., 1999). During skeletal growth, chondrocytes significantly undergo growth and differentiation and are responsible for synthesizing and remodeling the ECM (mainly collagen type II and proteoglycan). The collagen is synthesized by the chondrocytes during skeletal growth, which virtually ceases in the adult articular cartilage. In adult human cartilage, collagen turnover is significantly slower (several hundred years) than proteoglycan turnover (1–5 years) (Heinemeier et al., 2016; Maroudas, 1975b).

2.2 Depth-dependent characteristics of articular cartilage

AC is a thin layer of complex tissue. It exhibits unique depth-dependent physical and biological properties in terms of the content and structure of its constituent cellular and matrix components. Collagen fibers form unique structural frameworks in a depth-dependent manner as described before (Fig 2.1). In addition to the depth-dependent

structure of the collagen network, the distributions of all molecular components (water, proteoglycan, and collagen) are also not homogenous, and all vary with depth from the articular surface towards the cartilage-bone interface (Mittelstaedt & Xia, 2015; Rieppo et al., 2009; Xia, Zheng, et al., 2008). For mature and healthy cartilage, the SZ has a lower concentration of PGs and a higher concentration of water, when compared to the RZ (Mittelstaedt & Xia, 2015; Xia et al., 2016). In general, a clearer understanding of the depth-dependent variations of the ECM macromolecular components, in conjunction with the structural variations, is crucial in determining cartilage health and the alterations that occur from degradation (OA).

2.3 OA

AC can develop degenerative changes due to aging, excessive usage, and trauma. According to Osteoarthritis Research Society International (OARSI, 2015),

> *Osteoarthritis is a disorder involving movable joints characterized by cell stress and extracellular matrix degradation initiated by micro-and macro-injury that activates maladaptive repair responses including pro-inflammatory pathways of innate immunity. The disease manifests first as a molecular derangement (abnormal joint tissue metabolism) followed by anatomic, and/or physiologic derangements (characterized by cartilage degradation, bone remodeling, osteophyte formation, joint inflammation, and loss of normal joint function), that can culminate in illness.*

The prevalence of the number of people living with OA worldwide has increased significantly; it nearly doubled from 1990 to 2019, according to the Global Burden of Disease study (Institution for Health Metrics and Evaluation, 2023). In the report of the

National Health and Nutrition Examination Survey I (NHANES I), an estimated 12% of US adults ages 25–74 years have clinically diagnosed OA (NHANES, 2020). OA is the most common type of arthritis in terms of prevalent cases and ranked 17th highest of the 369 diseases and injuries included in the Global Burden of Disease study (Vos et al., 2020). OA is also considered a concern of global health and economic burdens in terms of increase healthcare costs, a decline in the workforce, and loss of wages due to disability. The overall economic burden associated with OA in the US is estimated at $136.8 billion annually (OAA, 2023; United States Bone and Joint Initiative, 2023).

The limited healing potential of articular cartilage imposes challenges to the efficacy of repair strategies. Currently, there are no drugs or treatments that can effectively regenerate or restore the damaged cartilage without surgical intervention. Clinically, it is extremely challenging to slow down the progression of OA over time; a total joint replacement is the common result for millions of OA patients worldwide. Therefore, there is a consistent interest in finding non-invasive imaging biomarkers with sufficient sensitivity to cartilage health and early degradation, to plan timely and effective interventions and to design new cartilage repair strategies. In current clinical practice, being noninvasive and having exceptional soft tissue contrast, MRI has proven to be an exceptional tool in OA management (clinical diagnostics and laboratory research). Since articular cartilage is a thin layer of tissue, however, the current resolution in clinical MRI is insufficient to detect early degenerative changes in articular cartilage.

2.4 Rabbit as an OA model

The use of animal models plays a vital role in OA research, as degradation in animals can be initiated by a particular event and monitored with time. Although some

studies have claimed the ability of the rabbit's cartilage to heal and repair rapidly after a traumatic experience, this model is still popular for intermediate-sized animals in OA research as it provides sufficient size/thickness for easier creation of local defects. Recently the reports on the radiographic signs of OA, associated with age and weight in aging domestic rabbits, make rabbits a reasonable choice to study both traumatically induced and naturally occurring OA (Arzi et al., 2011).

2.4.1 Age

The age or maturity of the animal is an important factor to consider before planning any orthopaedical experiments and studies. In the case of New Zealand white male rabbits, the average timeline for physeal closure is ~ 6 months with some exceptions, where physes does not close until 9-10 months (Bland & Ashhurst, 1996; Isaksson et al., 2010). There are vivid age-related differences in tissue response to naturally occurring or trauma-induced OA, e.g., the post-traumatic healing response is reported to be weaker in the aged rabbits (24 months old) than in younger rabbits (4 months). In general, cartilage repair, and response to trauma or surgical interventions were all found to be age-dependent (Buckwalter & Mankin, 1998a; Calandruccio & Gilmer, 1962; Frenkel et al., 2005; Wei et al., 1997). There is speculation that the immature rabbit cartilage has some potential for self-healing, but the underlying mechanism is poorly understood. In addition, significant structural differences in collagen fiber organization and glycosaminoglycan distribution have been reported to present in different locations of the immature rabbit knee cartilage (Batool et al., 2022; Heise & Toledo, 1993; Julkunen et al., 2010), which is possibly related to the natural growth and maturation process. Such age-related differences should be kept in mind when choosing

the animal model for OA studies; and in some cases, skeletally mature animals might be a better choice.

2.4.2 Topographical variations

Cartilage has several topographical variations (i.e., among different locations on a single joint surface) in the biochemical, physical, optical, and mechanical properties (Brama et al., 2000a; Briant et al., 2015; Lee et al., 2016; Risch et al., 2021; Xia, Moody, Alhadlaq, et al., 2002). These topographical variations can cause significant differences in the results of a study whether it is morphological or mechanical, physical or chemical, in vivo or in vitro, and clinical or preclinical.

Topographical variations in healthy cartilage of a joint are dependent on age, gender, differences in the mechanical demands between joints, and sometimes in the different sites over the same joint (Roth & Mow; 1980, Kempson, 1991, Julkunen et al., 2010, Brama et al., 2000a; Batool et al., 2022)). Such variations include but are not limited to tissue thickness, cell shapes, density, collagen fibril organization, fibril orientation, the concentration of macromolecules (collagen, GAG) and water, stress-strain response, and local stiffness. Some joints are more complex in terms of topographical variations than others e.g., the knee is more complex than the hip and shoulder joints. These variations can influence any imaging and data analysis, and optimization of various research protocols. The choice of sampling sites from any single joint surface can therefore significantly influence the outcomes of biochemical or biomechanical studies of articular cartilage. Studying these variations is important in improving the consistency and accuracy of outcomes of biochemical and biomechanical studies.

2.5 Biomechanics

Since cartilage is a load-bearing tissue, biomechanical testing of cartilage is essential in OA diagnostics and research. Usually, the compressive modulus of cartilage can be correlated with the stiffness of the tissue. When cartilage is compressed using unconfined, confined, or indentation experiments, the integrity of the tissue can be determined by its response to compression (Setton et al., 1999).

2.5.1 Young's modulus

Several biomechanical parameters in cartilage can be measured using stress relaxation and creep experiments, e.g., instantaneous compressive modulus, aggregate modulus, Poisson's ratio, etc. The instantaneous compressive modulus is measured during the loading phase of stress relaxation. The aggregate modulus is a measurement of the stiffness of the tissue at the equilibrium when all fluid flow has stopped. Poisson's ratio is the ratio of the change in radial length to the change in axial length of the tissue.

Usually, the modulus of cartilage can be correlated with the stiffness of the tissue. Young's modulus μ, is a ratio of stress and strain, given by

$$\mu = \frac{\sigma}{\varepsilon} \tag{2.1}$$

where $\sigma = \frac{F}{A}$ is stress and $\varepsilon = \frac{\Delta L}{L}$ is strain, F is the resultant force, A is the contact area of the compressor and tissue, ΔL is the net displacement, and L is the uncompressed tissue length or thickness. The experimental setup to measure the stiffness of tissue typically consists of a rigid frame, load sensor, and compression platen. A rigid frame houses the sample, a load sensor measures force, and a micrometer or computer-controlled actuator

controls the compression plate movement. Under action, the platen compresses the sample in small and successive steps, and the load sensor measures the resultant force. The force and displacement are both recorded, and the elastic modulus can be calculated.

2.5.2 Viscoelasticity

During joint loading (compression), there is an immediate increase in interstitial fluid pressure which leads to a fluid flow out of the ECM. The displacement of the fluids in cartilage is a function of time because the fluid cannot escape from the matrix instantaneously. When the compressive load is removed, interstitial fluid would flow back (Mow et al., 1999). Experimentally, it has been shown that interstitial water pressure contributes to more than 90% of the initial load-carrying capacity at the cartilage surface, thereby reducing the stress acting upon the solid matrix (Ateshian, 2009; Ateshian et al., 1994; Ateshian & Wang, 1995). Any material whose properties have time dependency are said to be viscoelastic material.

2.5.3 Creep and Stress relaxation

Two biomechanical tests are commonly used to estimate the viscoelastic properties of the tissue. Creep is a time-dependent deformation of a viscoelastic material under the application of a constant stress at a constant temperature. A step-like load is applied to the cartilage, and the time dependence of the resultant deformation (strain) is monitored (Fig 2.3a).

Stress relaxation refers to the measurement when a constant displacement (strain) is applied to the cartilage and the time dependence of the induced stress is monitored. As the tissue is compressed, the deformation results in an increased stress and leads to fluid displacement, after which relaxation occurs (Fig 2.3b).

2.6 Depth-dependent compressive stiffness of articular cartilage

Articular cartilage deforms in a depth-dependent manner when compressed. Biomechanical testing in combination with different imaging techniques allows better visualization and understanding of how the cartilage responds under compression (Alhadlaq & Xia, 2005; Wang et al., 2015). In mature healthy cartilage, the RZ exhibits a stronger resistance to compression than the SZ and TZ (Fig 2.4b). Using fluorescence-labeled chondrocyte nuclei as intrinsic markers, Schinagl et al. (1996) measured the intra-tissue deformation within the cartilage matrix and found that the compressive modulus increased significantly with depth from the articular surface to the cartilage-bone interface, ranging from 0.079 MPa in the SZ to 2.10 MPa in the deep RZ. It is known that the close association between proteoglycan aggregates, interwoven collagen fibrils, and interstitial fluid provides compressive resilience to cartilage through its depth. It has also been reported that an increase in the depth-dependent GAG concentration, related to the FCD, may alter the depth-dependent biomechanical behavior. When compressed, the negatively charged sites on aggrecan pushed closer together. This effect increases their mutual repulsive force and adds to the compressive stiffness of the cartilage with depth (Chen et al., 2001; Mattson et al., 2017; Pfeiffer et al., 2008; Wilson et al., 2007).

Although the GAG concentration, which is related to the FCD, has been suggested to modulate the compressive resilience of the cartilage, the role of collagen fibrils should not be ignored. The intrinsic swelling of cartilage is resisted by the collagen network which is in the state of pre-stress (tension) and may play a role in resisting compression. The role of collagen fibers in articular cartilage during loading has been studied extensively but the pre-stressed condition is mostly ignored. Under small

deformations, the fibrils are in tension, while at larger deformations, the forces within the fibrils become compressive (Römgens et al., 2013), eventually leading to buckling (which is a reversible process). At both smaller and larger deformation, therefore, the fibrils in cartilage will likely contribute differently to the compressive stiffness of the tissue.

2.7 Computational models

Although the behavior of articular cartilage under compression and changes in the cartilage structure and composition can be studied by using in vivo and in vitro imaging techniques (MRI, CT, various optical microscopies), these imaging techniques alone are unable to quantify the local tissue stresses, strains, fluid flow produced inside ECM and the independent roles of different cartilage constituents (e.g., collagen, PGs, fluid, and ions) in the loading response due to the complexity of articular cartilage. Therefore, computational models in conjunction with imaging techniques have been employed to determine the material properties of cartilage under different loading conditions.

In the early models of articular cartilage, the tissue was considered isotropic, homogenous, and biphasic (Mow et al., 1980). The biphasic theory models the tissue as a mixture of two phases: a charged porous permeable solid phase (collagen-proteoglycan matrix) and an interstitial fluid phase. Later, a triphasic model (Lai et al., 1991) of articular cartilage was introduced as an extension of the biphasic theory, where negatively charged proteoglycans are modeled to be fixed to the solid matrix, and monovalent ions in the interstitial fluid are modeled as additional fluid phases. According to the triphasic model, the swelling of articular cartilage depends on its fixed charge density distribution, the stiffness of its collagen-proteoglycan matrix, and the ion

concentrations in the interstitial fluid. These models, however, lack the structural inhomogeneity and anisotropic properties of ECM and consider cartilage to be a homogenous, isotropic, and viscoelastic material, which probably does not allow the discrimination between PGs and collagen-dependent mechanical properties, which are required for a more accurate understanding of cartilage mechanics. To address this issue, several fibril-reinforced models (fibril-reinforced poroelastic, poroviscoelastic, hyperelastic) have been introduced to include the effect of fibril anisotropy in traditional biphasic and triphasic models (Korhonen et al., 2003; Pierce et al., 2013; Soulhat et al., 1999; Wilson et al., 2005). These models all treat cartilage as inhomogeneous and anisotropic tissue and include many aspects of the real tissue structure and composition.

2.8 Quantitative MRI in cartilage research

2.8.1 Introduction

MRI is a sensitive and noninvasive imaging tool that can produce detailed anatomical images of biological specimens due to its high sensitivity to the dynamic motion of water molecules. The brain, spinal cord, and a number of connective tissues (muscles, ligaments, tendons, and articular cartilage) can all be seen much more clearly in MRI than in regular x-rays and computed tomography (CT). The technique is currently widely in use in clinical and preclinical settings for disease detection, diagnosis, and treatment monitoring. MRI is also safer than CT, since it does not utilize damaging ionizing radiation.

The working principle of MRI is nuclear magnetic resonance (NMR), which was first discovered in 1930s by I.I. Rabi, who measured the magnetic properties of atomic nuclei. He found that under a strong magnetic field, the spin states of the atomic nucleus

would flip if an electromagnetic (EM) wave at a specific frequency was incident on it. The resonance occurs when the incident oscillation frequency matches the intrinsic frequency of the nucleus, which depends on the strength of the static magnetic field (B_0), the chemical environment and the magnetic properties of the nucleus involved. This intrinsic precessional frequency is known as the Larmor frequency and given as

$$\omega = \gamma B_0 \qquad (2.2)$$

where γ is the gyromagnetic ratio (rad $\sec^{-1}T^{-1}$). Among the nuclei found in the human body that have a nonzero nuclear spin (e.g., ^{1}H, ^{13}C, ^{17}O, ^{19}F, ^{23}Na, ^{31}P), hydrogen is by far the most dominant nucleus of interest. For the ^{1}H nucleus (proton), the gyromagnetic ratio is 42.57 MHz T^{-1}.

2.8.2 NMR to MRI

In 1946, Felix Bloch and Edward Purcell demonstrated the NMR phenomenon in bulk matter, for which they shared the Nobel Prize in Physics in 1952 (Bloch, 1946, 1953; Purcell, 1946). In the 1950s, Erik Odeblad and Gunnar Lindstrom were the first to use NMR to study various biological tissues including articular cartilage (Odeblad and Lindstrom, 1955; Xia and Stilbs, 2016). For the next 20 years from the 1950s to the 1970s NMR was used exclusively in spectroscopy to analyze the structures of organic molecules. The earliest use of NMR for diagnostic purposes was likely in 1971 when R. Damadian showed that the NMR relaxation parameters (T1 and T2 relaxation) were significantly different in malignant tumor tissue when compared to normal tissue.

The era of MRI started in 1973 when Paul Lauterbur performed the first imaging experiment using the principle of NMR. Given the linear proportionality between the precessional frequency of the nuclei (e.g., protons in water) and the magnitude of the

external magnetic field (i.e., Eq (2.1)), a position-dependent magnetic field (i.e., a field gradient) can encode the physical space where the specimen resides. By setting up three field gradients in three orthogonal directions, the frequency of the nuclei (e.g., protons) can be spatially encoded in any 3D or 2D space in the form of an image. For this work, the extension of NMR to NMR imaging (or MRI), P. Lauterbur and P. Mansfield shared the Nobel Prize in Medicine in 2003.

2.8.3 Instrumentation

A complete MRI system consists of a magnet, which is used to generate the B_0 field. A radiofrequency (rf) coil can act both as a transmitter coil to deliver the energy to the specimen (a B_1 field) and as a receiver coil to receive the signal generated by the transverse magnetization (the free induction decay, FID). The use of three independent gradient coils can produce the linear field gradients with their magnitudes varying in the x, y, and z directions respectively. The MRI system also needs at least one computer for human-machine interface and a complex array of electronic components.

2.8.4 MRI contrast

MRI signal is sensitive to the motional dynamics of the nuclei in the system. Since the proton (^1H) is the most common and sensitive nucleus in biological systems, most MRI experiments rely on the water molecules in any water-containing specimens (biological or not) for its signal. There are several fundamental molecular mechanisms that are responsible for the unique characteristics of the MRI signals. We will discuss a few of them that are relevant to this dissertation, emphasizing their influences on the MRI signal.

In any practical (bulk) sample, the vast numbers of nuclear spins of protons precessing in a strong magnetic field (B_0) can be viewed/averaged as a macroscopic magnetization M vector, pointing to the +z direction in the thermal equilibrium condition. When an oscillating rf field (B_1 field) is applied in the transverse plane under the resonant condition (i.e., at the Larmor frequency), the macroscopic magnetization will be tipped towards the transverse plane (x-y plane, as in Fig 2.5a). After M is tipped to the transverse plane and the B_1 field is turned off, the nuclear spins will relax back to the +z direction. Since the M vector can be separated into two components, M_z in the longitudinal z-axis and M_{xy} in the transverse x-y plane, the relaxation of the nuclear spins can be examined in transverse and longitudinal directions (Fig 2.5a).

The time rate of change of the longitudinal component of the net magnetization (M_z) is given in the classical mechanical description as

$$\frac{dM_z}{dt} = -\frac{(M_z - M_0)k}{T_1} \tag{2.3}$$

where M_0 is the unperturbed macroscopic magnetization of the spin system, and T_1 is a longitudinal relaxation time, characterizing the spin-lattice interaction (Fig 2.5c).

Similarly, the time rate of change of the transverse component of the net magnetization (M_{xy}) is given as

$$\frac{dM_{xy}}{dt} = -\frac{(M_x i + M_y j)}{T_2} \tag{2.4}$$

where, M_x and M_y are the x and y components of the magnetization and T_2 is a transverse relaxation time, characterizing the spin-spin interaction (Fig 2.5b).

T_1 (the spin-lattice relaxation time) and T_2 (the spin-spin relaxation time) are the two most common types of MRI contrast in water-rich specimens especially in the biological and clinical environment. In addition, there is a spin-lattice relaxation time in the rotating frame, or $T_{1\rho}$, which is the relaxation of the macroscopic magnetization being spin locked in the transverse plane. The difference between their characteristics is closely related to the dominant frequencies of the molecular environment, which can be explained with the aid of nuclear spin dynamics. T_1 is sensitive to the highest frequencies of molecular motions in the Larmor frequency range (tens and hundreds of MHz); $T_{1\rho}$ is sensitive to the intermediate frequencies in the range of several or tens of kHz; and T_2 is sensitive to the lowest frequencies of molecular motions involving static or slowly fluctuating magnetic fields. These relaxation times have been explored extensively by incorporating different relaxation weighting mechanisms in the imaging pulse sequences.

2.8.5 Magnetization prepared pulse sequences in MRI

Practically, an MRI experiment is under the control of a pulse sequence, which is a list of time events on when and how the rf field and various gradient fields are applied and the data is acquired. In any imaging experiment, the influence of the spin relaxations (in particular, T2 relaxation) exists in the final image, different for different imaging sequences. Consequently, a true nuclear spin density (i.e., a true map of water content in a biological specimen) is difficult to quantify. In our MRI work, we commonly use 2D imaging pulse sequences in the format of magnetization preparation (Xia, 1998). This format of imaging sequences contains two clearly separated time-segments, a leading contrast segment and a subsequent imaging segment. The leading contrast segment uses a variable timing table to impose an image contrast (either T2 contrast or T1 contrast);

while the final imaging segment keeps all timings constant – hence the contrast effect of this imaging segment can be normalized in the final image analysis.

To impose a T2 contrast, a spin-echo or CPMG (Carr-Purcell-Meiboom-Gill) sequence can be used in the leading contrast segment. For example, in the spin-echo format, a 90° rf pulse is applied to tip the net magnetization into the transverse plane. At a time TEc/2, a 180° rf pulse flips the dephasing magnetization about the transverse plane, which results in the re-phase of the spins at the time TEc (where TEc is the echo time between the 90˚ rf pulse and the echo center). A final -90° rf pulse tips the refocused transverse magnetization back to the longitudinal direction (z-axis), to prepare it for imaging. The imaging segment typically starts with a slice selection sequence, which has a soft 90° rf pulse together with one gradient pulse. Subsequently, a set of 2D imaging gradients in the orthogonal plane can be applied to sample the signal over the 2D **k** space (raw data matrix). Two important parameters in MRI are the echo time (TEi), which is the time duration between the center of the first 90˚ soft rf pulse and the center of the signal in acquisition (Fig 2.6b), and the repetition time (TR), which is the time duration at which the sequence repeats itself. Using several TEc, an exponential fit can be applied to the peaks of the signal, which enables the quantitative calculation of the T2 relaxation time, as

$$M_{xy}(TE) = M_{xy}(0)\, e^{-\left(\frac{TE}{T2}\right)} \tag{2.5}$$

where $M_{xy}(0)$ is the net signal, and TE is the variable time in the contrast segment.

To impose a T1 contrast, an inversion recovery sequence can be used in the contrast segment, in which the magnetization is inverted along its longitudinal direction

(to the -z direction) by a 180° rf pulse. After a time, delay τ_i (the inversion time), a 90° rf pulse is applied to tip the magnetization into the transverse plane for signal detection. Therefore, the signal intensity depends on the delay time between the 180° and 90° rf pulses (Fig 2.6a). This process can be repeated for various τ_i, which imposes different T1 contrasts. The calculation of T1 can be performed using the following equation,

$$M(\tau_i) = M_0\left(1 - 2\,e^{-\left(\frac{\tau_i}{T1}\right)}\right) \tag{2.6}$$

where M_0 is the initial magnitude of the signal right after the 180° pulse, M (τ) is the signal depending on τ_i. Several τ_i are needed to calculate the T1 relaxation time.

To impose a T1ρ contrast, a 90° rf pulse tips the magnetization into the transverse plane; immediately after, the magnetization is spin-locked in the transverse plane by a second rf pulse in the direction of the magnetization vector. Under the resonance condition, this second rf pulse (a spin-lock B1 pulse) is the only field in the rotating frame of reference, which acts to keep (i.e., spin-lock) the magnetization in the transverse plane. However, the magnitude of the magnetization was established under B_0, which is often too big to be maintained by the spin-lock B_1 field, hence the magnetization will shrink its magnitude according the power of the spin-lock field. The time duration and power of the spin-lock B1 pulse is known as the spin lock time (TSL) (Fig 2.6c). When the power of the spin-lock field is zero, T1ρ relaxation is identical to T2 relaxation.

2.8.6 Quantification of relaxation times in MRI of articular cartilage

Due to its excellent soft tissue contrast and its ability to map the molecular environment of tissue, MRI has been increasingly used in the diagnosis of OA and other musculoskeletal disorders. However, the measurement sensitivity to *early* cartilage

degeneration, occurring before morphological changes, is still limited. In the last two decades, several quantitative MRI techniques for cartilage imaging, such as sodium MRI, T1ρ and T2 relaxations, diffusion MR, and delayed gadolinium-enhanced MRI of cartilage (dGEMRIC) have been used to assess different aspects of the extracellular matrix of cartilage and as potential biomarkers for early degradation (Baum et al., 2013; David-Vaudey et al., 2004; Duarte et al., 2019; Hänninen et al., 2021; Lammentausta et al., 2006; Li et al., 2007; Garrick, 2016; Nissi et al., 2007; Shapiro et al., 2002; Xia, Zheng, et al., 2008). The quantifications of relaxation times are currently the most used protocols in clinical MRI for imaging cartilage and joints.

2.8.7 Quantitative T2 in cartilage imaging

T2 imaging in mature articular cartilage is both depth-dependent and orientation-dependent (Mahar et al., 2018; Xia, Moody, & Alhadlaq, 2002), which reflect the combination of water content, PG content, collagen content and collagen fiber orientation in the ECM. When the normal axis of the cartilage surface is placed at 0° to the external magnetic field B_0, articular cartilage appears bilaminar or tri laminar in high-resolution T2 weighted MRI images. Quantitative analysis of T2 (0˚) in healthy cartilage shows that T2 values in the deep zone are significantly shorter than in the SZ and TZ. This is because the deep zone collagen fibers are densely packed so restricting the mobility of water protons. In addition, at orientations close to 0˚, there is a strong influence from the nuclear dipolar interaction in deep cartilage, which shortens the measured T2 values (Bydder et al., 2007; Xia, 2000b). A depth-dependent T2 profile at 0° is bell-shaped, which implies a classical three-zone structure in cartilage and has been used to subdivide cartilage thickness into multiple histological zones (Xia et al., 2001a). At the magic angle

(55° to B_0), this laminar appearance vanishes and the cartilage appears homogenous with a maximum signal intensity (Xia, 2000b). This is due to the minimization of the nuclear dipole interaction. The disappearance of the cartilage laminae associated with the 55° angle is known as the magic angle effect in MRI of cartilage (Bydder et al., 2007; Xia, 2000b). Due to the geometric factor in the dipolar interaction, $(3\cos^2\theta - 1)$ (Xia, 1998), the radial zone of cartilage has stronger T2 anisotropy than TZ and SZ.

Quantitative mapping of T2 relaxation time is one of the most used techniques in MRI of cartilage due to its unique relationship with the structural integrity and arrangement of the collagen network as well as the water content in the tissue. T2 has also been reported to increase in spontaneous degeneration of articular cartilage and used as a vital imaging biomarker to study the progression of OA (Baum et al., 2013; David-Vaudey et al., 2004).

2.8.8 Quantitative T1 in cartilage imaging

In contrast to the depth-dependent anisotropy in T2 relaxation, T1 is known to be isotropic and has a small dependency on its tissue depth. In healthy cartilage, T1 is associated with slow motional interactions between the water molecules and highly constrained PGs (Xia, 2013). A common usage of T1 in MRI of cartilage is via the measurement of T1 before and after doping the tissue with a negatively charged contrast agent, gadolinium diethylene triamine penta acetic acid (Gd-$DTPA^{-2}$). Since Gd-$DTPA^{-2}$ is repelled by the negatively charged GAGs and tends to deposit in the inverse proportion to the local GAG concentration in tissue (Bashir et al., 1996; Owman et al., 2008), different depositions of Gd-$DTPA^{-2}$ can be used to determine the local GAG concentrations. This technique is known as delayed Gadolinium-Enhanced MRI of

cartilage (dGEMRIC). Since the contrast agent contains heavy metal ions, the use of this procedure in a patient requires caution.

2.8.9 Quantitative T1ρ in cartilage imaging

A subtle feature of T1ρ relaxation is its dependency on the strength of the spin-lock field. With a sufficiently high spin lock field (e.g., > 2 kHz), the influence of the dipolar interaction to spin relaxation can be minimized (Wang & Xia, 2013). When the spin-lock field is zero, T1ρ relaxation is identical to T2 relaxation, which shows strong anisotropy in cartilage MRI. With an increase in the spin-lock power, T1ρ becomes less anisotropic, less depth dependent, and has higher values than T2. The measurements of T1ρ probe molecular fluctuations in the kHz range and are sensitive to the interactions between motion-restricted water molecules and their local macromolecular environment. Some studies showed T1ρ imaging could differentiate between normal cartilage and early-stage OA (Li et al., 2007; Mlynárik et al., 1999) and be correlated with proteoglycan loss in vitro (Duvvuri et al., 2002), which provides an attractive alternative to map GAG loss, an early sign of cartilage degeneration.

2.8.10 Spatial resolution in MRI of cartilage

A major limiting factor in clinical MRI of articular cartilage in humans is its imaging pixel resolution, typically 300-500 μm for 3 Tesla whole-body systems, which does not provide sufficient resolution to determine the zonal characteristics of human cartilage (2-3 mm total thickness), nor the detection of early (i.e., small) degenerative changes topographically in joint degeneration. Ample work is in progress to improve the resolution and sensitivity of clinical MRI of OA.

In small animals, articular cartilage is much thinner than the tissue in large primates and humans (Malda et al., 2013), which requires even higher spatial resolution. In this regard, the use of high-resolution microscopic MRI (μMRI) is preferred to precisely identify the anatomical features of the cartilage from small animals. The rabbit cartilage is $\sim 1/4$ times thinner than human cartilage and it has been shown that a resolution on the order of 10 μm is required to successfully resolve its depth-dependent structural features (Batool et al., 2020). The fact that μMRI shares identical physics principles and engineering architectures with clinical MRI ensures a translational pathway between the animal model study of OA to clinical detection and intervention (Xia, 2013).

2.9 PLM imaging in cartilage research

The PLM is a gold standard in histology, which is capable of analyzing the anisotropy of a specimen's optical properties such as refraction and absorption (Mehta et al., 2013). In articular cartilage, due to the orientation and organization of the collagen fibers in the tissue, cartilage is birefringent, which exhibits two different indexes of refraction along perpendicular axes.

2.9.1 Working principle of PLM.

Light is an electromagnetic wave that has two orthogonally oscillating components: electric and magnetic components, both orthogonal to the direction of light propagation. Natural light is nonpolarized which can vibrate in all perpendicular planes to the direction of propagation, while polarized light vibrations are restricted in a specific plane (Fig 2.7). Polarized light microscopy makes use of polarizing filters to study the anisotropic properties of materials, which have distinct optical axes and hence whose

optical properties dependent upon the orientation of their axis to the incident light. When light enters a non-equivalent axis in an anisotropic material, it is refracted into two orthogonal components (ordinary and extraordinary waves), which travel at different speeds through the specimen and experience different refractive indices, a phenomenon known as birefringence or (bi-refraction).

Birefringence (b) can be quantified by the numerical difference between these two indices and is given by relation.

$$b = |n_e - n_0| \tag{2.7}$$

where n_e and n_0 are the extraordinary (slow) and ordinary (fast) axis indexes of refraction, respectively. After exiting the specimen, the light components become out of phase, and interfere between the two components as they are re-united along the same optical path. This enables the study of anisotropic materials, based on their birefringent properties.

A common PLM system consists of multiple polarizers and wave plates to measure the sample birefringence without the need to rotate the sample (Oldenbourg & Mei, 1995). Microscopes can be outfitted with a mounted camera to capture images of a specimen and be connected to a computer to analyze the images, to calculate several parameter maps such as the collagen fiber orientation and organization, and pericellular matrix around chondrocytes.

2.9.2 Retardation and azimuthal measurements

In articular cartilage, the birefringent properties of its ECM can be quantitatively examined by two parameters, retardation, and angle (azimuth), which correspond to the local fibril organization and the fibril orientation respectively (Xia et al., 2001a). The

retardation and azimuth calculations at high resolution in PLM show a depth-dependent anisotropic structure of the collagen network in cartilage. The retardation value is high in the SZ, low in the TZ, and high in the RZ related to the degree of collagen fiber organization and density in different zones. The azimuth calculation shows the collagen fibers are oriented parallel, randomly, and perpendicular to the articular surface in the SZ, TZ, and RZ, respectively (Lee & Xia, 2013). Mapping these two parameters has also permitted the detection of a disrupted collagen matrix due to the early onset of lesions and tissue deformation due to loading (Alhadlaq et al., 2004, 2007b).

Since the structural orientation and organization of the collagen matrix in cartilage are the cause of the magic angle effect and T2 anisotropy in MRI of cartilage, the quantitative correlation between MRI and PLM has enabled independent validation of the ultrastructural information in our comprehensive studies of cartilage and other connective tissues (Batool et al., 2020, 2022; Xia et al., 2001a). Chapter 3 and 4 results are based on the quantitative MRI relaxation data and PLM fibril structural data, which clearly show distinct features in tissue properties at different depths and at different anatomical locations.

Figure 2.1

Articular cartilage structure from macro to micro scales

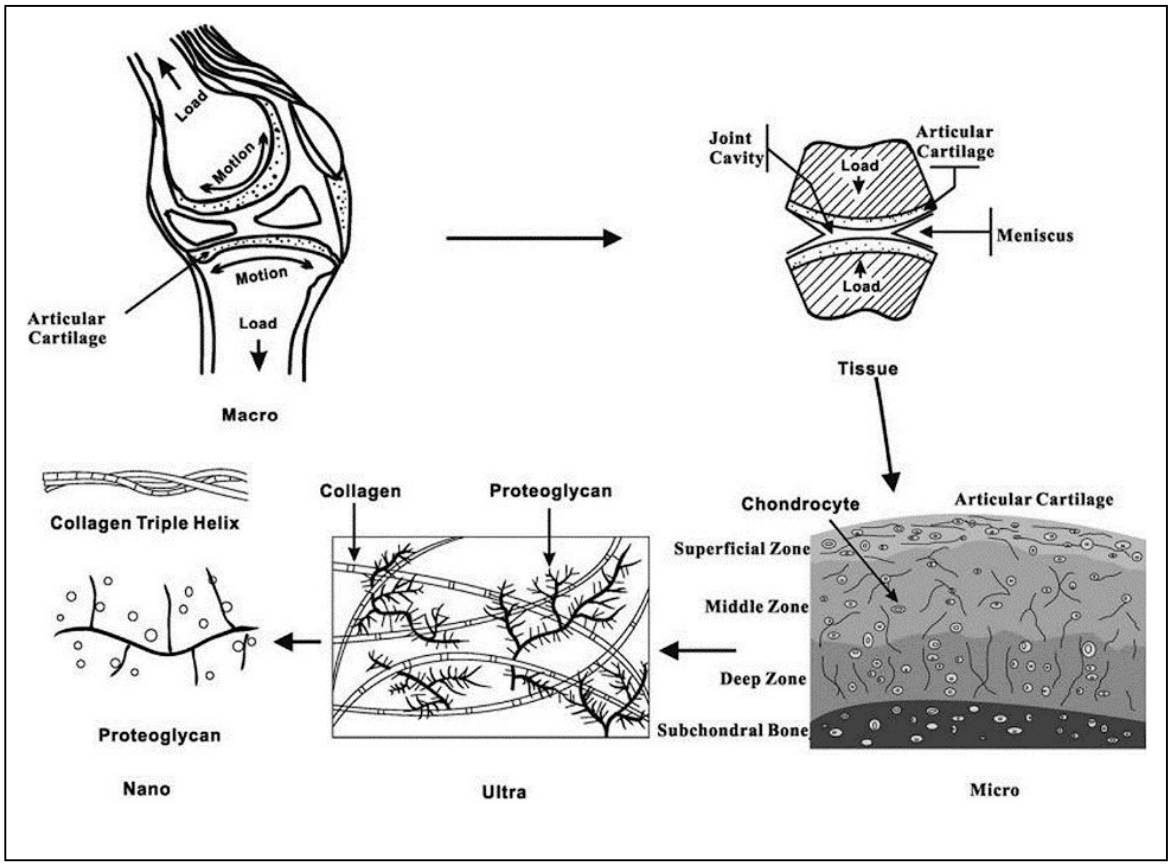

Note. Morphologically (micro-scale) articular cartilage mainly consists of chondrocytes (cells) and the surrounding extracellular matrix (ECM). There are three major components of ECM of articular cartilage, collagen (type II), proteoglycans (aggrecan), and water (not shown). Depth-dependently, cartilage can be divided into three sub-zones (superficial, middle, and deep zone). Reused with the permission of *Ge, Z., Li, C., Heng, B., & Cao, G. (2012). Functional biomaterials for cartilage regeneration. Journal of Biomedical Materials Research. Part A, 100, Figure 1. Page 2527*. Copyright by John Wiley and Sons.

Figure 2.2

ECM Composition of articular cartilage

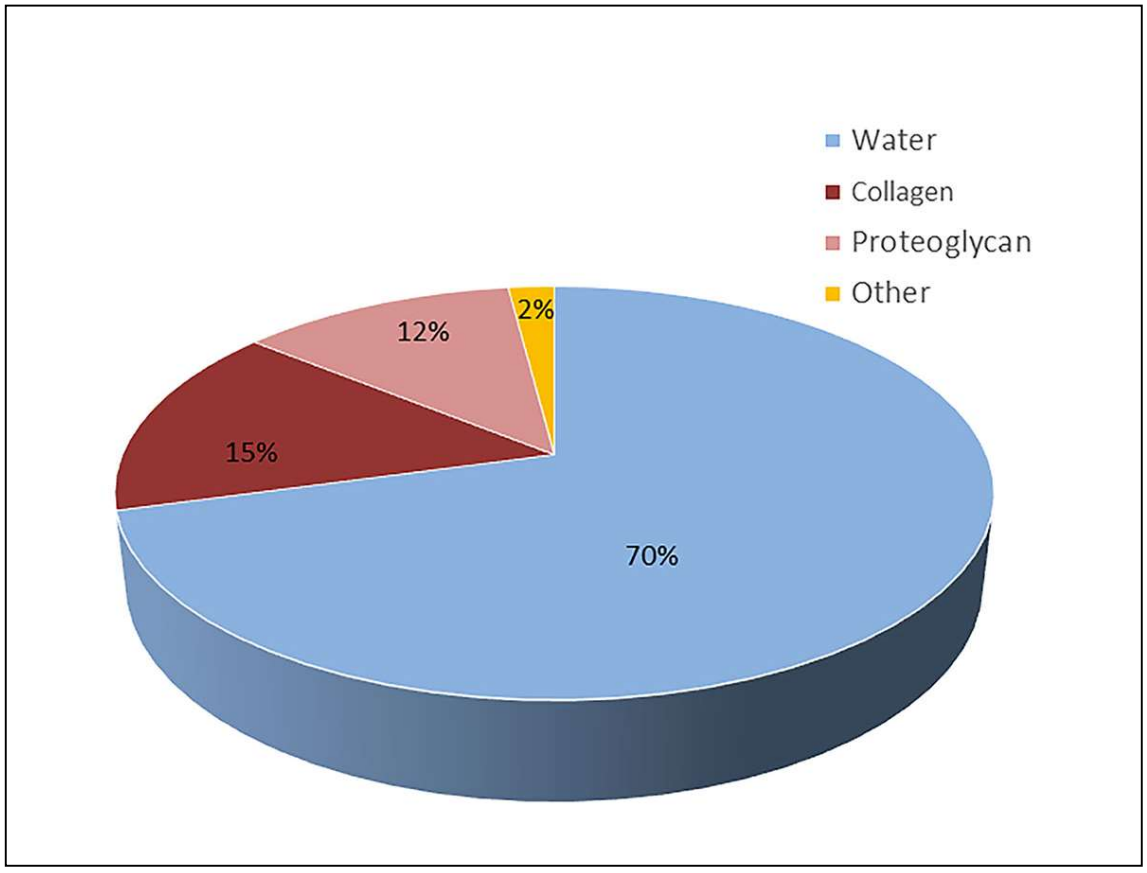

Note. Water (blue), constituting 65–80%, collagens (red) make up about 10–20% and proteoglycans (pink), constituting 10–15% of the wet weight of the AC, 1-3% other macromolecules. (yellow).

Figure 2.3

Schematic representation of stress relaxation and creep testing

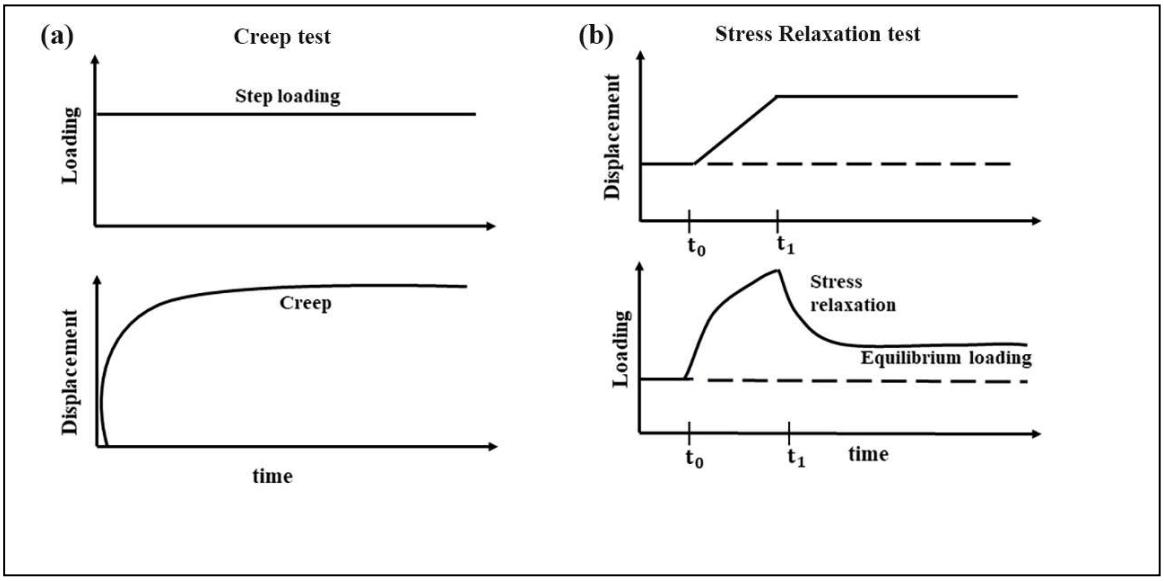

Note. In creep testing (a) a constant stress or load (time-independent) is applied (step loading) and the resultant change in displacement with time is measured. In stress relaxation testing (b), the initial displacement/strain is ramped (t_0 to t_1) to a certain value and kept constant. The load or applied stress relaxation is measured from peak (t_1) to equilibrium.

Figure 2.4

The schematics of collagen fibril structure and proteoglycan distribution in unloaded and loaded cartilage.

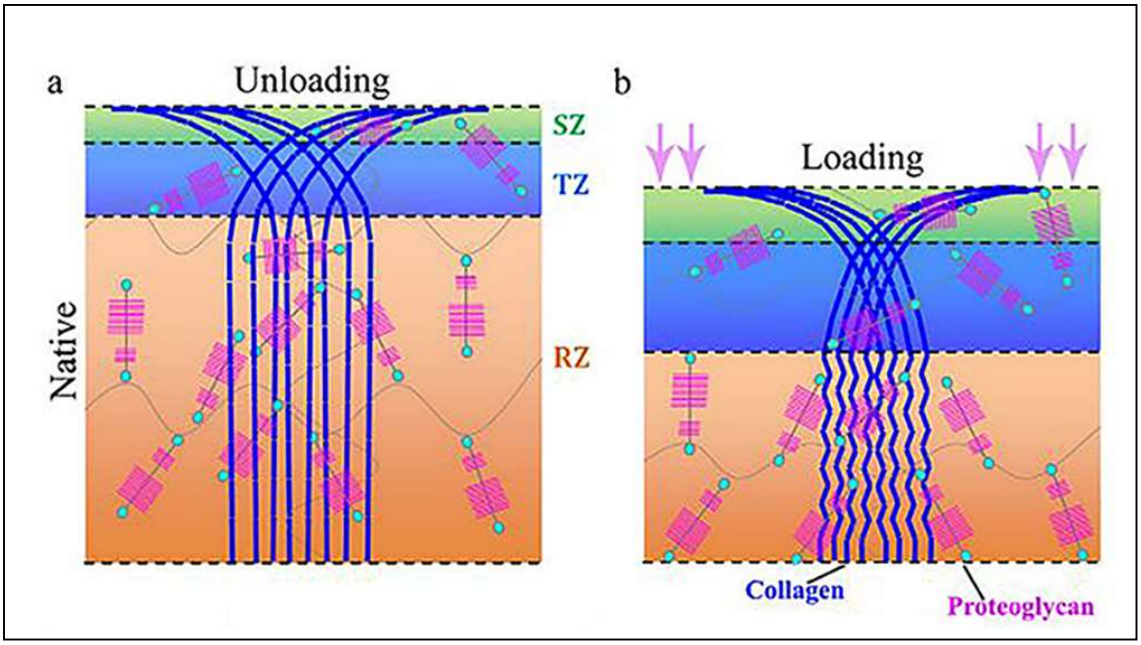

Note. Unloaded cartilage (a) with trizonal structure of collagen fibers and embedded PGs. Loaded cartilage (b), where collagen fibers in superficial and transitional zone deform easily but radial zone fibers resist compression and can have some type of localized zigzag patterns after loading. Reproduced with permission of *Wang, N., Badar, F., & Xia, Y. (2015). MRI properties of a unique hypo-intense layer in degraded articular cartilage. Physics in Medicine and Biology, 60(22), 8709–8721. Figure 5*. Copyright by IOP Publishing, Ltd.

Figure 2.5

Schematics of working principle of nuclear magnetic resonance (NMR).

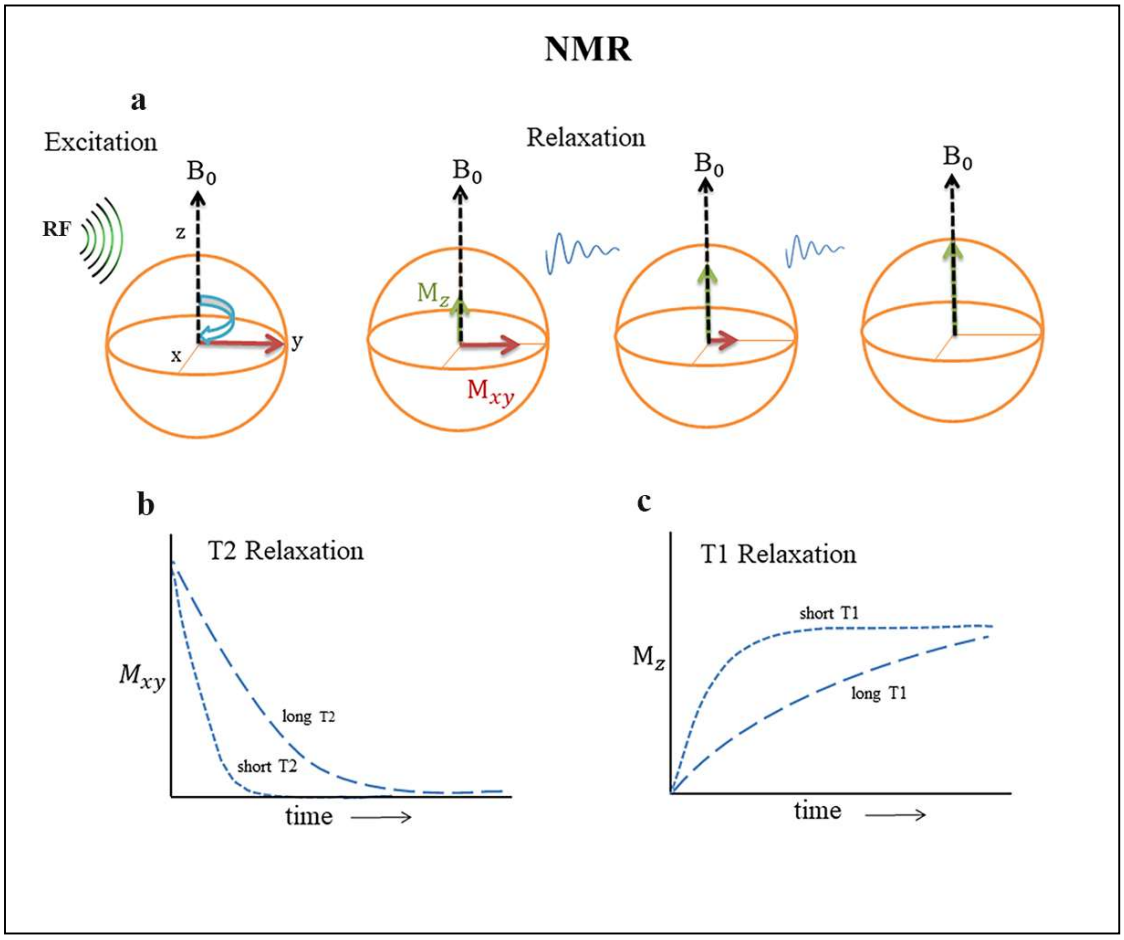

Note. (a) Excitation of protons in the magnetic field with radio frequency (RF) signal and subsequent relaxation in transverse (M_{xy}) and longitudinal direction (M_z). (b) Spin-spin relaxation (T2): time is taken for excited spinning protons to go out of phase with each other. (c) Spin-lattice relaxation (T1): time taken for the protons to realign with the external magnetic field (B_0).

Figure 2.6

The graphical sketches show the SE-based and magnetization-prepared pulse sequences (T2, T1, T1ρ).

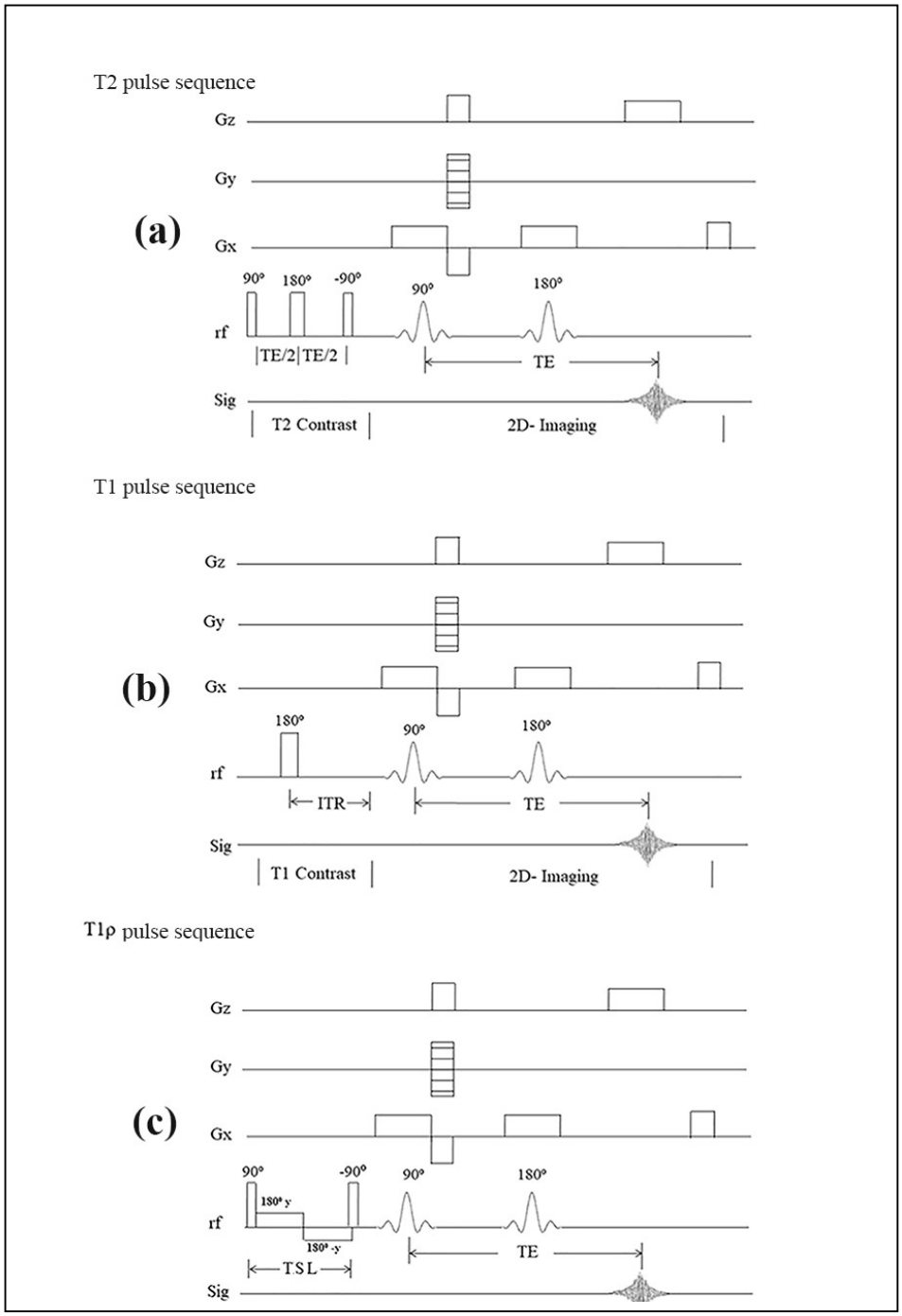

Note. (a) quantitative T2, (b) quantitative T1 and (c) quantitative T1ρ. (Gx- Slice selection gradient; Gy - Phase encoding gradient; Gz - read out gradient; TSL - spin lock period; TIR - inversion recovery time; TE - echo time). Originally published by *Mahar, R., Batool, S., Badar, F., & Xia, Y. (2018). Quantitative measurement of T2, T1ρ and T1 relaxation times in articular cartilage and cartilage-bone interface by SE and UTE imaging at microscopic resolution. Journal of Magnetic Resonance, 297, 76–85, Figure 1.* Reproduced with copyright permission.

Figure 2.7

Diagrammatic representations of linearly and circularly polarized light

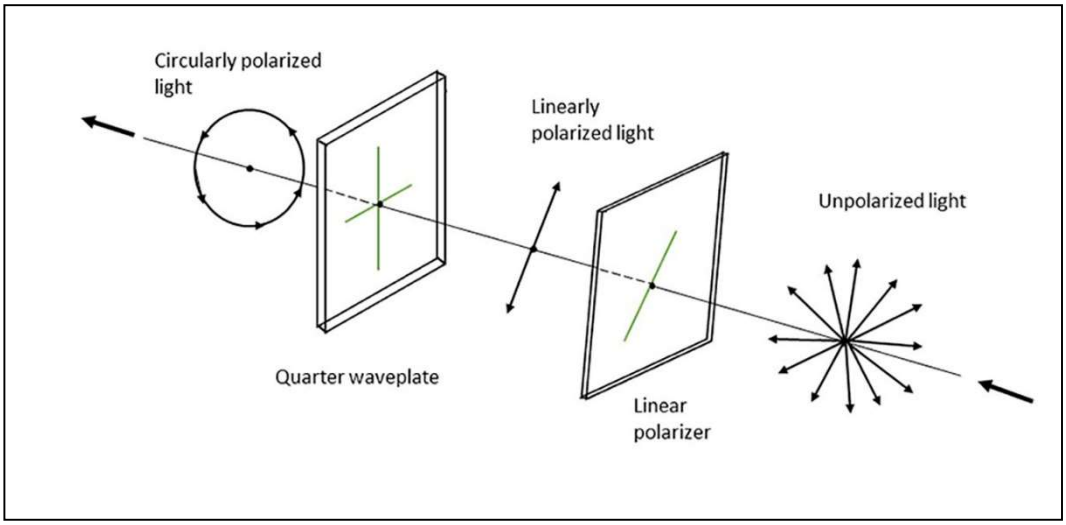

Note. First, an unpolarized light beam enters from the right and propagates through first a linear polarizer oriented at 45° and then a quarter wave plate with its fast axis oriented vertically. The linear polarizer transmits fully linearly polarized light, while the quarter wave plate delays the horizontal component of this light by ¼ wave relative to the vertical component, producing left-handed circularly polarized light.

CHAPTER THREE

QUANTITATIVE μMRI AND PLM STUDY OF RABBIT CARTILAGE AT SUB-10 μm RESOLUTIONS

3.1 Introduction

This chapter describes a high-resolution quantitative imaging study, which investigated the individual histological zones in the articular cartilage of rabbits. This study aimed to establish the baseline characteristic T2, T1ρ, and T1 relaxation times in humeral and femoral cartilage in rabbits using quantitative protocols in microscopic MRI (μMRI) and polarized light microscopy (PLM). To the best of our knowledge, this is the first correlated and quantitative MRI and PLM study of cartilage at sub-10 μm resolution, which establishes the baseline characteristics of normal healthy cartilage. The quantitative MRI relaxation data and PLM fibril structural data collectively show distinct features in tissue properties at different depths of cartilage, different in individual histological zones. The establishment of these characteristic features of rabbit cartilage would provide a solid foundation for future utilization of the rabbit model in the OA investigation.

3.2 Materials and methods

3.2.1 Sample preparation

Five healthy rabbits (12-15 weeks New Zealand White, male) were used in this study. The animals were sacrificed for an unrelated biomedical study. Ethical approval for the use of spare tissues in our study was waived by the Institutional Animal Care and Use Committee (IACUC) because the specimens were the discarded tissue. The animals

were frozen immediately at -80 °C after necropsy and thawed at 4 ˚C before the specimen harvesting. Five intact (i.e., unopened) shoulder joints (the scapula and humeral heads) and three femoral heads from the hip joints were harvested; each was placed in a glass tube and imaged by MRI at low resolutions (70-82 μm pixel size). A cotton swab soaked with 154 mM protease-inhibitor (PI) saline solution was placed in the tube to avoid tissue drying. After each intact joint/bone was imaged, a diamond saw cut each humeral head into 5 slices (Fig 3.1a, b) and each femoral head into 4 slices (Fig 3.1c, d), where each slice was about 1.8 mm thick.

Two cartilage-bone specimens were selected from each humeral head (Fig 3.1a), which resulted in n=10 for the humeral specimens. Similarly, one cartilage-bone specimen was harvested from each femoral head (Fig 3.1c), which resulted in n=3 for the femoral specimens. Each cartilage-bone specimen (each about 1.8×2×2.5 mm^3) had the full thickness of articular cartilage still attached to the underlying bone. These specimens were bathed in the PI solution and imaged using the same MRI system at high resolution (9.75 μm pixel size).

3.2.2 MRI experimental

The MRI system was a Bruker AVANCE II console and a 7 Tesla/89 mm magnet (Bruker, Germany). The intact joints and bones were first imaged sagittally using the standard multi-slice multi-echo sequence, where each joint/bone had 8 or 10 slices and each slice had 10 intensity images. This resulted in 80 or 100 intensity images for each joint/bone. Each slice had a thickness of 1 mm with a gap of 0.5 mm (humeral) or 0.8 mm (femoral) between any two neighboring slices. The humeral joint imaging had an echo time (TE) of 6.64 ms, and a repetition time (TR) of 2.5 s. The 2D acquisition matrix

was 256×256 and the field-of-view (FOV) was 18×18 mm², resulting in a 2D pixel size of 70.31 μm. The femoral head imaging had TE of 7 ms and TR of 2.20 s. The 2D acquisition matrix was 256×256 and FOV was 21×21 mm², resulting in a 2D pixel size of 82.03 μm.

All cartilage specimens (10 humeral and 3 femoral) were imaged for quantitative T2, T1ρ, and T1 at two orientations to the external magnetic field B_0, 0° and 55°, which allowed the tissue properties to be influenced by the max and min dipolar interaction (Xia, 1997). All quantitative imaging used TR of 2 s, TE of 6.47 ms, and a slice thickness of 0.8 mm. The 2D matrix was 256×128, which was reconstructed into 256×256; the FOV was 2.5×2.5 mm², resulting in a 2D pixel size for all cartilage specimens at 9.75 μm.

To determine the depth dependent T2 anisotropy across the full depth of rabbit cartilage, quantitative T2 imaging was repeated at a series of angular orientations to B_0 for two humeral specimens. The selected orientations form a series of discrete sampling points along the geometrical factor $(3\cos^2\theta - 1)^2$ that is proportional to the non-zero dipolar Hamiltonian.

3.2.3 Quantitative μMRI relaxation protocol

Quantitative T2, T1ρ, and T1 imaging adapted the concept of magnetization preparation (Haase et al., 1993; Xia, 1997), which consisted of a head segment to prepare the magnetization and an imaging sequence where all timings were constant. The head segment for T2 was a CPMG sequence (Xia, 1997; Zheng & Xia, 2009a), where the echo times were 2, 8, 16, and 38 ms for both humeral and femoral specimens. The head segment for T1ρ was a spin-lock sequence at a strength of 2000 Hz (N. Wang & Xia,

2011), where the spin-locking pulse lengths were 2, 8, 16, 38 ms for humeral and 2, 16, 40, and 60 ms for femoral. The head segment for T1 was an inversion-recovery sequence (Xia, 1997), where the inversion recovery times were 0, 0.8, 1.4, and 3.5 s for all specimens. Since only the timing of the head segment is altered during the experiments, the relaxation effect of the magnetization can be determined accurately.

3.2.4 Quantitative PLM protocol

After μMRI, 7 humeral cartilage-bone specimens and 3 femoral cartilage-bone specimens were fixated in 10% neutral buffered formalin overnight at 4 °C. A number of cartilage-bone slabs (5-6 mm thick) were cut at the center of the humeral head (at the location of the μMRI slices) across its width horizontally (hence containing both lateral and medial sides) and fixated. The fixated slabs and the cartilage specimens in μMRI were sent to a histology service (Yale Pathology Tissue Services, CT) to section into 6μm thin sections using the paraffin method. 30 sections from the humeral cartilage specimens, 6 sections from the femoral cartilage specimens, and 5 sections from the whole-width humeral head slabs were imaged using PLM.

The PLM system consists of a digital setup (Cambridge Research & Instrumentation, MA) that is mounted on a polarized light microscope (Leica, Germany). The output of the CCD camera was processed (Oldenbourg & Mei, 1995) to generate two quantitative images: the optical retardation and the angular orientation. Both quantitative images describe different aspects of the collagen matrix in cartilage (Xia et al., 2001a). All cartilage specimens were imaged at the identical orientation under a 10x objective which yielded a pixel size of 1.0 μm. All intact humeral heads were imaged under a 2.5x objective which yielded a pixel size of 4.0 μm.

3.2.5 Image and data analysis

On each T2 map of the humeral and femoral bone, a three-pixel-wide region of interest (ROI) was selected, which covered the entire thickness of cartilage and extended beyond the cartilage. The ROI was chosen at an identical location on the joint surface from which the small cartilage-bone specimens would be harvested for μMRI. From each ROI, one 1D profile along the cartilage depth was generated. On each quantitative 2D relaxation image, twenty parallel neighboring columns of data were selected and averaged to obtain one 1D profile. (Note that 20 consecutive columns in μMRI at 9.75 μm have approximately the same tissue width as 3 consecutive columns in the intact humeral cartilage resolution at 70.31 μm.) On each quantitative PLM image, 195 parallel neighboring columns, which would have approximately the same width as the slice thickness in μMRI, were averaged to produce one 1D profile.

Since the averaging from 2D ROI to 1D profiles in μMRI and PLM occurs perpendicular to the tissue depth, the spatial resolutions of the 1D profiles along the tissue depth are still 70.31 μm for MRI of the intact humeral, 82.03 μm for MRI of the femoral head, 9.75 μm for MRI of the cartilage-bone specimens, and 1 μm for PLM of the intact joint/bone. All 2D images and 1D profiles, where each came from one independent imaging experiment, used identical scaling and settings without any additional adjustment. The post-acquisition analysis used the public-domain software ImageJ (NIH) and a commercial software KaleidaGraph (Reading, PA).

3.3 Results

3.3.1 MRI of Intact Joint and Small Cartilage-bone Specimens at Different Resolutions

Fig 3.2a and Fig 3.2c showed four intensity images for one intact humeral joint and one intact femoral head respectively, together with their quantitative T2 images. Note that the surface of the humeral cartilage was bordered by synovial fluid and other tissues since the shoulder joint was intact; in comparison, the surface of the femoral cartilage was bordered with air (which appeared black in the intensity images) since only the femoral head was imaged in the glass tube (due to the large size of the acetabulum of the hip). Fig 3.3b and Fig 3.3d showed the intensity and T2 images for one humeral specimen and one femoral specimen respectively. The high-resolution images of humeral and femoral cartilage appear similar. A thin black line was more visible near the femoral surface (Fig 3.2d) than the humeral surface (Fig 3.2b), indicating a lower T2 in the surface of the femoral cartilage.

3.3.2 Quantitative relaxation measurements at 9.75 μm resolution

Fig 3.4 shows the quantitative T2, T1ρ, and, and T1 images and profiles in both humeral and femoral cartilage at 9.75μm resolution, where the same tissue block was imaged twice using the identical protocol at two different orientations in B_0. These images and profiles reveal similarities and differences between humeral and femoral cartilage in rabbits, and between rabbit and canine humeral cartilage in the literature (Xia et al., 2001a, Lee & Xia, 2013). Between humeral (Fig 3.4a-3.4c) and femoral (Fig 3.4d-3.4f) cartilages in rabbits, the relaxation images and profiles appear similar at 55˚ to B_0, at which the dipolar interaction has the weakest influence to spin relaxation. This is

likely because both cartilages belong to the same type of ball-and-socket joint and hence are structured similarly. At 0˚ to B_0 (which has the strongest dipolar influence to spin relaxation), the shape of the T2 profile in femoral cartilage is well defined and narrower than humeral cartilage, the meaning of which at the fibril structure level needs further investigation.

Between the humeral cartilage in rabbits (Fig 3.4a-3.4c) and canines in our previous studies using the same protocols (Xia et al., 2001a; Xia, Moody, Alhadlaq, et al., 2002), the depth-dependent characteristics of these relaxation times in rabbit cartilage match broadly the corresponding characteristics in canine cartilage, where the bell-shaped curve in the T2 profiles (Fig 3.4a, 3.4d) implies a classical three-zone structure in cartilage, which can be used to sub-divide cartilage thickness into multiple histological zones (Lee & Xia, 2013; Xia et al., 2001a). One noticed that the T2 profile at 55˚ was not as uniform in values across the tissue depth, which should have an anatomic origin at the fibril level in the tissue. Using the established criteria (Lee & Xia, 2013; Xia et al., 2001a), the zonal division of cartilage thickness was carried out on all μMRI images (Table 3.1). In both humeral and femoral cartilages, SZ is about 21 μm thick, just over 2 pixels in μMRI at 9.75 μm/pixel. This thin thickness of SZ in rabbit cartilage puts a high-resolution requirement on μMRI and any other imaging tools in the study of rabbit cartilage. A peculiar feature in the humeral data is that the L blocks were consistently thicker than the C blocks, which suggests a topographical variation of cartilage thickness over the joint surface (L and C blocks were two adjacent tissue blocks, about 1.8 mm apart on the joint surface). Table 3.2 summarizes the zonally averaged relaxation times, based on the zonal thickness data in Table 3.1. The biggest zonal variations are T2 at 0˚,

while the zonal data in T1ρ and T1 have much less depth dependence and little orientational dependence.

Fig 3.5 compares the T2 profiles from the T2 images in Fig 3.4. Two features can be identified for humeral cartilage (Fig 3.5a). First, for the deeper part of humeral cartilage (about 75% of the total cartilage), T2 profiles at both resolutions match each other. Second, for the top 25% of the tissue, the low-resolution imaging missed the critical feature of the surface cartilage. The continuously increased T2 values towards the articular surface (the depth of 0) and beyond the articular surface (into the neighboring space) in Fig 3.5a demonstrates the consequence of low-resolution MRI of cartilage, which averaged cartilage with the surrounding synovial fluid – two tissues that have very different T2 relaxation times. Similarly, the low-resolution MRI of femoral cartilage (Fig 3.3b) missed out on the critical features of the surface cartilage (the top 25%), where the cartilage signal was reduced because of the averaging with air near the surface. In contrast, μMRI can resolve the T2 characteristics of the surface tissue faithfully (Fig 3.5), which represent the superficial and transitional zones.

3.3.3 Depth-dependent T2 anisotropy

To study the depth-dependence of T2 anisotropy, two humeral specimens were each imaged at six different orientations to B_0. Fig 3.5a showed one set of six T2 profiles from six independent T2 experiments, plotted together without additional scaling. These profiles demonstrated that T2 anisotropy in rabbit humeral cartilage is strongly depth-dependent and orientational-dependent, with the biggest anisotropy around 80 μm to 160 μm depths, representing the upper part of the radial zone. A close examination can be done by plotting T2 anisotropy at every tissue depth (every 9.75 μm). Four such plots are

shown in Fig 3.5b. T2 anisotropy in rabbit humeral cartilage is prominent at 0 μm and stays equally prominent at 9.75 μm (not shown) – both pixels represent SZ cartilage. As the depth goes deeper, T2 anisotropy weakens and remains nearly identical within the depths of 29.25 μm to 48.75 μm, which signals TZ cartilage. However, T2 anisotropy remains noticeable even at its weakest (up to 40%), which reflects a residual fibril structure in TZ. From the depth of 68.25 μm, T2 anisotropy becomes stronger again, reaching a max at 351 μm (near the bottom of RZ). These pixel-by-pixel features in the depth-dependent T2 anisotropy precisely reflect the variations in the collagen organization across the entire thickness of cartilage (Xia, Moody, & Alhadlaq, 2002; Zheng et al., 2011; Zheng & Xia, 2009b).

3.3.4 Quantitative PLM results

The angle and retardation maps from the quantitative PLM represent the pixel-averaged fibril orientation and fibril organization of the collagen matrix in cartilage respectively. Fig 3.6 showed the retardation image of an intact humeral head. Several observations can be noted. First, there is a dark 'line' in the retardation image at ~50 μm below the articular surface, which represents the location of the least organized fibers in tissue (the center of TZ). Second, this dark line gradually vanishes towards both peripherals, which suggests the collagen architecture in peripheral cartilage is different from the central region. Thirdly, humeral cartilage has strong topographical variation in its thickness, from ~250 μm at the joint center to ~500 μm at the peripherals. Although this thickness variation is significant, it is not as complex as in some other joints such as the tibia (refer to Fig 1.10 in Chapter 1 of the book (Xia & Momot, 2016)). Finally, our cartilage specimens for μMRI and PLM were harvested from a slightly off-center

location in the humeral head, which explains the consistent thickness difference between our L specimens and our C specimens (Table 3.1). Fig 3.7 showed the quantitative PLM results from the same humeral specimen from which the μMRI data were discussed (Fig 3 4). These PLM images from rabbit cartilage are very similar to the PLM images from canine cartilage ((Xia et al., 2001a). Briefly, the depth-dependent retardation (Fig 3.7a) had its lowest values about 50 μm below the articular surface, which indicates the center of TZ; the high retardation values at the articular surface indicate the fine fibril organization at the articular surface while the high retardation values in the deep cartilage represent the fibril structure of RZ (closely and more densely packed). In the angle image (Fig 3.7b), the blue and red colors in this color scale showed ~85˚ orientational difference between the SZ and RZ fibrils. The tide mark in this rabbit tissue was not quite visible as in some mature cartilage (Xia et al., 2001a). Femoral cartilage was also analyzed by PLM, which yielded similar results as in humeral cartilage. Fig 3.7c showed one set of quantitative PLM profiles (from Fig 3.7a and 3.7 b), which were averaged over 6 tissue sections from one humeral specimen, together with the T2 profile from the same tissue block (Fig 3.4a). These profiles solidify the descriptions and conclusions for the angle and retardation images in the early part of this section.

3.3.5 μMRI zones vs histological zones correlation

Using the established criteria (Lee & Xia, 2013; Xia et al., 2001a), the zonal division of cartilage thickness was carried out on all PLM images from 30 histological sections (from 5 humeral specimens). PLM zones from the humeral specimens were compared with the corresponding μMRI zones from the same specimens (Table 3.3). Some disagreements can be noted for the thin zones between μMRI and PLM, which is

likely caused by the difference in the imaging resolution (9.75 μm in μMRI, 1.0 μm in PLM). The correlations in the total tissue thickness and the radial zone are satisfactory. Similarly, the zonal division for femoral cartilage has also been carried out, where the μMRI and PLM results from the same femoral specimens were compared for their zonal thicknesses. In femoral cartilage, SZ was ~ 7-9 %, TZ 8-9 %, and the radial zone was ~82% of the total cartilage.

3.4 Discussion

Among many MRI parameters that could be used to study cartilage degradation, T2, T1ρ, and T1 relaxation times are currently the most commonly used parameters in clinical MRI of OA (Xia, 2013). These parameters are sensitive to molecular motions and their interactions with the tissue surroundings. This study has successfully quantified T2, T1ρ, and T1 in both humeral and femoral cartilage in rabbits at 9.75 μm resolution. To the best of our knowledge, these μMRI results are the first quantitative characterization of the entire depth of humeral and femoral cartilage in rabbits at a sub-10 μm resolution. The complementary use of quantitative PLM in this study further enhances the μMRI results. Given our experience in canine studies (Alhadlaq et al., 2004; Lee et al., 2016; Lee & Xia, 2013; Xia, 1997; Xia, Alhadlaq, et al., 2008), the depth-dependent features of T2, T1ρ, and T1 in rabbit cartilage were found to be like those in canine cartilage. This similarity implies a classical three-zone structure in rabbit cartilage and provides possibilities for doing comparative analyses between canine studies and leporine studies.

3.4.1 Challenges in studying rabbit cartilage – age, thickness, topographical variations.

There are at least three challenges in using the rabbit model for OA research. First, the growth plates in rabbit joints do not close until 6-9 months, beyond which those

animals can be considered skeletally mature (Bland & Ashhurst, 1996; Burr, 2002; Isaksson et al., 2010; Turunen et al., 2011). The animals in this study (also in many studies in the literature) were 3-4 months old, hence skeletally immature. However, the same studies (Kavanagh & Ashhurst, 1999; Turunen et al., 2011) also noted that the collagen matrix of articular cartilage in mature rabbits appeared to be "similar" to that at 12–14 weeks. In contrast to this similar conclusion between immature and mature rabbits, some previous μMRI and PLM studies of canine humeral cartilage have found vastly different characteristics between young and mature canines (Xia et al., 2003; Xia, Moody, Alhadlaq, et al., 2002). In any case, the maturity of rabbit tissues should be noted for any study that creates an injury or intervention in the tissue and waits for a time for its development, as well as for any comparative analyses of the rabbit data in the OA literature.

Second, rabbit cartilage is thin, a few hundred microns in thickness in the largest joints. This thin thickness possesses challenges for several types of studies, including diagnostic imaging and surgery. In this imaging study, based on the birefringent information at the 1.0 μm optical resolution, we determined the zonal thicknesses for the central part of humeral cartilage, where SZ and TZ were just over 30 μm each. These findings demonstrate that high resolution (e.g., approximately 10 μm) is required to analyze zonal differences in the rabbit cartilage. One subtle but important reason to use two resolutions to study rabbit cartilage in this MRI study comes from the imaging scaling in the MRI of cartilage (Xia, 2007). In this study, for a nominal thickness of 300-400 μm in rabbit cartilage, there were approximately 4-5 pixels in our low-resolution MRI of intact bone heads (70-82 μm pixel size) and 35 pixels in our μMRI of tissue

blocks (9.75 μm pixel size). In contrast, although human knee and hip cartilage are much thicker, clinical MRI also has a bigger pixel size, which commonly resolves human cartilage in 3-5 pixels. Consequently, our low-resolution MRI of rabbit cartilage mimics almost exactly the tissue averaging situation in clinical MRI of human cartilage (Xia, 2007). Hence our experimental methodology and approach can be adapted to perform many OA projects using the rabbit model.

Thirdly, most of the tissue characteristics in cartilage change topographically over a joint surface, likely due to the consequence of load-bearing and motional patterns for a particular joint and a particular animal. Even for a ball-and-socket joint such as the humeral head in rabbits (which has considerably simpler variations than a knee joint), the thickness of cartilage ranges from about 250 μm at the center to twice the thickness at the periphery (Fig 3.6). These topographical variations exist on any joint surface (Xia, 2000a; Xia et al., 2003; Xia, Moody, Alhadlaq, et al., 2002). In this study, slightly off-center harvesting of the cartilage-bone specimens from the humeral head has led to noticeable variations in the quantitative measurement of the tissue properties by both μMRI and PLM (Fig 3.4-3.7). In μMRI results, for example, we can attribute the non-uniformity of the T2 depth profile at 55˚ (Fig 3.4) to be the results of these off-center specimens, where the collagen organization was not entirely perpendicular to each other between the superficial and radial fibrils, which was also confirmed by the PLM results (Fig 3.7c). These topographical variations can make the interpretation of the individual study difficult and the comparison among different studies in the literature challenging.

3.4.2 Limitations of study

This study has several experimental limitations. First, five animals were used in this study, from which five intact shoulder joints and three femoral heads from the hip joints were harvested. These animals belong to a total of over 20 nearly identical rabbits that we obtained from the same source and studied in our lab in different projects. We can confirm that the μMRI and histology features from the tissues of other animals were highly consistent with the presentation in this study. Second, quantitative imaging can be influenced by the topographical variation of cartilage, i.e., the surface site where the specimen is harvested and studied. This variation could be significant for joints such as the knee. In humeral and femoral heads, by contrast, our experience indicates that the topographical variation has a much smaller influence on cartilage properties and hence the limited sampling sites in this study can represent most of the joint surface (apart from the peripherals). Third, this study demonstrates that the depth-dependent characteristics of the T2, T1ρ, and T1 relaxation times in humeral and femoral cartilage in rabbits are similar to those in canine cartilage (Xia et al., 2001a; Xia, 2013). This similarity implies a classical three-zone structure in the rabbit cartilage and the possibility of doing comparative analyses between canine studies and leporine studies.

Table 3.1a

Averaged zonal thicknesses based on the T2-0° profiles of humeral cartilage (n = 10 specimens)

Specimen	Superficial Zone (µm)	Transitional Zone (µm)	Radial Zone (µm)	Total Tissue (µm)
1L	19.50	48.75	234.25	302.25
IC	19.50	48.75	224.25	292.50
2L	19.50	58.50	292.50	380.25
2C	29.25	48.75	234.25	302.25
3L	19.50	48.75	380.25	458.25
3C	19.50	48.75	360.75	429.00
4L	19.50	58.50	380.25	458.25
4C	19.50	48.75	302.25	370.50
5L	19.50	48.75	399.75	468.00
5C	29.25	58.50	370.50	458.25
Mean ± σ	**21.45 ± 1.3**	**51.67 ± 1.6**	**317.90 ± 21.8**	**391.95 ± 22.5**
%	**6**	**13**	**81**	**100**

Note. σ represents the standard error. % is the relative percent thickness of each zone based on the total thickness.

Table 3.1b

Averaged zonal thicknesses based on the T2-0° profiles of femoral cartilage (n = 3 specimens)

Specimen	Superficial Zone (µm)	Transitional Zone (µm)	Radial Zone (µm)	Total Tissue (µm)
1C	19.50	29.25	253.50	302.25
2C	29.25	48.75	282.75	360.75
3C	29.25	39.00	292.50	360.75
Mean ± σ	**26 ± 3.3**	**39 ± 5.6**	**276.25 ± 11.7**	**341.25 ± 19.5**
%	**8**	**11**	**81**	**100**

Note. σ represents the standard error. % is the relative percent thickness of each zone based on the total thickness.

Table 3.2a

Averaged orientation dependent (0˚, 55˚) zonal T2, T1ρ, and T1 relaxation times based on the zone division of humeral cartilage (n = 10 specimens).

	T2 (ms)		T1ρ (ms)		T1 (s)	
	0˚	55˚	0˚	55˚	0˚	55˚
SZ	20.46 ± 1.55	51.31 ± 3.87	86.32 ± 2.92	88.82 ± 3.97	1.25 ± 0.02	1.32 ± 0.02
TZ	37.96 ± 1.66	58.99 ± 2.75	92.49 ± 3.12	93.60 ± 3.52	1.21 ± 0.02	1.21 ± 0.01
RZ-I	12.04 ± 0.58	62.94 ± 2.91	90.84 ± 2.67	103.63 ± 2.67	1.26 ± 0.03	1.27 ± 0.02
RZ-II	7.24 ± 0.61	37.55 ± 1.93	53.97 ± 2.27	65.67 ± 1.85	0.95 ± 0.03	1.01 ± 0.02

Note. Data are in mean ± standard error. RZ-I and RZ-II are the top and bottom equal halves of the radial zone.

Table 3.2b

Averaged orientation dependent (0˚, 55˚) zonal T2, T1ρ, and T1 relaxation times based on the zone division of femoral cartilage (n = 3 specimens)

	T2 (ms)		T1ρ (ms)		T1 (s)	
	0˚	55˚	0˚	55˚	0˚	55˚
SZ	17.16 ± 3.59	48.10 ± 7.47	68.34 ± 3.88	76.01 ± 5.77	1.18 ± 0.09	1.29 ± 0.08
TZ	33.30 ± 3.73	51.15 ± 1.82	76.30 ± 3.23	79.94 ± 4.72	1.21 ± 0.01	1.26 ± 0.04
RZ-I	10.90 ± 0.65	46.19 ± 3.60	82.32 ± 9.06	89.58 ± 1.06	1.23 ± 0.05	1.27 ± 0.03
RZ-II	4.30 ± 2.10	25.89 ± 2.50	35.63 ± 4.22	51.25 ± 2.19	0.75 ± 0.07	0.90 ± 0.06

Note. Data are in mean ± standard error. RZ-I and RZ-II are the top and bottom equal halves of the radial zone.

Table 3.3

Correlations of μMRI vs PLM zonal thickness (μm)

	μMRI Thickness	**PLM Thickness**	**t-probability**
SZ	21.45 ± 1.95	29.09 ± 2.36	0.04
TZ	52.65 ± 2.38	31.69± 1.24	<0.001
RZ	366.60 ± 16.82	379.68 ± 15.76	0.58
Total Tissue	440.70 ± 18.13	440.46 ± 16.82	0.95

Note. Correlations of the averaged zonal thickness in humeral cartilage between μMRI (n = 5 cartilage specimens) and PLM (n = 30 histological sections from 5 μMRI specimens at 6 sections per specimen). Data are in mean ± standard error. The t-probabilities were calculated using Student t-test analysis.

Figure 3.1

Rabbit humeral and femoral head and histological sections

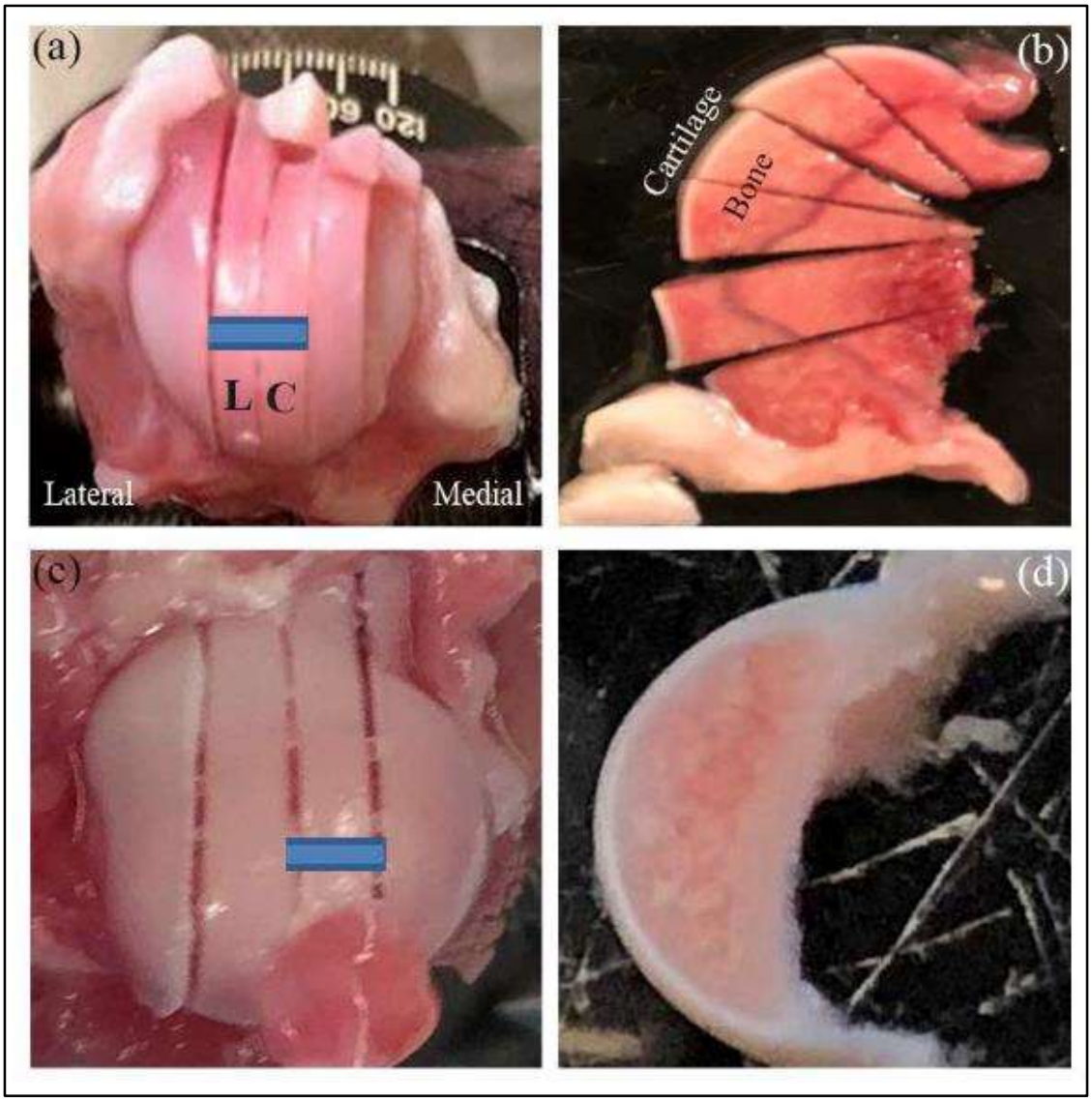

Note. The top left and right corners are the greater and lesser tubercles respectively (a). After an MRI of the intact shoulder joint, four cuts were made over each intact head, as shown in the photo. The two peripheral slabs were not used in specimen imaging because of their irregularity. The second and third slabs (each about 1.8 mm thick) were selected for the quantitative μMRI and PLM. The rectangular shape marks the approximate location of the imaging slice in the high-resolution imaging. (b) The side view of a central slab cut into small specimen blocks, through the humeral head. (c) A femoral head, where a central slab is shown in (d).

Figure 3.2

T2-weighted intensity images and T2 maps of an intact shoulder, the femoral head (80 µm/pi,xel) and small cartilage bone plugs (9.75 µm/pixel)

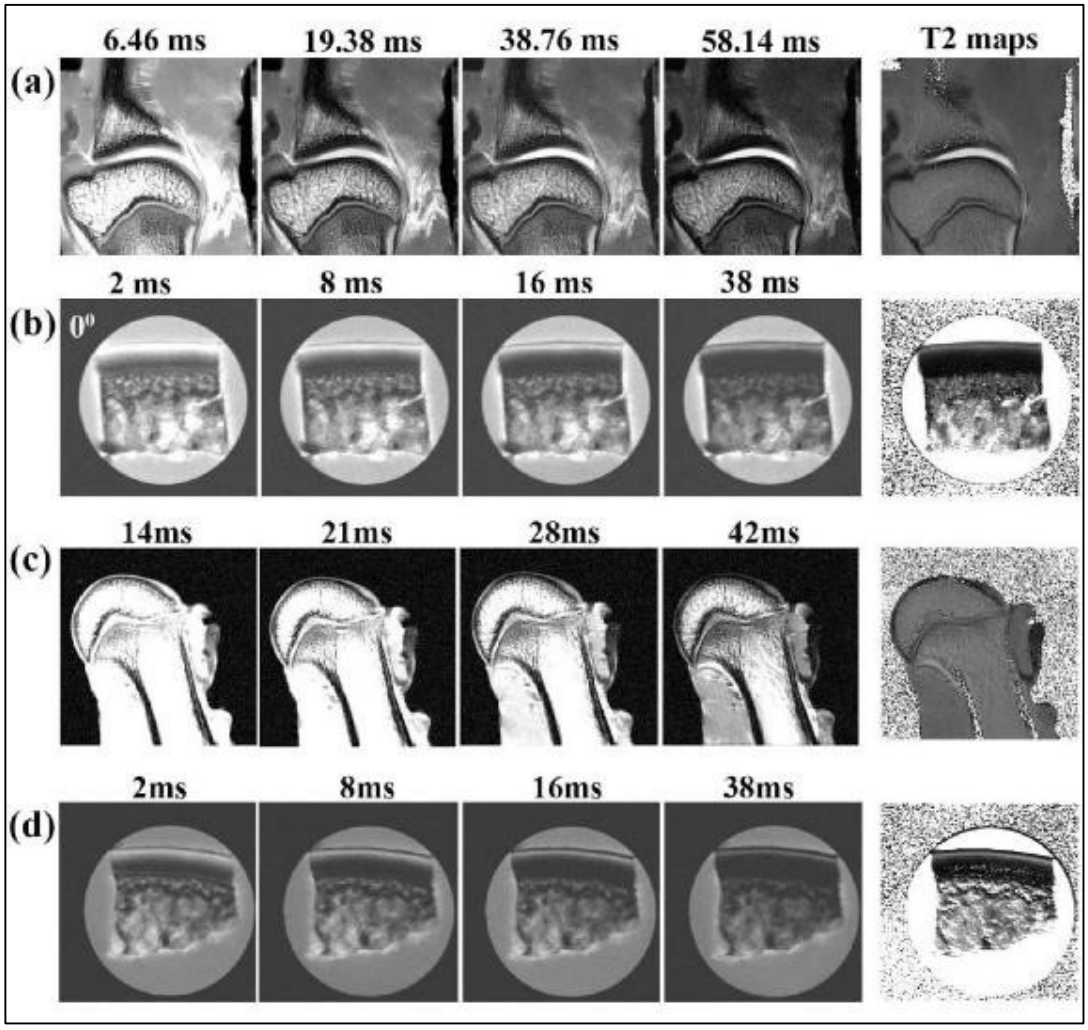

Note. An intact shoulder joint (a) and a humeral cartilage specimen (b) at different echo times, at the pixel resolution of 70.31 μm and 9.75 μm respectively. (c) and (d) show similar images from a femoral head, at the pixel resolutions of 82.03 μm and 9.75 μm respectively. The quantitative T2 images from each series of ten T2-weighted intensity images were shown on the most-right images. Since the direction of the magnetic field, B_0 was vertically up in the figure, the orientation of the cartilage specimens was 0˚ to B_0 (Fig 3.2b, 3.2d), which was like the surface orientation of the tissue when the intact joint was imaged in the magnet in sagittal view (Fig 3.2a, 3.2c). All T2 images were displayed with the same up/low limits (0-100 ms).

Figure 3.3

The depth dependent T2 profiles from the T2 images at low (~80 µm/pixel) and high (9.75 µm/pixel) resolution

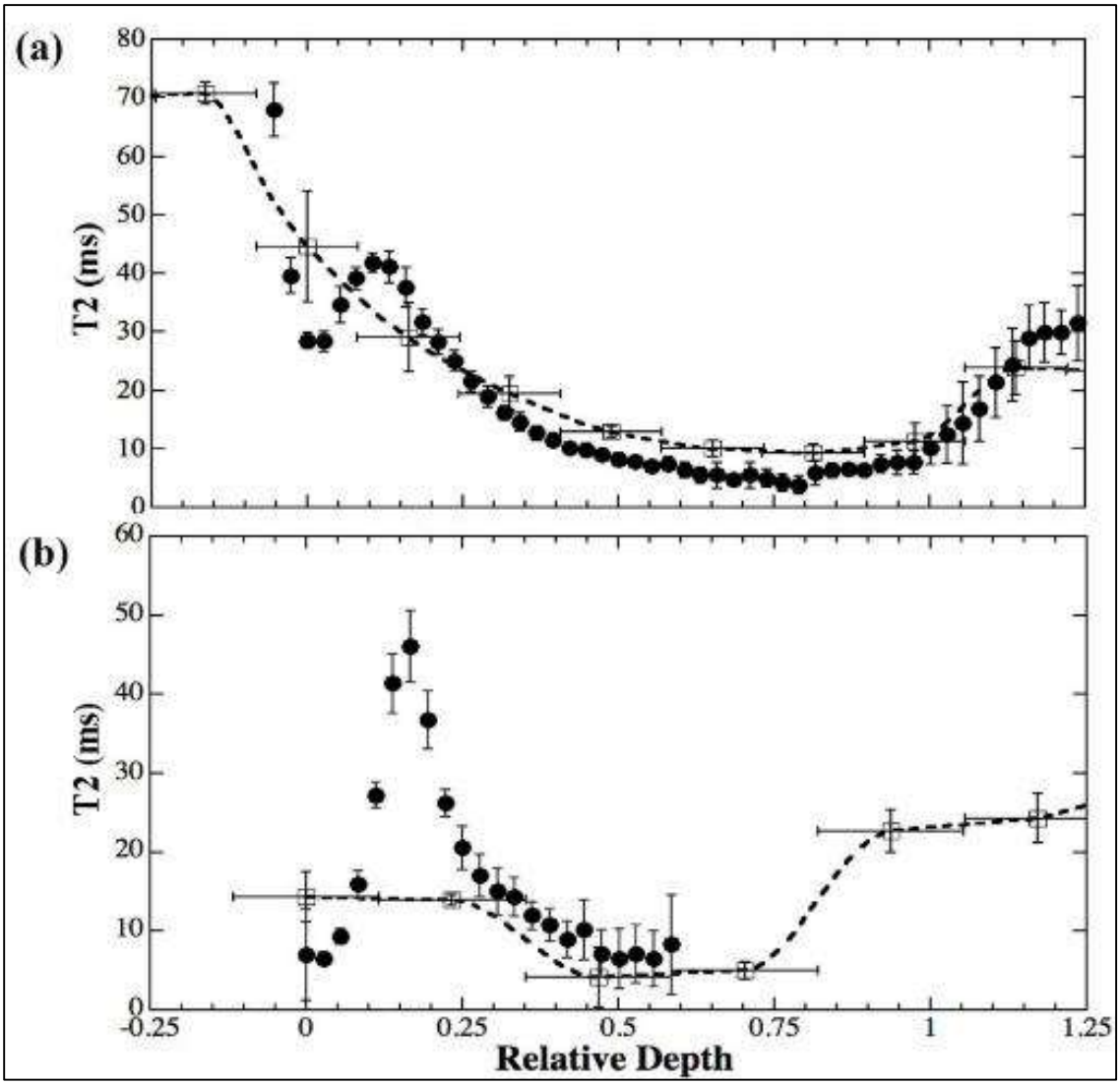

Note:(a) humeral cartilage at 70.31 µm/pixel (open squares) and 9.75 µm/pixel (solid dots) and (b) femoral cartilage at 82.03 µm/pixel (open squares) and 9.75 µm/pixel (solid dots), respectively. The depth scale is relative, with 0 marking the articular surface and 1 marking the cartilage-bone interface. The dashed lines fit through the T2 profiles in the low-resolution MRI. The vertical error bars represent the standard deviation of the data, and the horizontal error bars in the low-resolution mark the pixel sizes. Note that in (b), µMRI T2 (0˚) are shown till the tissue depth of 0.6, after which the image intensities become very low and the calculated T2s become unreliable.

Figure 3.4

The quantitative T2, T1ρ, and T1 images and their respective 1 D profiles at 9.75 μm/pixel for humeral and femoral cartilage

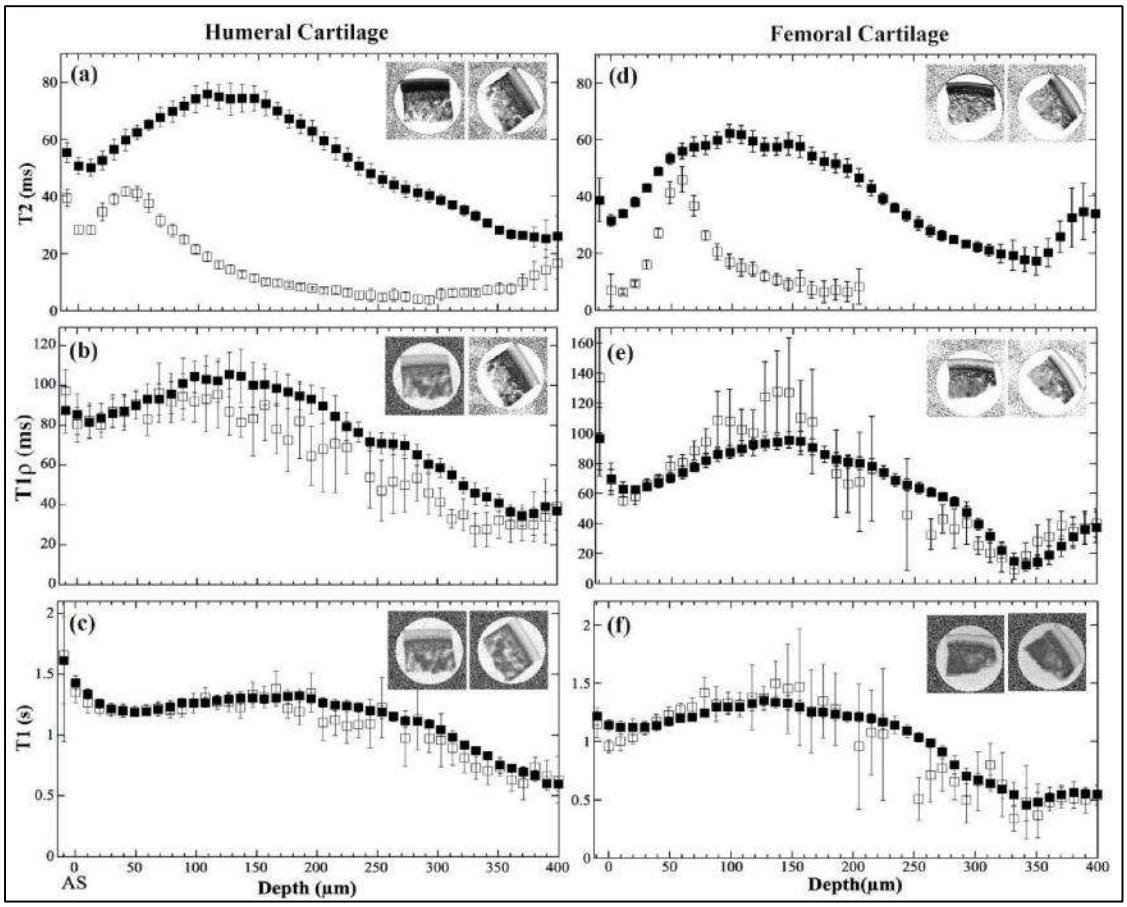

Note. (a)-(c) humeral cartilage, and (d)-(f) femoral cartilage. The solid dots are the profiles at the 55˚ specimen orientation, while the open squares are the profiles at the 0˚ specimen orientation to the external magnetic field B_0.

Figure 3.5

Depth-dependent T2 profiles and the plots of T2 anisotropy of humeral cartilage.

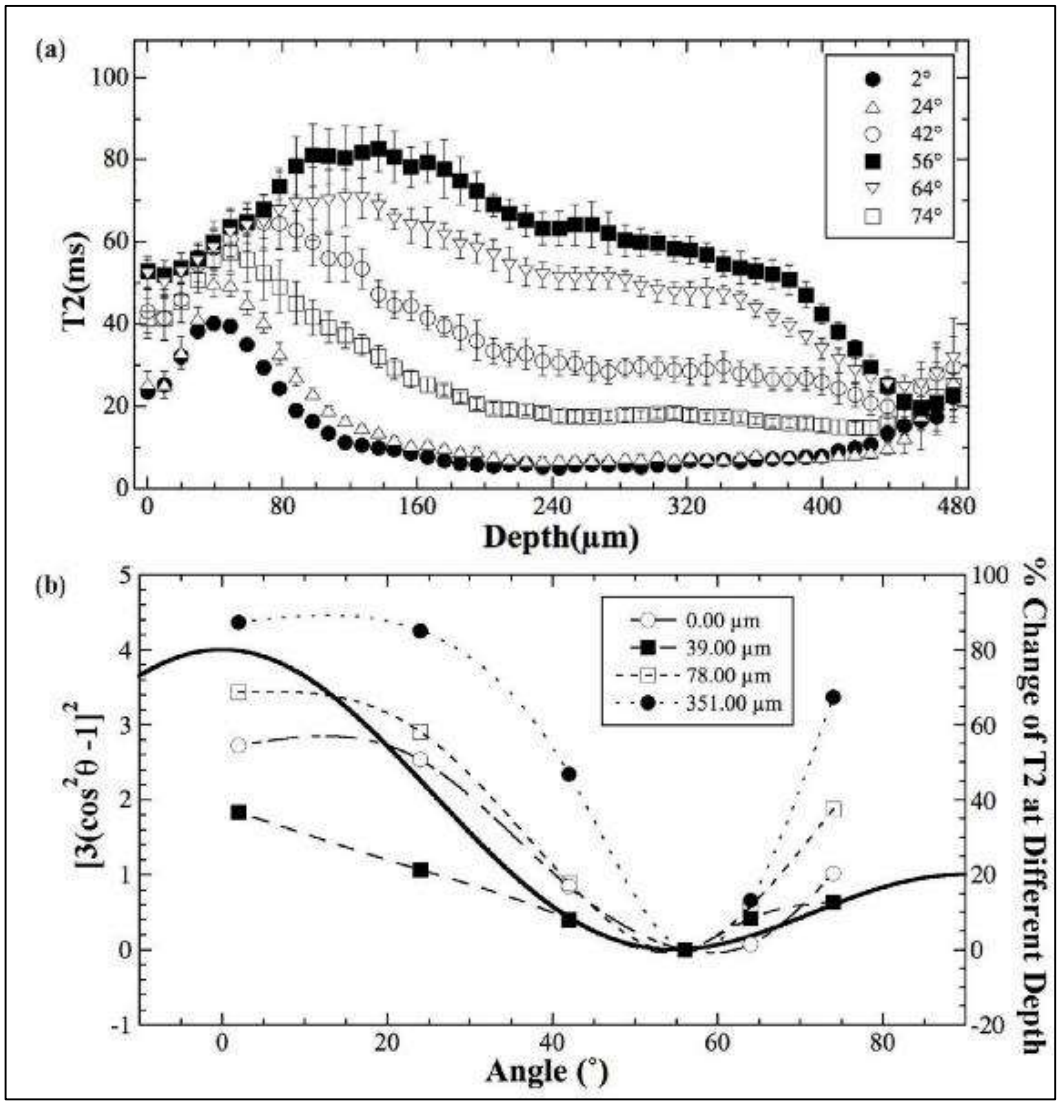

Note. T2 profiles at six orientations to B_0, which follow the geometric factor in the dipolar interaction, $(3\cos^2\theta-1)^2$, that manipulates T2 relaxation in MRI. (b) The plots of T2 anisotropy (% change in T2 to the 55˚ data, as a function of the specimen orientation) at four tissue depths (at a 9.75 μm tissue depth step): 0 μm represents the first layer of the superficial zone; 39 μm is inside the transitional zone; 78 μm marks the boundary between the transitional zone and radial zone, and 351 μm locates deep in the radial zone. The solid line plots the $(3\cos^2\theta-1)^2$ in the dipolar interaction that dominates the T2 characteristics in the articular cartilage.

Figure 3.6

The retardation images from an intact humeral head of the shoulder joint, imaged by polarized light microscopy with a 2.5x objective (4 µm pixel resolution)

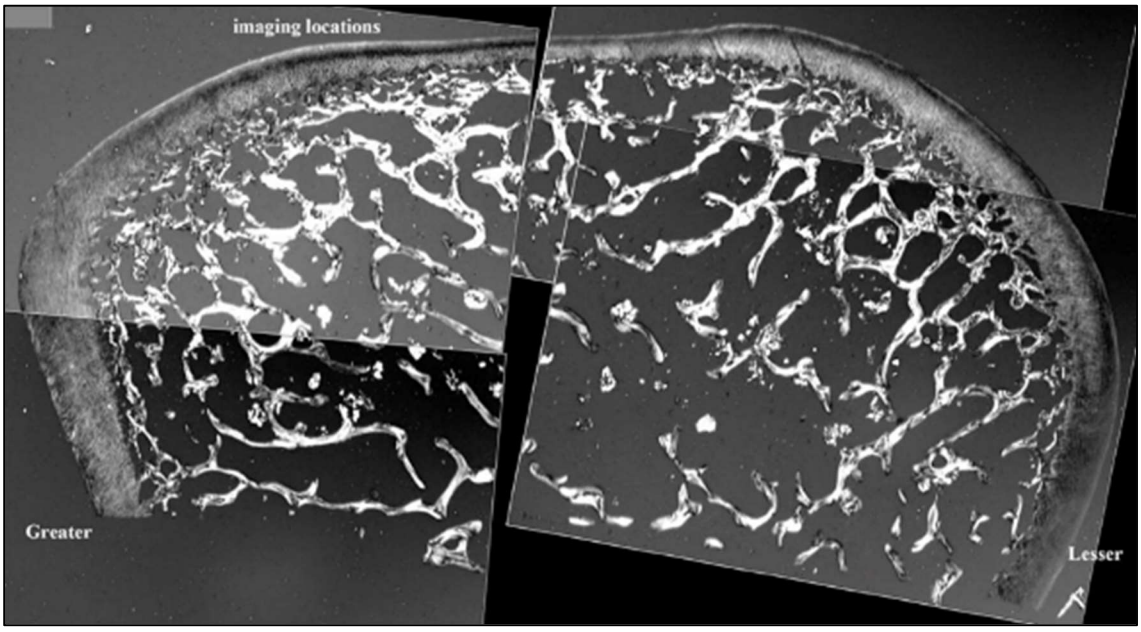

Note. The histological slice of the intact humeral head was imaged in four parts to cover the entire humeral head with a 2.5x objective (4 µm pixel resolution); the four quantitative retardation images were scaled using identical limits (0 – 10 nm); the images were pieced together in photoshop. The humeral head shows a strong curvature, flat in the central area and rounded towards both peripherals. (Some of the curvatures could also be influenced by the histological process after the underlying bone becomes soft in decalcification.) In the retardation images, large and small values indicate that the collagen fibrils are ordered, which could include the information for the fibril diameters and fibril packing density.

Figure 3.7

2D retardation (a) and angle (b) images in PLM, at 1μm pixel resolution of one humeral cartilage specimens

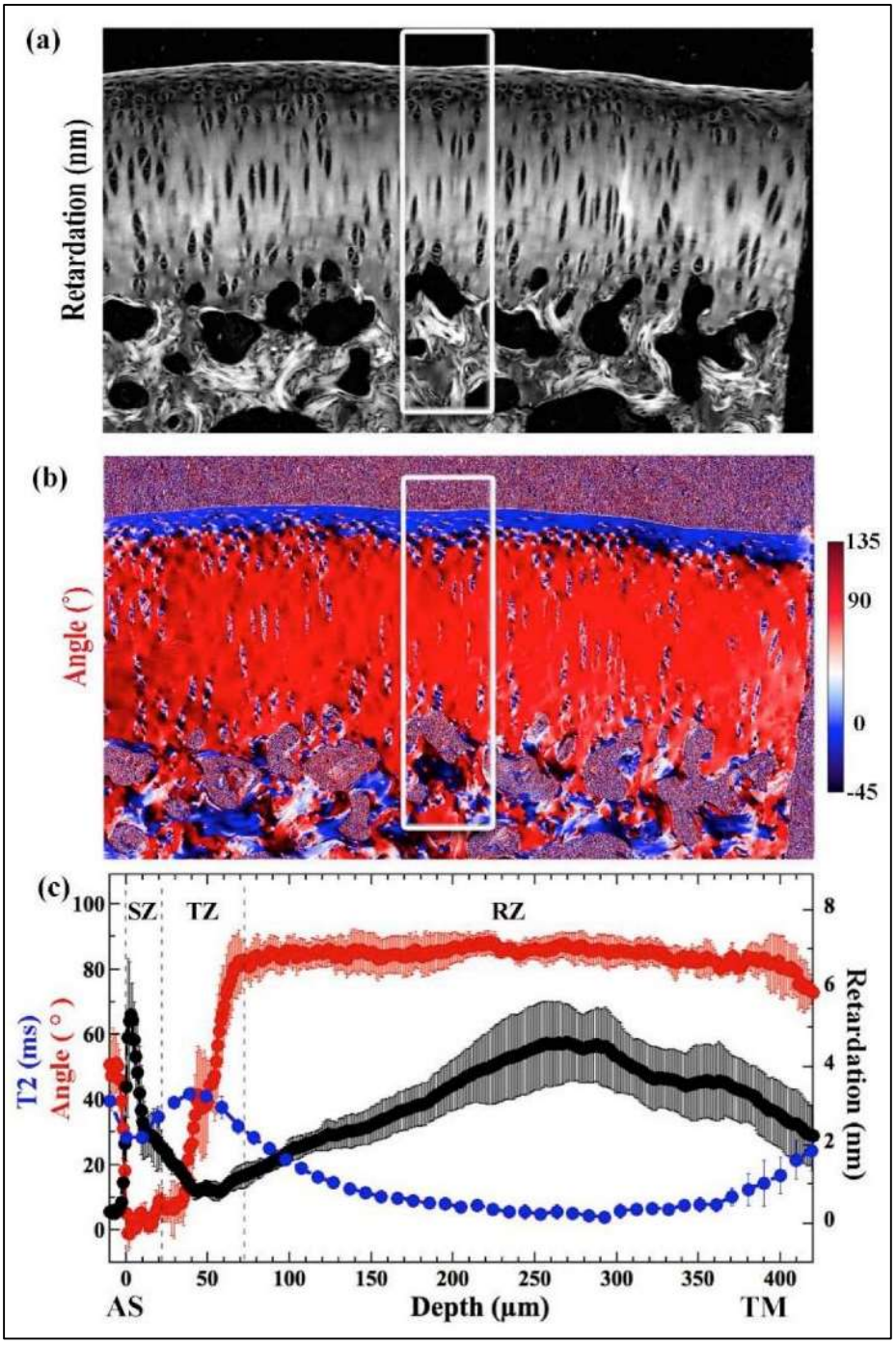

Note. In the angle images, a typical arch structure of the collagen matrix should have a nominal 90˚ orientational difference between the superficial and radial fibers, hence represented by the blue and red colors. The rectangular boxes in (a) and (b) show the location where the depth-dependent profiles were calculated and shown in (c). Also, in (c) is the T2 profile from μMRI of the same specimen. Note that the oval shapes in the retardation image are the locations of the chondrocytes that used to be present in cartilage. Since no protocol was used in histology to preserve the cells, the cellular components were washed out, which yielded black color in the retardation images (i.e., background values). In contrast, the same empty cellular spaces are often filled with random numbers in the angle images, which is due to the imaging algorithm that determines two quantitative numbers at each pixel location). These inaccurate assigned angles and retardation values in the cellular cavities contribute to and exaggerate the size of the error bars in the PLM profiles. The vertical dashed lines mark the locations of the three histological zones. AS and CBI in the tissue depth mark the articular surface and cartilage-bone interface respectively.

CHAPTER FOUR

LOCATION-SPECIFIC STUDY OF YOUNG RABBIT FEMORAL CARTILAGE BY T2 μMRI AND POLARIZED LIGHT MICROSCOPY

4.1 Introduction

In this study, we characterized the structural variations at different anatomical locations of femoral cartilage in young skeletally immature rabbits (12-14 weeks old). Quantitative MRI relaxation data and PLM fibril data revealed collaboratively distinct topographical variations in both cartilage thickness and collagen organization in the juvenile joint. This study aimed to better understand the structural specifics in skeletally immature tissue in the rabbit model, related to its potential in the use of osteoarthritis studies, and the remodeling of the collagen fibril network during growth and maturation at different anatomical locations over the same joint surface. Since any joint has specific 3D shapes/contours and a unique set of biomechanical and biochemical environments, any joint degradation at its early stages must have complex variations over joint surfaces, and knowledge of normal topographical variations will be useful to understand the degradation process dependent upon the location of the initiation event.

4.2 Materials and methods

4.2.1 MRI of intact joint

Four knee joints from 12 to 14 weeks old, healthy rabbits (White New Zealand, male) were obtained from a nearby higher-education institution. The animals were sacrificed for an unrelated approved biomedical study ((PROTO202000161). Ethical approval for the use of spare tissues in our study was waived by the Institutional Animal

Care and Use Committee (IACUC). The animals were frozen immediately at -80 ˚C after necropsy and thawed at 4 ˚C before specimen harvesting. Each intact joint was placed in a glass tube with a cotton swab soaked with physiological saline to avoid dehydration and imaged at room temperature using a Bruker AVANCE III HD NMR spectrometer equipped with a 7 Tesla/89 mm magnet and 25 mm RF resonator (Bruker, Germany).

All four intact knees were imaged in sagittal and coronal views using the standard multi-slice multi-echo sequence, where each imaging experiment had 8-10 slices and each slice had 6-8 intensity images. Each slice had a thickness of 0.8 mm with a gap of 1mm between any two neighboring slices. The imaging echo time (TE) was 8.23 ms, and the repetition time (TR) was 3 s. The FOV was 22×22 mm^2 and the 2D acquisition matrix was 256×128, which was later reconstructed to 256×256, resulting in a pixel size of 86 μm.

4.2.2 μMRI of cartilage-bone specimens

After imaging the intact joints, two knees were opened (Fig 4.1a) to harvest the cartilage-bone specimens from the femoral medial condyles. Each condyle was cut into 3 slices (Fig 4.1e), which were ~1.6-1.8 mm in thickness. Three individual cartilage-bone specimens were harvested from three separate locations on the same (middle) condyle slice (Fig 4.1f), which were named anterior (A), central (C), and posterior (P), respectively. Each cartilage-bone specimen was rectangular, approximately 1.8×2×2.5 mm^3 in size, and still had a full thickness of articular cartilage attached to the underlying bone. All cartilage-bone specimens were equilibrated in saline with 154 mM protease inhibitors. The total number of cartilage-bone specimens for μMRI was six (two for each location).

Each of the cartilage-bone specimens was imaged independently five times using identical imaging parameters, except for the physical orientations of the specimen to the external magnetic field B_0, ranging from 0˚ to 125˚ (where 0˚ is defined as the normal axis of cartilage surface being in parallel with B_0) with the use of a home-built rotating device (Xia, Moody, & Alhadlaq, 2002). A magnetization-prepared 2D spin-echo sequence was used for the quantitative T2 imaging of all cartilage-bone specimens, with TR of 2 s, TE of 6.47 ms, and a slice thickness of 0.8 mm. The location of the slices throughout each series of imaging experiments was identified to be the same during the project. The 2D matrix was 256×128, which was reconstructed into 256×256; the FOV was 2.5×2.5 mm^2, resulting in a pixel size of 9.75 μm for all cartilage specimens (Batool et al., 2020; Xia, 1997). The echo times of the leading contrast segment (TEc) had four increments: 2, 16, 22, and 46 ms, for the central (C) and posterior (P) specimens and 2, 16, 46, and 60 ms for the anterior (A) specimens.

4.2.3 PLM specimens and protocol

All six cartilage-bone specimens after the non-invasive μMRI were processed for histology. In addition, two remaining intact joints were processed for whole-joint histology, where the full-length and width slabs (4-5 mm thick) were cut in transverse planes (across tibiofemoral and patellofemoral regions, as in Fig 4.1b and 4.1.c) and along the middle of the medial condyle (including all 3 μMRI sites, as in Fig 4.1f). All histology specimens were fixated in 10% neutral buffered formalin overnight at room temperature. All fixated specimens were sent to a histology service (Yale Pathology Tissue Services, CT), which cut the specimens at specified locations into 6-μm thin sections using the paraffin embedding method. Three sections from each cartilage-bone

specimen (the μMRI samples) and three sections from each longitudinal and lateral slab were imaged using a digital PLM system (Leica, Germany & Cambridge Research & instruments, MA). Each imaging acquisition in the digital PLM system generated two quantitative images: the optical retardation (in units of nm) and the angular orientation (in units of °). The angle image represents the voxel-averaged orientations of the collagen fibrils, whereas the retardation image represents the voxel-averaged organization of the collagen fibrils in tissue (Xia et al., 2001a).

Each cartilage-bone specimen (A, C, P) had at least three full-thickness histological sections, which were imaged individually at identical orientations under 10x and 40x objectives. This yielded a pixel size of 1 μm and 0.25 μm respectively. The 10x images were used for quantitative retardation and azimuthal profiles and the 40x images were used to observe the territorial matrix surrounding the individual chondrocytes at different depths. Histological sections of the intact femoral condyles were imaged under 2.5x and 5x objectives, which yielded pixel sizes of 4 μm and 2 μm, respectively. These low-resolution optical images were used to study the heterogeneity of collagen fibril organization across the intact femoral condyles in orthogonal directions.

4.2.4 Image and data analysis

Quantitative maps of T2 relaxation were calculated by a single exponential fitting of the data on a pixel-by-pixel basis for all specimens. Each cartilage-bone specimen was imaged in μMRI five times at five different orientations to B_0, which resulted in 20 independent proton images and 5 calculated T2 maps for each specimen. On each quantitative 2D T2 image, one rectangular region of interest (ROI) with 15 parallel neighboring columns was selected manually and averaged into one 1D depth-dependent

T2 profile, which enabled the observation of the depth-dependent T2 anisotropy in the tissue and the comparison among profiles from different imaging experiments. Since the column-averaging occurred perpendicular to the tissue depth, the pixel resolution in the T2 profiles was still 9.75 μm along the tissue depth. The width and location of ROI were the same for all independent imaging experiments of each sample, using the image analysis software ImageJ. All 2D images and 1D profiles, where each came from one independent imaging experiment, used identical scaling and settings without any additional adjustment.

On each quantitative PLM image of cartilage specimens obtained at 10x objective, 146 parallel neighboring columns, which would have approximately the same width as the ROI thickness in μMRI, were averaged to produce one pair of 1D quantitative retardation and angle profiles across all tissue zones. The 40x images enabled the visualization of the shape and orientations of chondrocytes concerning the surrounding territorial and interterritorial matrix at different depths (histological zones) among all histological sections from three locations. The post-acquisition analysis used the public-domain software ImageJ (NIH) and commercial software KaleidaGraph (v4, Reading, PA).

4.3 Results

4.3.1 MRI of intact knee joint

Before opening the knee joints, the intact knees were imaged by μMRI at the pixel resolution of 86 μm. Fig 4.2 shows the sagittal and coronal views of T2-weighted intensity images respectively, together with their respective quantitative T2 images. The epiphyseal cartilage (growth plate) appears brighter and homogenous in intensity; in contrast, signal

variations can be seen over the thickness of articular cartilage, especially in the femur, even at the low 86 μm resolution. The appearance of articular cartilage in T2-weighted MRI images was highly sensitive to its orientation to the external magnetic field B_0 (vertically up). Because of its curved articular surface, the femoral condyle provides a convenient model to study the orientation effect of cartilage T2 relaxation to B_0 (i.e., the magic angle effect), if the quality of cartilage is the same at every location. If T2-sensitive structural variations exist as expected in the juvenile joint during development, the interpretation of imaging results needs additional considerations. In our imaging results, among the three topographical locations on the central medial femur, the central location (C) was about at the magic angle (~ 54.74˚) to B_0 (sagittal view), where the influence of the dipolar interaction to the spin-spin relaxation was minimized; consequently, the cartilage in the central region appeared thicker than at the two other locations, anterior (A) and posterior (P). Away from the magic angle location, the femoral cartilage appeared bilaminar with a high-intensity surface layer and a low-intensity deep layer. Due to the pixel size, signal variations for thinner regions (A and P) can be influenced by volume averaging.

4.3.2 PLM images of intact femur joint at 4 μm resolution

Fig 4.3 is the quantitative retardation images of the whole joint by PLM, at the three cross-sectional surfaces shown previously in Fig 4.1f, Fig 4.1b, and Fig 4.1c. (Multiple retardation images were acquired individually in PLM and pieced together without any additional intensity adjustment.) Fig 4.3a is the retardation image of a longitudinal section of a femoral medial condyle at 4 μm pixel resolution (from the tissue block as in Fig 4.1f), which showed that femoral cartilage was thinner at peripheries and thicker in the central region. Three topographical variations were determined from this

image. First, the central cartilage was about 600 μm in thickness, twice the thickness when compared with the anterior and posterior cartilage (~ 300 μm). This PLM observation is consistent with the MRI results of knee joints in Fig 4.2. Second, the values of retardation were the lowest at the anterior site and highest at the central site, where most of the deep central cartilage had high retardation (i.e., high coherence in fibril organization) and most of the anterior site had very low retardation (i.e., low coherence in fibril organization). Finally, the lowest values of retardation at any topographical location occurred consistently at approximately 35 μm to 40 μm below the articular surface, regardless of the total thickness of the cartilage at this location.

Fig 4.3b and 4.3c are the retardation images of two cross-sections taken transversely or orthogonally from the anterior (patellofemoral) locations of the femur (which opposes the patellar cartilage) and the central (tibiofemoral) location of the femur (which opposes the tibial cartilage) as shown in Fig 4.3a (as well as shown previously in Fig 4.1b and 4.1c). Two observations can be made for these cross-sections. First, there is little difference in cartilage thickness across most of these transverse/orthogonal sections (except at the peripheral edges). Second, the femoral cartilage (Fig 4.3b) from the central cross-section seemed to have more variations in the structural patterns across the tissue depth. For example, this occurred between the cartilage at the trochlear ridges (TR) to the cartilage in the trochlear groove (TG). For these reasons, one ROI was selected from the central location of the medial femoral head (shown in Fig 4.3c), and two ROIs were selected from the anterior cartilage opposing the patellar cartilage (shown in Fig 4.3b).

4.3.3 MRI of site-specific T2 anisotropy results

Fig 4.4 shows the T2 anisotropy results at the higher spatial resolution of 9.75 μm in μMRI, from three specimens acquired from the anterior, central, and posterior regions of the femoral medial condyle, shown previously in Fig 4.1f and Fig 4.3a. (Note that each specimen was imaged five times between the orientations of 0˚ and 120˚. Since these images appeared similar visually, only two images for each location were shown in the figure. The most insightful information on T2 anisotropy among each set of five images can be obtained from the depth-dependent profiles in Fig 4.4, which contain all orientations at all locations.) The images and anisotropy profiles of cartilage from the central (C) location have familiar features that assemble the well-known T2 anisotropy under the influence of the dipolar interaction (Xia, 1998, 2000b). Based on the data at 55°, the cartilage thickness was ~500 μm at the central location. When the specimen was oriented at 0˚, where the dipolar interaction is the strongest, most of the deep tissue had little signal in the spin-echo-based imaging sequences. This caused the truncation of the T2 (0˚) profile to a depth of ~ 200 μm, beyond which the signal became too low to be reliably used to calculate T2 (the echo time in the imaging sequence is 6.47 ms). Compared to the central cartilage, the posterior cartilage was about 50% thinner, at ~ 350 μm. The T2 (0°) profile followed approximately the bell-shaped curve as seen in the central cartilage, but the peak was not as sharp and occurred deep in the percentage thickness. The rest of the anisotropy profiles did not follow strictly the T2 anisotropy as observed in the central cartilage. This implies that the overall orientational structure of the collagen fibers in the posterior cartilage might be slightly different from the central cartilage. But it largely followed the usual three-zone structure as seen in mature cartilage. The anterior cartilage had the most curvature and its T2 anisotropy profiles had the most complicated variations. Two ROIs

(A1, A2) were selected for the anterior specimen, where A1 is located at the anatomical location of the trochlear ridge (TR) and A2 is in the proximity of the trochlear groove (TG). The T2 anisotropy profiles from the A1 location lost all recognizable features as shown in the central cartilage, which implies its collagen matrix did not have any of the usual three-zone structure.

4.3.4 Quantitative PLM images of cartilage-bone specimens

Fig 4.5 shows the quantitative PLM results at 1 μm pixel resolution from the cartilage specimens at three topographical locations on the medial femur, whose μMRI data was presented in Fig 4.4. In the quantitative retardation images, the small black 'holes' inside the articular cartilage are the locations where the cells and cell clusters used to reside (the histology procedure did not preserve the cellular details). In these angle images, the blue and red colors indicated a 90˚ difference between the fibril orientations; the same 90˚ difference also existed between the black and white colors, which had a 45˚ shift in the orientation to the blue and red combination.

Several features can be identified among the specimens obtained from three different anatomical locations of the joint. First, the PLM images and profiles for cartilage from the central location showed that the tissue had the arched three-zone fibril architecture, where the surface fibers and the radial fibers had a 90˚ difference in their angular orientations (represented by the blue and red colors respectively in the image). This observation agrees with the quantitative μMRI data discussed previously in Fig 4.4, and this agreement between the μMRI and PLM data is also consistent with the observations from many mature cartilage tissues from larger animals such as canines (Xia et al., 2001a). With this understanding, one can easily see that the collagen fibers in the

posterior cartilage also have the arched three-zone architecture, except that the tissue is thinner.

Second, as we have observed in the μMRI T2 anisotropy data (Fig 4.4c), cartilage from the anterior location has a fibril architecture that is far from the arched three-zone structure. This μMRI observation can be confirmed by the high-resolution PLM data in Fig 4.5. Comparing the 2D images between the anterior location and the central location, it is easy to recognize the continued variation of fibril structure even within the short length of the anterior cartilage block (~ 1.5 mm).From the orientations of the black oval-shaped cell voids in the retardation images, which follow the local orientations of the collagen fibers in the territorial matrix of the tissue, one recognizes the transition from the right end (towards the G side) of this specimen, which still has some similarity to the arched three-zone structure, and to the left end (towards TR side) of this specimen, where most of the deep cells become parallel with the articular surface, representing the parallel architecture of collagen fibers at this location. Comparing the quantitative 1D retardation profiles of all locations (Fig 4.5c), it is evident that the overall retardation values are lower for anterior than central and posterior specimens (weak mutual organization).

Third, among the three locations, the central cartilage was the thickest (550 μm), about 50% thicker than cartilage at both anterior and posterior locations (250 μm-300 μm). Although different in their total thickness, both central and posterior cartilage had approximately the same thickness in their superficial zones (10-15 μm), and an identical tissue retardance minimum (~ 30-35 μm below the articular surface, marked by the arrow in Fig 4.5.c).

4.3.5 Comparison between μMRI and PLM

Fig 4.6 compares the T2 (0˚) profiles from μMRI and the retardation profiles from PLM, for the four topographical locations on the femoral condyle. In these quantitative profiles, the location of the minimum retardation indicates the location of the least ordered collagen fibrils in the tissue. By comparison, the location of the maximum T2 relaxation at 0˚ indicates the location of the least-ordered water molecules in the tissue. Among the four locations, only the central cartilage (Fig 4.6c) has a matched correlation between the T2 peak and the retardation minimum, which is consistent with the previous observations in mature cartilage (Xia, Moody, Alhadlaq, et al., 2002). At the A2 location (Fig 4.6b) and in posterior cartilage (Fig 4.6d), the T2 peaks areless well-defined and the peak correlation between μMRI and PLM is lacking. Cartilage at the A1 location (Fig 4.6a) does not have any recognizable feature that can be used to interpret the arched three-zone fibril structure.

4.3.6 Territorial matrix

Fig 4.7 shows the high-resolution quantitative angle and retardation images (40x objective, 0.25 μm/pixel) of the cellular clusters at different depths, from the same specimens used before in the 10x imaging (Fig 4.5). Morphologically, one can use quantitative retardation images to view the cellular structure, from which one can easily determine the zonal orientation of the cells and cellular clusters. In the SZ of all three sample locations, all cells had a spindle shape and were oriented in parallel with the articular surface. In addition, the territorial and interterritorial fibers ran parallel to the articular surface (i.e., having the blue color in the angle images). In the central and posterior cartilage, the cellular clusters in TZ were more circular, which implied the lack of a dominant orientation. Furthermore, the cellular clusters in RZ are all oriented

vertically – perpendicular to the articular surface, which can also be seen from its red color in the angle images. In contrast to the central and posterior cartilage, the cellular structures in RZ at the anterior location oriented approximately with the articular surface, which gives the anterior cartilage its lack of arched zonal structure. A higher cellular density can also be noted in the anterior cartilage – in particular, the anterior clusters were fatter than the central and posterior clusters, which implies larger aspect ratios of the oval shapes (aspect ratio = width/length).

Quantitatively, higher retardation values can be found in the proximity of cells and cellular clusters, which indicates the presence of a cocoon-shaped fibril structure surrounding each cell or each group of cells. The same cocoon-shaped fibril structure was also seen from the quantitative angle images when they were enlarged further, in which the angle values change in a cyclic manner, i.e., the same color appears on the opposite side of the same cell or cellular cluster. Since a collagen fiber has neither head nor tail, the same angle value appears on the opposite side of any circular shape, which should have two 90˚ orientational differences, between the blue and red colors, and between the white and black colors. For the central and posterior cartilage, the background colors in the angle images, i.e., the orientations of the territorial matrix in the tissue, had the expected 90˚ transition between the surface and deep cartilage, indicating an arched three-zone structure. In contrast, the anterior cartilage (A1) had the same blueish color for all regions of the tissue, indicating an absence of a three-zone structure.

4.4 Discussion

To the best of our knowledge, this is the first quantitative study of the topographical features of the femoral cartilage in a rabbit model by μMRI and PLM at microscopic resolutions. Compared with the use of larger animals, rabbits are small, inexpensive, and have more societal acceptance. Since rabbit cartilage is thin, any depth-dependent examination requires high resolution in imaging. In recent years, the use of rabbit models in biomedical research has been gradually increasing (Batool et al., 2020; Esteves et al., 2018; Frenkel et al., 2005; Julkunen et al., 2009; Sah et al., 1997; Wakitani et al., 1998). Still many features of the rabbit tissues, even in healthy control animals, have not been well characterized, which complicates the understanding of degenerative characteristics in tissue.

4.4.1 Topographical structural variations in juvenile joints

A better understanding of the developmental changes from juvenile tissue to mature tissue is critically important since younger populations can develop osteoarthritis several years after traumatic injuries. Studies of the juvenile canine humeral head and ovine distal metacarpus (vanTurnhout et al., 2010; Xia et al., 2003) have revealed several site-specific collagen structures ranging from the arched three-zone structure to complex multi-zone architecture, which can be seen on the same joint surface. Such site-specific collagen structures are absent in mature animals (Xia, Moody, Alhadlaq, et al., 2002). These experimental observations support the notions that there are specific imaging features that are unique in juvenile joints, and that not all locations on the same juvenile joint develop into the three-zone structure simultaneously. A probable explanation for these developmental differences at different locations on the same joint surface could be

either variable growth rates, a pattern of the bone epiphysis, or exposure to different mechanical loading conditions at different anatomical sites of the same joint (Brama et al., 2000b; Heinemeier et al., 2016; Hudelmaier et al., 2001; Julkunen et al., 2010; van Turnhout et al., 2010; Peters et al., 2018; Thonar & Sweet, 1981; Wong et al., 2009).

This study showed that for 3-month-old juvenile rabbits, the cartilage at the central and posterior locations along the femoral medial condyles had already developed into the classic three-zone architecture, which is commonly seen in mature joints. In contrast, the cartilage at the anterior location, the trochlear ridge (TR) of the patellofemoral region of the same joint, had no zonal architecture. This topographical difference could have two causes, developmental and mechanical. The developmental cause is associated with the maturity of the cartilage, where distinct differences between the juvenile and mature cartilage in large animals have been noticed (Xia et al., 2003; Xia, Moody, Alhadlaq, et al., 2002). The mechanical cause is associated with the differences in the force patterns between the anterior location and the central and posterior locations. While the central and posterior cartilage is subject to large compressive loading, the anterior cartilage is subject to constant tangential motion with the patellar cartilage. Hence, the collagen fibers may adapt to the local mechanical environment.

Since MRI T2 anisotropy is extremely sensitive to the dynamic environment of water molecules in biological tissue, it is expected that the fibril architecture and structural variations of the collagen network can be detected non-invasively and non-destructively by MRI, if a sufficient resolution can be achieved (as in μMRI). At the same time, this study also employed quantitative PLM protocols at the higher optical

resolution, which are uniquely sensitive to the mutual organization and overall orientation of the collagen matrix based on different physical principles. It has been shown previously that the retardance minimum below the articular surface is closely associated with the geometric center of the transitional zone, which is represented by a maximum in quantitative T2 anisotropy of adult animals. The correlation between the two quantitative protocols can define the zonal architectures of the collagen network, from the classic three-zone architecture to more complicated variations in juvenile tissues.

4.4.2. Intervention at an early stage

Understanding the differences between the juvenile and mature cartilage associated with the developmental stages and mechanical environments in individual animals (and humans) can contribute to a better intervention of the cartilage degradation process at an early stage. The collagen network in cartilage is responsible for the structural stability of the tissue, which remodels continuously during growth and adolescence periods. After skeletal maturation, cartilage maintains a stable structure for the rest of the lifespan with only minor adaptations (Heinemeier et al., 2016). Studying the site and age-dependent mechanisms in tissue remodeling provides an opportunity to intervene/repair cartilage optimally at different ages when the damage and degradation occur, which could prevent or postpone advanced stages of osteoarthritis. For example, sports-related injuries, common in young adults, can develop into osteoarthritis within a brief time after the injury. Failure in cartilage repair could happen if the repair tissue does not fit the specific age and topographical dependent features of the damage location.

The development of arcade-like structures with age is an important and interesting phenomenon, the understanding of which would be beneficial to the design of superior

materials and procedures as it would be more stable and better able to effectively handle the loading environment. Therapeutic improvements could potentially be implemented by identifying and investigating the localized physiological and mechanical factors involved at different sites on the same joint. For example, osteochondral allograft transplantations have been used to treat focal lesions in young and active patients. Considering the topographical variation in the fibril architecture can be helpful in dealing with the site morbidity and improve the integration, if the repair grafts can be designed to better match with neighboring/donor cartilage structurally.(Reddy et al., 2007).

4.4.3. Experimental notes

Structural changes in collagen fibril orientation are closely linked to compositional changes (PG and collagen content) in connective tissue. Due to technical limitations, we did not perform any histochemical analysis to determine any compositional difference in the cartilage at different sites. In addition, since the development of the collagen network is a gradual process, we recognize the potential need for more time points (i.e., different-aged animals) to fully understand the developmental variations in the tissue architecture. The number of μMRI sampling locations was three, which were 4-6 mm apart from each other along the same small joint. It should also be noted that any topographical variations are highly dependent on the plane/location of histological cutting and the type of joint. Finally, any sample with curved surfaces (e.g., the anterior specimen in Fig 4) cannot be set in any single experiment with the entire surface at a particular orientation. This would also be true for any intact joint in human MRI. Any deviation from the nominal orientation would affect the T2 anisotropy, mainly via the geometric factor in the dipolar spin Hamiltonian (Xia,

1998). Note that in physics, anisotropy is a descriptive term, which refers to the characteristic of a measurement that exhibits different values when measured along with different directions. In MRI, the direction in the sample space is defined by the polarizing magnetic field B_0. There are various methods to analyze the characteristic of T2 anisotropy. The first and original method analyzes the depth-dependent profiles directly (Xia, 1998) (as Fig 4c of this study). One can also combine these depth-dependent profiles into 2D or pseudo-3D anisotropy maps, either without image interpolation (Xia, Moody, & Alhadlaq, 2002) or with image interpolation (Hänninen et al., 2021). Furthermore, one can calculate the percentage differences in these depth-dependent profiles (Hänninen et al., 2021). In addition, if T2 anisotropy has been measured at many different orientations in the 0˚-360˚ angular space, one can calculate the relative contents of two orthogonal fibril directions on a pixel-by-pixel basis (Xia, Moody, & Alhadlaq, 2002). In this study, our goal is to characterize the structural variations at different anatomical locations of femoral cartilage in young rabbits. The direct comparisons among the μMRI and PLM profiles (Fig 6) are sufficient to clearly show the nature of these location-specific anisotropies quantitatively.

Figure 4.1

The right knee of a 3-month-old, rabbit, and its histological sections.

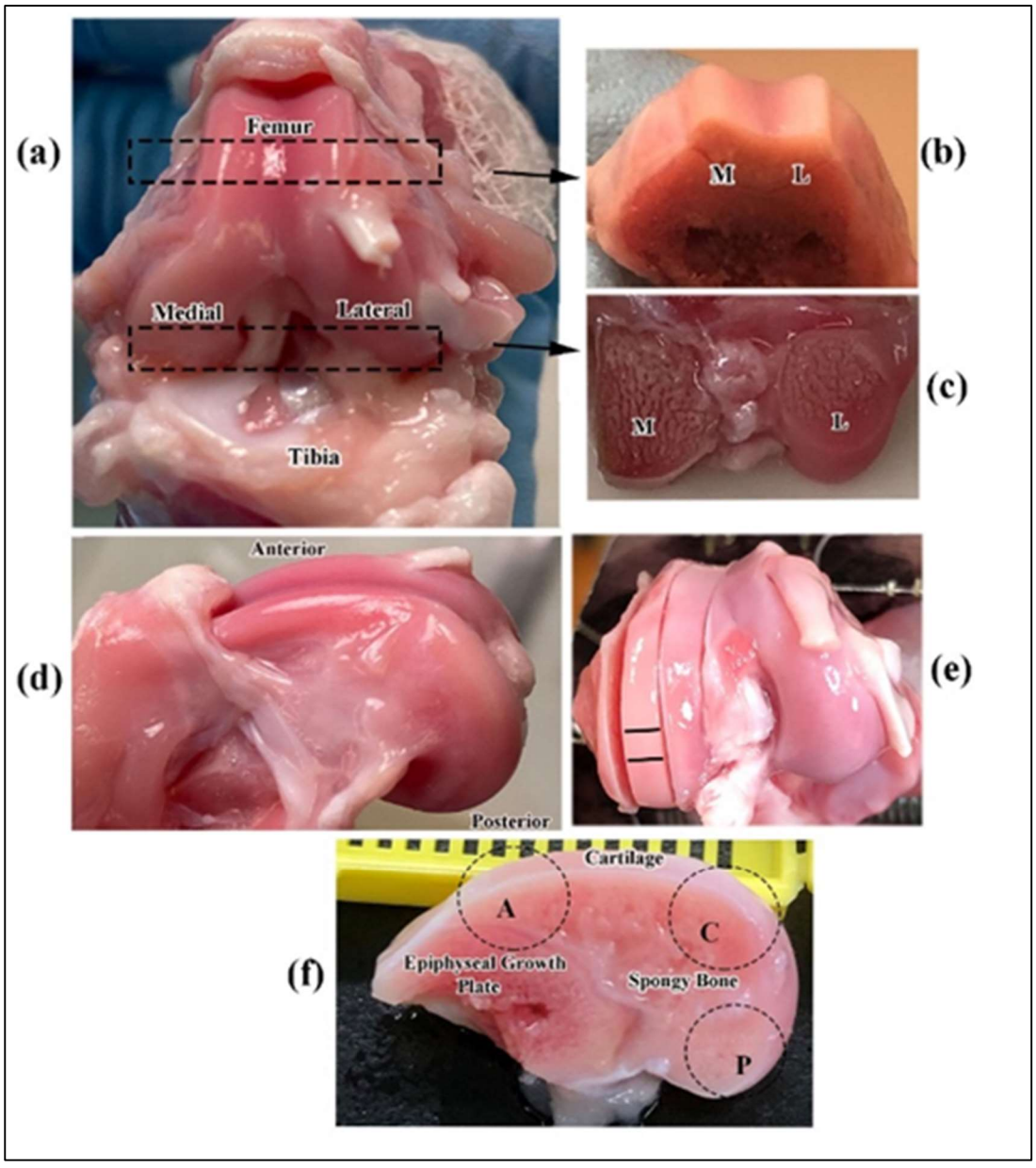

Note. (a) Both medial and lateral condyles of a femur are shown. (b) The cross-sectional slice at the patellofemoral location of the femur covers both medial and lateral condyles before its split. (c) The cross-sectional slice at the tibiofemoral location of the femur covers both condyles. (d) Side view of an un-sectioned femur medial condyle. (e) The medial condyle is sectioned into three ~1.6-1.8 mm thick cartilage-bone slices longitudinally. The central slice, which runs up to the unsplit part of the femur, is further cut into small rectangular cartilage-bone specimens (~ 1.8×2×2.5 mm^3) for high-resolution μMRI and PLM. Two thin lines mark the location of the central specimen on the central slice. (f) Side view of a central slice of medial condyle with three designated locations (A, C, and P) for μMRI specimens.

Figure 4.2

Coronal and sagittal T2-weighted intensity images and corresponding T2 maps

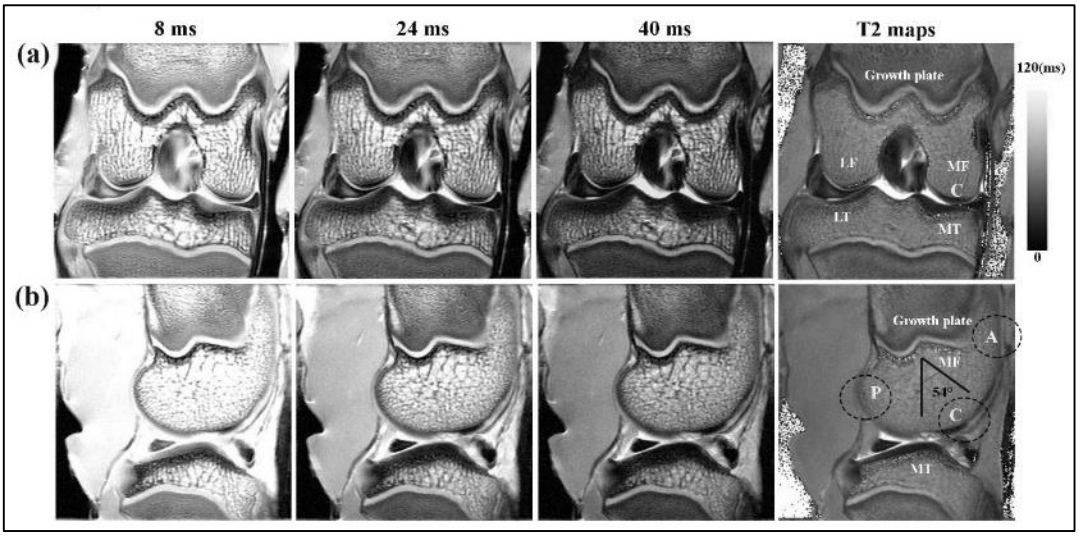

Note. Each set of T2-weighted intensity images had 10 individual images, each at a different echo time. These intensity images were used to calculate one quantitative T2 image. Three designated locations, labeled as central (C), posterior (P), and anterior (A) on the medial condyle, were selected for μMRI T2 experiments. All images are displayed using the same up/low limits on a greyscale. (MT: medial tibia; MF: medial femur).

Figure 4.3

The quantitative retardation images.

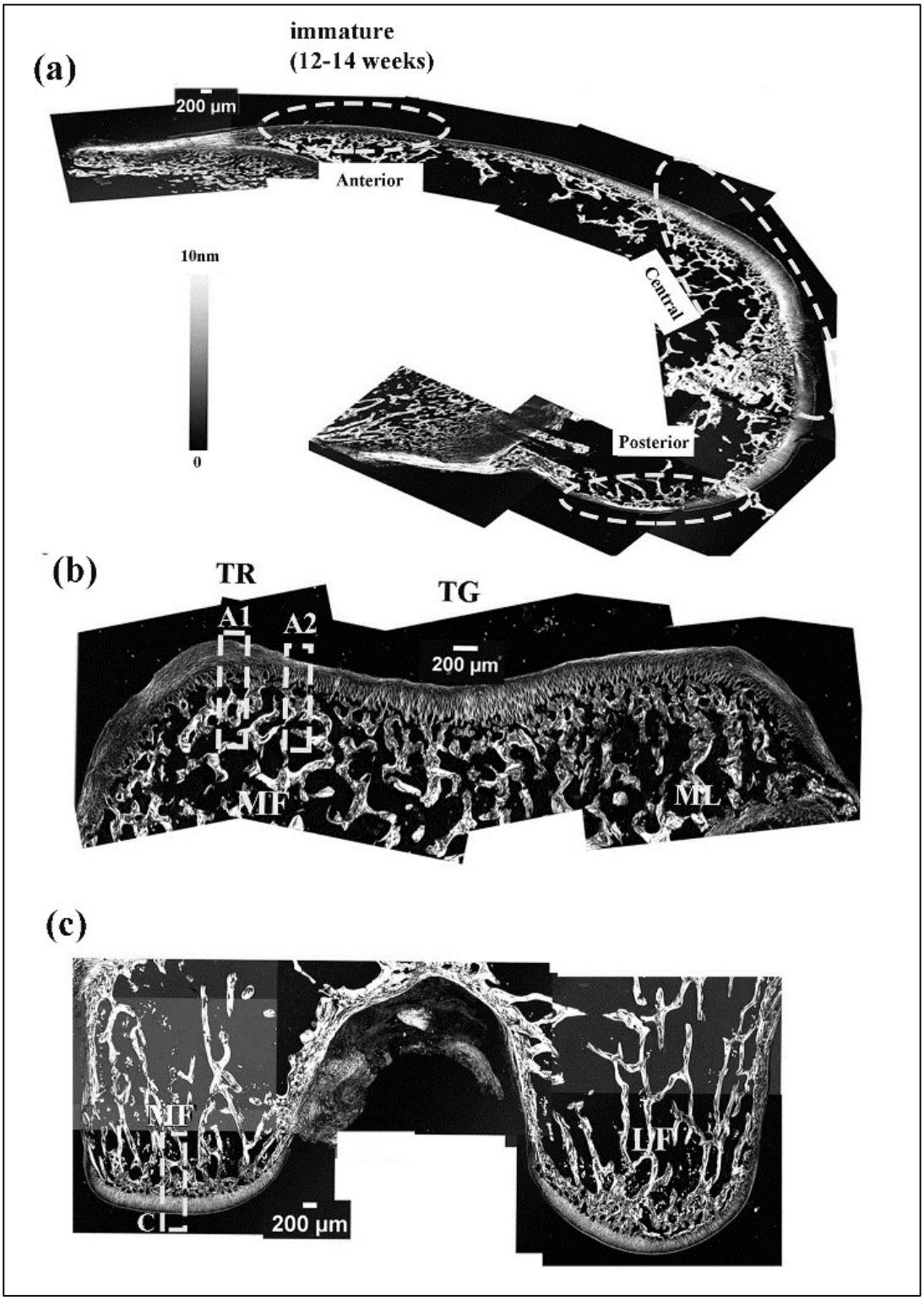

Note. (a) The longitudinal slice from a femoral medial condyle (4 μm/pixel) displayed with identical intensity limits (0–10 nm). Three white elliptical shapes show the locations where the small specimens were harvested for μMRI. (b) The retardation images (2 μm/pixel) from a tissue slice that was harvested transversely to the slice in (a), approximately at the anterior location. (c) The retardation images (4 μm/pixel) from a tissue slice that harvested transversely to the slice in (a), approximately at the central location where the femur has two distinct medial and lateral condyles. The transverse planes on these slices are approximately at the same imaging planes as in μMRI. Three dashed rectangular boxes (A1, A2, and C) in b and c are the ROIs selected on the cartilage-bone specimens for quantitative imaging. (MF: medial femoral; ML: medial-lateral; TR: trochlear ridge; TG: trochlear groove).

Figure 4.4

2D μMRI intensity images (left) and corresponding T2 images (right) of cartilage-bone specimens (A, C, P) at 9.75 μm/pixel at (a) 0˚ and (b) 55˚ and (c) 1D profiles at 5 different orientations.

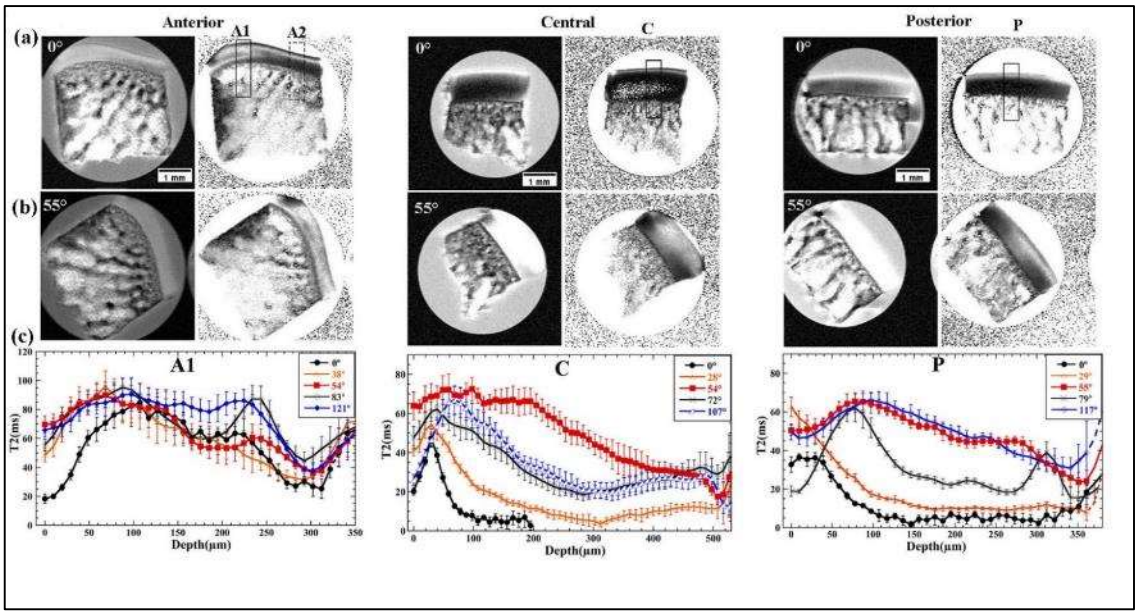

Note. Each of the three samples was imaged under identical parameters except its orientations in B_0. Since the anterior specimen had the most curved surface, two ROIs (A1, A2) were selected, where the A1 location is closer to the trochlear ridge (TR) and A2 is towards the trochlear groove (TG). (c) Quantitative T2 profiles from cartilage in ROIs (A1, C, and P), where the standard deviations of the averaged T2 data over the width of the ROI are represented by the vertical error bars.

Figure 4.5

2D quantitative PLM images and 1D quantitative profiles (retardation and angle) at 1-µm pixel resolution

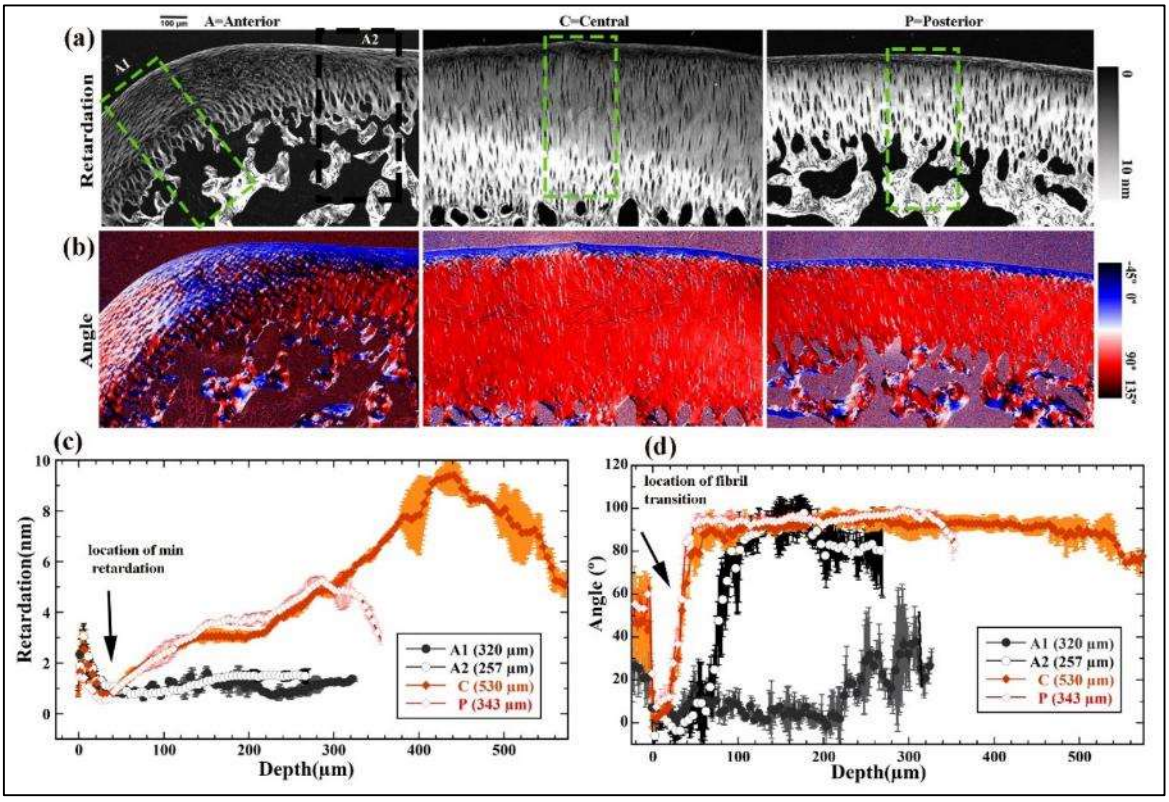

Note. The rectangular boxes in (a) show the locations where the depth-dependent profiles for both retardation and angle were calculated and shown as the profiles in (c) and (d). The quantitative profiles for each location are the mean values (retardation and angle) obtained by averaging three histological sections from each specimen. The vertical error bars are the standard deviations in the averaging. The profiles are plotted for every 5th data point, but the standard deviations are shown for all data points. In the angle images, the blue and red colors defined a 90˚ orientational difference in collagen fibers. The white color represents 45˚ in the angle, which can be seen in large regions of the deep tissue in A1 (trochlear ridge). The thickness of the cartilage for each location is listed next to the figure legends in a black rectangular box.

Figure 4.6

Comparison between the quantitative T2 profiles at 0˚ and the quantitative retardation profiles, at four different locations in femoral cartilage

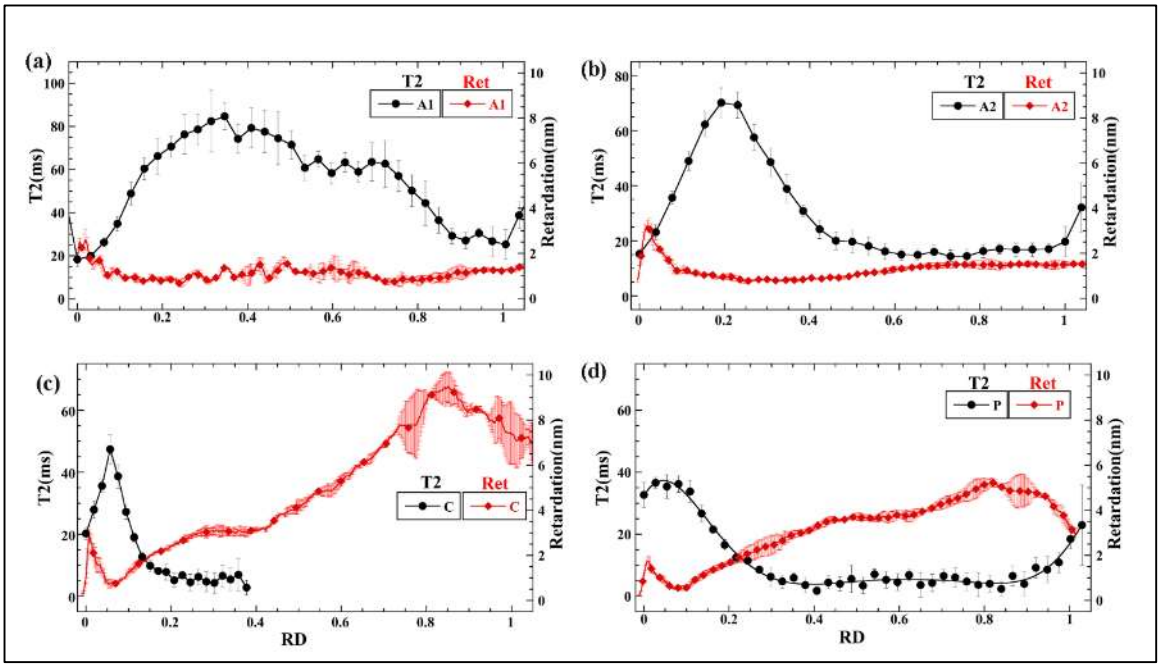

Note. 0 in the relative depth marks the articular surface; 1 in the relative depth marks the cartilage-bone interface (CBI).

Figure 4.7

Quantitative PLM images of the three locations of tissue at 0.25 µm pixel resolution at different histological zones.

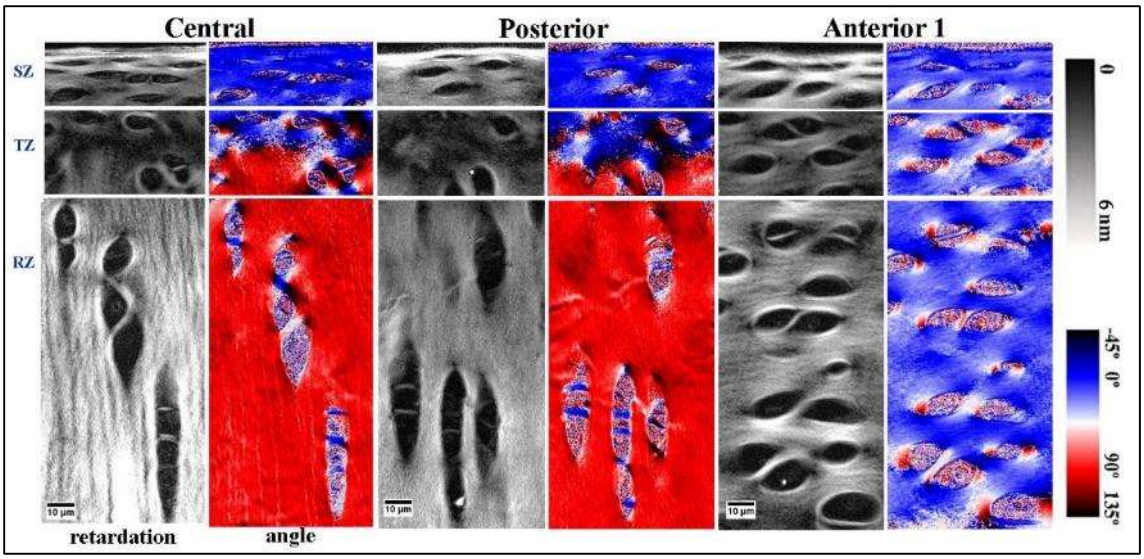

Note. (a) SZ (superficial zone) images of all three locations at 5% of their relative thickness, (b) TZ (transitional zone) images of all three locations at 10% of their relative thickness, and (c) (RZ) (radial zone) images at 40% of their relative thickness.

CHAPTER FIVE

DEPTH-DEPENDENT STRAIN CALCULATIONS FOR ANISOTROPIC FIBRIL STRUCTURES IN ARTICULAR CARTILAGE

5.1 Introduction

The mechanisms giving cartilage its mechanical resilience involve complex compositional and structural variations across the tissue thickness (depth). The major constituents of its ECM are interstitial fluid (water and ions such as Na^+, Cl^-, etc.), and macromolecules such as proteoglycans (PGs) and collagens (Sophia Fox et al., 2009). PGs in cartilage are considered unstructured; in contrast, collagen in mature healthy cartilage forms a network with a depth-dependent tri-zonal structure (Fig 5.1b, left). In addition to the depth-dependent structure of the collagen network, the distributions of molecular components (water, proteoglycan, and collagen) are also not homogenous, and all vary with depth from the articular surface towards the cartilage-bone interface (Mittelstaedt & Xia, 2015; Rieppo et al., 2009; Xia, Zheng, et al., 2008). The depth-dependent variations of the molecular components, in conjunction with the macro and microstructural variations, may control its unique depth-dependent and direction-dependent mechanical deformation response to external loading (Chahine et al., 2004; Chen et al., 2001; Korhonen et al., 2008).

In this study, we used a simple 1D mixture model to study the mechanical deformation response of articular cartilage under 1D axial compression (confined, equilibrium). The model included the structural inhomogeneity of collagen fibers and inhomogeneous distribution of FCD to calculate intra-tissue strains and displacements in

the tissue. This model highlighted the role of collagen fibril mechanics in conjunction with the osmotic swelling pressure of articular cartilage. The 1D model was computational and solved in MATLAB using finite difference methods (Provided in Appendix B). The fibril stiffness was introduced as an anisotropic modulus that varies with fibril orientation through depth. We assumed that collagen fibers were stiffer to stretch parallel to their length (in the RZ) than perpendicular to them (in the SZ). The intrinsic structural inhomogeneity of collagen fibers and inhomogeneous distribution of FCD caused an anisotropic pre-strain in the tissue and increased the tissue resistance against axial loading, specifically in the radial zone. The simulation results (intra-tissue strains and displacements) were applied to different scenarios (mature, immature, healthy, and degraded cartilage) and qualitatively explain many experimental findings. In particular, we examined the relative importance of collagen fibril intrinsic stiffness towards osmotic swelling contributing to the response of cartilage to compression. We hypothesized that the mechanical compressive properties of cartilage were not only dependent upon FCD but also the structured pre-strained collagen fibril network can counterbalance the mechanical compression. The knowledge of the structure and mechanical properties of ECM surrounding the cells is vital not only for understanding but also designing novel engineering scaffolds and tissues that possess normal mechanical functionality.

5.2 Materials and methods

The fundamental assumptions used in this study are described in Fig 5.1a and 5.1b. Cartilage is assumed to be compressible and permeable (water flows in and out). Initially, the unstretched and unloaded tissue (stress $\tau = 0$) has cross-sectional area A,

length L, and FCD concentration C_c (Fig. 5.1a, left). We model the collagen as a series of linear springs with intrinsic stiffness denoted by a mechanical modulus (μ). Due to osmotic swelling pressure caused by FCD, the tissue swells causing a pre-strain ε_{pre} to the collagen fibers and the effective concentration of FCD drops from its unstrained value C_c (assuming the number of molecules remains the same but the volume changes) as tissue is diluted by additional water, giving a strain-dependent concentration.

$$C = \frac{C_c}{(1 + \varepsilon_{pre})} \tag{5.1}$$

During the pre-strain condition of the collagen fibers (without any load applied), let u_{pre} be the distance it displaces in the radial direction, so strain $= \varepsilon_{pre} = \frac{u_{pre}}{L}$ (Fig 5.1a, middle). When tissue is loaded under uniaxial compression ($\tau \neq 0$), let u be the distance it displaces from the initial unloaded state. The resultant strain will be $\varepsilon = \frac{u}{L}$ (Fig 5.1a, right). The observed strain, e, is the net difference between displacements (u_{pre} and u) over the pre-compression length (L+ u_{pre}). Tissue with length $L = 1$ mm under uniaxial load (confined compression) is used to model intra-tissue strains and displacements at equilibrium, when the osmotic swelling stress in cartilage is balanced by the elastic stress exerted by a pre-stressed collagen network (Basser et al., 1998). In that case, the total stress (τ) in the tissue can be represented as the osmotic stress (τ_{FCD}) minus the elastic stress of the collagen network (τ_{CN})(Basser et al., 1998),

$$\tau = \tau_{FCD} - \tau_{CN} \tag{5.2}$$

$$\tau = CkT - \mu\varepsilon_{pre} \tag{5.3}$$

For simplicity, a 1D analysis of cartilage occurs in confined compression. The total normal stress (perpendicular to the articular surface) can be modeled as Eq. (5.1), where, $\tau_{FCD} = CkT$ is an osmotic term that depends on the concentration of FCD (C), the Boltzmann constant k, and the absolute temperature T, and $\tau_{CN} = \mu\varepsilon_{pre}$ is the linear elastic stress exerted by the collagen fibers.

When pre-stressed tissue is under zero external stress ($\tau = 0$), Eq. (5.3) can be written as

$$\frac{C_c kT}{\mu} = \varepsilon_{pre}(1 + \varepsilon_{pre}) \tag{5.4}$$

Solving Eq. (5.4) quadratically gives the pre-strain as

$$\varepsilon_{pre} = \frac{-1 + \sqrt{1 + \frac{4C_c kT}{\mu}}}{2} \tag{5.5}$$

When tissue is stressed under uniaxial compression ($\tau \neq 0$), the observed strain, e, is

$$e = \frac{u_{pre} - u}{(L + u_{pre})}, \tag{5.6}$$

$$e = \frac{\varepsilon_{pre} - \varepsilon}{(1 + \varepsilon_{pre})}. \tag{5.7}$$

From Eq. (5.2), total stress can be written as

$$\tau = \frac{C_c}{(1 + \varepsilon)} kT - \mu\varepsilon \tag{5.8}$$

Rearranging Eq. (5.8) and using Eq. (5.4) gives

$$\frac{\tau}{\mu} = \frac{\varepsilon_{pre}(1 + \varepsilon_{pre})}{(1 + \varepsilon)} - \varepsilon. \tag{5.9}$$

Solving Eq. (5.9) for ε using the quadratic equation gives

$$\varepsilon = \frac{-\left(1+\frac{\tau}{\mu}\right)+\sqrt{\left(1-\frac{\tau}{\mu}\right)^2+4\left({\varepsilon_{pre}}^2+\varepsilon_{pre}\right)}}{2} \tag{5.10}$$

The observed strain can be calculated using Eqs. (5.5), (5.7), and (5.10)

$$e = \left(\frac{\varepsilon_{pre}}{1+\varepsilon_{pre}}\right) + \left\{\frac{\left(1+\frac{\tau}{\mu}\right) - \left(\sqrt{\left(1-\frac{\tau}{\mu}\right)^2 + 4\left({\varepsilon_{pre}}^2 + \varepsilon_{pre}\right)}\right)}{2\left(1+\varepsilon_{pre}\right)}\right\} . \tag{5.11}$$

Using approximation $\tau << \mu$, Eq. (5.11) can be written as,

$$\tau = \mu\left(1 + 2\varepsilon_{pre}\right)e \, , \tag{5.12}$$

so, the effective modulus, μ_{eff}, is

$$\mu_{eff} = \mu\left(1 + 2\varepsilon_{pre}\right) \tag{5.13}$$

During compression and under small strains, the effective modulus of the tissue is governed by the contributions from its intrinsic stiffness μ and the ratio $\frac{C_c kT}{\mu}$. The fibril pre-strain ε_{pre} — which depends on the FCD (C_c) and the intrinsic stiffness of collagen network (μ), both of which vary with depth (Fig 5.1b, middle and right) — can also be non-uniform and depth-dependent and depends on variations of these two parameters (Eq. (5.5)). The observed strain (e) under applied load can be calculated using Eq. (5.11) considering uniaxial compression (confined, constant load, equilibrium) and will be non-uniform along the depth.

5.2.1 Depth-wise variation in fiber orientation

Non-calcified, healthy, mature cartilage is commonly subdivided into three structural zones (SZ, TZ, RZ), where the lower/deeper end of the radial zone is anchored to the subchondral bone. The collagen fibers in different zones have preferred orientations, as shown in Fig 5.1b (left). The tissue is divided into three zones based on the depth-dependent angle profile θ of the collagen fibers (Xia et al. 2001)

$$\theta\,(y) = \frac{\pi}{4}\left[\tanh\left(\frac{y - m1}{m2}\right) + 1\right]. \tag{5.14}$$

To represent a typical tri-zonal architecture of mature cartilage of depth, L = 1 mm, we take $m1$ = 0.3 mm and $m2$ = 0.09 mm, where θ is the angle between the fiber direction and the plane of the articular surface (θ ~0 in SZ and θ ~ $\pi/2$ in RZ), y refers to the depth of tissue with zero at the articular surface, $m1$ refers the center of TZ or the location of most random fibers, and $m2$ determines the rate at which fibers are changing their orientation. The thickness of each zone can be determined using Eq. (5.13) (Xia et al. 2001).

5.2.2 Depth-wise variation in FCD and μ

The depth-wise increase in FCD (Fig 5.1b) is incorporated into the model using

$$C_c(y) = C_0 \exp\left(\frac{y}{r}\right) \tag{5.15}$$

where C_0 is the concentration of FCD near-surface (y = 0) and r is the rate at which concentration varies with the depth. The typical value of FCD ranges from 50–250 mM for human cartilage (Chen et al., 2001b). The calculation of FCD used in the simulations is based on a depth-dependent GAG concentration (Mittelstaedt & Xia, 2015; Xia, Zheng, et al., 2008) for mature canine cartilage, assuming 2 moles of negative charge per mole of chondroitin sulfate (one sulfate and one carboxylate), which has a molecular weight of 502.5 g/mole. These values (159–398 mM) lie within the range reported in the literature, as shown in Fig 5.1b (right). The concentration of FCD, which depends on PG concentration, is not only depth-dependent but also varies among species, types, and locations in the joint and it has also been reported to change during growth and

maturation (Julkunen et al., 2009). Therefore, the choice of C_0 and r would be sample-specific to fit the simulation results.

Another assumption in our model was that the intrinsic stiffness of the collagen network (denoted by modulus μ) in articular cartilage is anisotropic and depth-dependent (it varies with fiber orientation along its depth) as shown in Fig 5.1b (middle). We assume the collagen fibers are stiffer parallel to their length (in the RZ) than perpendicular to it (in the SZ). The stress-strain relationship in anisotropic tissue has been derived previously (Wijesinghe & Roth, 2019). For the 1D case, the collagen network modulus can be written as

$$\mu(y) = \mu_0 + \mu_1 sin^4\theta \tag{5.16}$$

where μ_0 is the modulus of the collagen network near the surface in the SZ ($\theta = 0$) and μ_1 is the additional contribution to the modulus in the RZ ($\theta = \pi/2$). Since there were no independent values reported in the literature for collagen network intrinsic stiffness, the values we have used (0.4 MPa for SZ, 0.6 MPa for RZ) are comparable to the values of solid matrix stiffness of immature bovine cartilage from carpometacarpal joints (Wang et al. 2002). The corresponding μ_0 and μ_1 are

$$\mu_0 = 0.4 \times 10^6 \qquad \text{(Pa)} \tag{5.17}$$

$$\mu_1 = 0.08 \times 10^6 \exp\left(\frac{y}{0.00099}\right) \quad \text{(Pa)} \tag{5.18}$$

In general, when an external force deforms an elastic body, the resistance to deformation is called its stiffness. It could be a function of material properties, material orientation, geometric dimensions, loading directions, type of constraint, and choice of spatial region, where loads and constraints would be applied. In the case of cartilage,

when loaded or stretched in tension, resistance to tensile deformations is offered by the intrinsic stiffness of the collagen fibers (Wijesinghe & Roth, 2019) which we assume in our model is anisotropic and increases with depth. The pre-strain ε_{pre}, which depends on the FCD (C_c) and the intrinsic stiffness of collagen network μ (Eq. (5.5)), both of which varied with depth (Eqs. (5.15) and (5.16)), would be non-uniform and depth dependent. Eq. (5.11) implies that the observed stress-strain relationship is nonlinear when the cartilage is compressed, even if the collagen stress-strain relationship is linear (defined in the text under Eq. (5.2)).

To appreciate the relative influence of collagen and proteoglycan, assume $\varepsilon_{pre} <<< 1$ and $\tau << \mu$. The effective modulus can be obtained by simplifying Eqs. (5.11) and (5.12)

$$\mu_{eff} = \mu + 2C_c kT \tag{5.19}$$

which is the sum of a term relating to the intrinsic stiffness of the collagen network and a term relating to the contribution of FCD (twice the osmotic term). As the stress becomes large, the observed strain *e* in Eq. (5.11) becomes independent of stress. If τ becomes larger than $\mu\varepsilon_{pre}(1 + \varepsilon_{pre})$, the collagen network alone cannot support compressive stress and our model no longer holds (loss of pre-stretch corresponds to $\varepsilon = 0$).

5.3 Results

5.3.1 Nonlinear strain (*e* vs τ relationship)

Fig 5.2 shows the e versus τ relation for ε_{pre}= 1. For small, applied stresses, the stress vs strain relation is linear, but with increased stress, it tends to be nonlinear even

though the elastic stress-strain relationship was linear in the model. If $\tau >> 2\mu$, the collagen loses pre-stretch ($\varepsilon = 0$).

5.3.2 Effect of variations of FCD and μ on strain

The observed strain (Eq. (5.11)) was simulated in Fig 5.3, for the given ranges of FCD and μ as two independent parameters. When both FCD and μ are small the predicted strains are large (a desirable trend for SZ of compressed cartilage), while for larger FCD and μ the strains appear smaller (RZ trend).

5.3.3 Depth-dependent strain

The simulated tissue strain is obtained by introducing depth-dependent parameters FCD and μ (Eq. (5.15) and Eq. (5.16)) considering mature healthy cartilage with L = 1 mm, $m1$ = 0.3 mm and $m2$ = 0.09 mm The FCD near the surface ($C_0 = 159$ mM) was obtained from experimental studies (Mittelstaedt and Xia 2015; Xia, Zheng, and Bidthanapally 2008), and varied with depth (r = 0.9 mm in Eq. (5.15)). The values of FCD used in this simulations are based upon the depth-varying GAG concentration (159 mM at the surface to 398 mM at radial zone) reported for mature canine humeral cartilage obtained from different experimental studies (Mittelstaedt and Xia 2015; Xia, Zheng, and Bidthanapally 2008; Zheng et al. 2009) (μMRI, μCT, and biochemical); all of them provided similar values and are strongly correlated. For preliminary analysis, the intrinsic modulus of the collagen fibers near-surface was 0.4 MPa, which increases to 0.6 MPa in deep regions as described above (Eqs. (5.16-5.18)). The simulated intra-tissue strain decreases non-homogenously through the depth (τ = 0.1 MPa) as shown in Fig 5. Positive stress or observed strain corresponds to compression in our model. The tissue strain is highest near the articular surface and

decreases (~50%) from the SZ to RZ with the middle 'kink' occurring in the transitional zone at a depth between 0.2–0.4 mm.

5.3.4 Force vs intra-tissue displacement relation.

The strains averaged over the thickness of each zone (as determined by Eq. (13)) are represented as zonal strains. The intra-tissue displacement for each zone of tissue was obtained by integrating the depth-varying observed strain '*e*' along the depth and then averaging the displacement results over the thickness of each zone. In general, the RZ has the least mean intra-tissue strain and displacement compared to the SZ and TZ, consistent with what is observed experimentally (Chen et al., 2001; Kahn et al., 2015).

Fig 5.5 represents the relationship between applied force (stress) and simulated intra-tissue displacements for three zones (SZ, TZ, RZ) of a thin rectangular sample tissue, compressed (surface-to-surface) by increasing stress (τ) in discrete steps (stress relaxation). The applied stress (τ) can be converted into force (F) as $F = \tau \times A$, where A is the surface area (A = thickness × width) in contact with the loading platen (0.25 mm²). The thickness of tissue is assumed to be ~ 120 μm, the width is ~ 2 mm, and it is compressed with a thin glass platen (thickness ~ 100 μm). The thickness and width are in the x and z directions and y refers to the depth of tissue i.e., direction perpendicular to cartilage surface. These simulated zonal relationships between force and displacement agree with the known mechanical response of cartilage under compression and are comparable to the experimental measurements of the intra-tissue displacements in mature canine humeral articular cartilage (Kahn et al., 2015) (linear model, 10–20% error). The total depth of tissue used in the simulation is 0.50 mm, compared to a cartilage depth of 0.55 mm mentioned in the experimental study (Chen et al., 2001; Kahn et al., 2015). The

rest of the parameters are the same as described above to simulate depth-dependent strain for mature tri-zonal cartilage.

5.3.5 Effective modulus for cartilage zones (stress vs strain)

Fig 5.6a presents the stress vs strain relation for three zones for the selected parameters (FCD, μ, $m1, m2$) as described earlier (Fig 5.4, Fig 5.5). The mean strain appears to increase linearly with increasing stress for all three zones. The slope of linear fit represents the effective modulus of each zone. The modulus increases with depth, from ~1 MPa in SZ to 1.6 MPa in RZ.

With the adjustment of μ (at the deep region, RZ) in the range between 1–1.5 MPa instead of 0.6 MPa, the simulation produced similar depth-dependent intra-tissue displacements and intra-tissue strains when compared with the data reported for human femoral head cartilage (Chen et al., 2001) (τ = 0.01 – 0.4 MPa). The value of μ was chosen by trial and error. The FCD used in the simulation is the same as mentioned before $(C_0 = 159 \text{ mM}, r = 0.9 \text{ mm})$, since the FCD range reported in the study by Chen et al. (2001) lies in the range reported by several other studies (Mittelstaedt & Xia, 2015; Xia, Zheng, et al., 2008; Zheng et al., 2009).

The loss of PG can cause a loss in FCD which can be attained through different enzymatic digestion (e.g., trypsin) and is the characteristic feature of degraded tissue. As a result, tissue can experience an abnormal increase in intra-tissue strains and displacements for a given otherwise-normal stress. Fig 5.6b presents the stress vs zonal strain relation for three zones of PG depleted or degraded tissue, with μ the same as normal (0.4 – 0.6 MPa), assuming no change in intrinsic properties of collagen fibers. The maximum depth-wise loss in FCD was introduced in the model using Eq. (5.15) and

adjustment of C ($C_0 = 1.59$ mM) which results in a decrease of pre-strain and a considerable increase in observable strain *e* for all three zones. The rest of the parameters are the same unless otherwise stated. The effective modulus (linear fit of stress vs zonal strain) decreases ~ 50 % for each zone as compared to normal native tissue (Fig 5.6a) and is consistent with experimental findings; selective enzymatic digestion of PGs can cause a significant drop in elastic compressive modulus of articular cartilage (Broom & Silyn-Roberts, 1990; Lyyra et al., 1999).

5.3.6 Strains between homogeneous and inhomogeneous tissues

Fig 5.7 presents several intra-tissue strains simulated for a given stress ($\tau = 0.1$ MPa) under different depth-varying conditions, including FCD and μ, between homogenous (e.g., neonatal cartilage) and inhomogeneous (e.g., healthy, mature) cartilage, L =1 mm. For comparison, a constant FCD ($C \sim C_0 = 159$ mM, $r \rightarrow \infty$) and a constant intrinsic modulus of collagen network ($\mu \sim \mu_0 = 0.4\ MPa,\ m1 = 0,\ m2 \rightarrow \infty$) were used for the homogenous case (no depth variations) keeping the rest of parameters the same as before This condition of constant intrinsic modulus of the collagen network can be attained in neonatal cartilage (Julkunen et al., 2009) or nasal cartilage (Xia et al. 2012) with a uniform fibril organization where most fibers align parallel to an external surface i.e, θ =0. The inhomogeneous case of both FCD and μ used the same parameters as to simulate depth-dependent strain in Fig 5.4. By comparison, the intra-tissue strain in articular cartilage decreases significantly with depth in the middle and deep zones when it has non-homogenous distributions of both FCD and μ (mature tissue).

5.4 Discussion

Articular cartilage has unique depth-dependent structural and material anisotropy. A better understanding of anisotropy in biological tissues is important for predicting material properties and designing novel engineering structures. Considering the tissue structural anisotropy, the effect of the force loading direction can be explored through the examination of its structural and material characteristics in the loading direction, related mostly to the anisotropic structure of the collagen network in cartilage.

The role of collagen fibers in articular cartilage under compression has been studied extensively (Alhadlaq et al., 2007b; Kääb et al., 1998; Moger et al., 2009; Wilson et al., 2007) and depth-dependent deformation and fibril reorientation responses have been reported (Alhadlaq et al., 2007a; Chen et al., 2001; Kääb et al., 1998). In mature healthy cartilage, the RZ exhibits stronger resistance to compression than the SZ and TZ. Various theoretical models (Ateshian et al., 2004; Julkunen et al., 2013; Schwartz et al., 1994; Smith et al., 2016) (e.g.; isotropic elastic, isotropic biphasic or triphasic, fibril-reinforced poroelastic, etc.) have been developed to explain the depth-dependent compressive response of articular cartilage.

In this study, we have presented the simulation results for 1D loading (normal to the articular surface) only. The model uses the structural anisotropy of the fibril network to explain the depth-dependent mechanical compressive properties of the tissue. We intend to explore the role of the zonal structure of pre-stressed collagen fibers in the loading response of cartilage and provide some insights to design advanced anisotropic fibril-reinforced models of cartilage We can examine the nonlinear strain response of articular cartilage. Our model emphasizes the structural arrangement of the collagen network that

influences the compressive nature of cartilage. A critical assumption in our model is that collagen fibers are stiffer along their longitudinal axis (RZ) than perpendicular to their axis (SZ), as illustrated in Fig 5.1c. This assumption is introduced into our modeling as a fibril modulus that varies with fiber orientation and depth (Fig 5.1b middle). When combined with a depth-wise increase in proteoglycan content (represented by the FCD; Fig 5.1b right), the collagen fibers in RZ appear to be more resistant (minimal observed strain) to uniaxial compression than SZ and TZ (maximum observed strain). Although the exact role of fibrillar mechanics in the collagen network is not clear, an increase in the fibrillar pre-strain may be associated with increasing fibrillar D-period (nanoscale structure) with depth (Inamdar et al., 2019), which in turn may be controlled by the known depth-wise variation in proteoglycan content and subsequent swelling pressure.

The fibril pre-strain in our model depends on the intrinsic stiffness μ of collagen fibers (anisotropic; higher longitudinal than transverse) and FCD. Since FCD varies with cartilage depth in addition to fibril orientation, our simulated fibril pre-strain was higher in RZ (FCD and μ higher) than SZ (FCD and μ lower). The effective modulus for SZ qualitatively agrees with experimental results (Kahn et al., 2015), while the RZ modulus (1.6 MPa) is significantly smaller than what the experimental study found (~6 MPa). We hypothesize that this difference arises because of the choice of elastic stiffness (μ) for RZ fibers (it could be higher than 0.6 MPa) and not the FCD since the FCD can be measured more easily and accurately. This hypothesis is supported by Chen et al. (Chen et al., 2001), who highlight the role of other factors (unknown) besides FCD at different depths of tissue to explain the marked increase in confined compression modulus of human femoral head articular cartilage in the deep radial zone (RZ).

When this pre-stressed structure is compressed perpendicular to the articular surface, the simulated intra-tissue displacement and observed strain decreased with depth below the articular surface (minimal observed strains appear for RZ). The simulation results are in agreement with several macro-scale experimental findings of higher compressive modulus in RZ than SZ (Kahn et al., 2015; Schinagl et al., 1996; C. Wang et al., 2002; C. Wang et al., 2003) in articular cartilage, except for some which reported the opposite trend (McLeod et al., 2013). We speculate that the model prediction of higher compressive modulus in RZ (smaller strains, strain hardening) can be explained if we assume that the intrinsic stiffness of collagen fibrils reaches a maximum when tissue is mature (closure of growth plate). If tissue is immature (growth plate open), we hypothesize that the intrinsic stiffness of collagen fibers in RZ could be smaller than in mature tissue even if both have radial fibers in the RZ. A recent study has quantified the structural differences between the immature and mature articular cartilage of rabbits by using microscopic MRI and polarized light microscopy (Mantebea et al., 2022) and we speculate that in the case of cartilage, the intrinsic stiffness of collagen fibers arises not only because of their orientation but also because of the presence of prototypic fibrils that can fuse or interlace into thicker fibrils or cross-linking, particularly in the RZ (Depalle et al., 2015; Gottardi et al., 2016; McLeod et al., 2013), which increase as tissue matures. This inter-fibril organization stabilizes the collagen assembly by the intramolecular and intermolecular linkages. This hypothesis can be tested by comparison of compressive properties of cartilage at different stages of growth and maturation, which involves structural adaptations including collagen fiber architecture.

A polarized Raman spectroscopy study combined with the nanoindentation technique (Bergholt et al., 2016) reported a marked increase in the elastic modulus in the deeper part of cartilage tissue and no correlation between composition and local mechanical modulus, which emphasized the contribution of ECM microstructural anisotropy to the tissue oppressiveness. We suggest that the local mechanical modulus of the anisotropic articular cartilage should not only depend upon the concentration of macromolecules (PG, collagen) but also the intrinsic structural properties of the extracellular matrix (ECM microstructure), including cross-linking, a shift in fiber orientation, mutual organization, etc. of the collagen fibers, which all influence fibril pre-strain and consequently the compressive stiffness.

In native mature cartilage, fibrils are pre-strained by the proteoglycans almost to their maximum limit, while this pre-strain is lost upon enzymatic digestion (e.g., trypsin, chondroitinase ABC) (Inamdar et al., 2019). This loss can lead to a significant decrease in tissue compressive modulus (Hunziker et al., 1997), but it has also been reported that PG depletion should not affect some intrinsic material properties of collagen fibers (e.g. cohesive strength, orientation, fiber-to-fiber interaction, length, width, etc.) which depend upon the structural linkages within the fibril meshwork itself (Hunziker et al., 1997) and could be a maturation-related phenomenon (Stammers et al., 2020). So, when simulating the observed strains in PG-depleted cartilage (Fig 5.6b), we assumed that loss of PG should not change the intrinsic stiffness of collagen fibers. The loss in fibril pre-strain in our case is due to the loss of FCD (PG) not the μ.

Our model can be used to estimate the mechanical response of both mature and immature articular cartilage if the selection of parameters is made accordingly. The actual

developmental changes of articular cartilage in animal growth involve complex mechanical and biochemical changes dependent upon compositional and structural changes of the extracellular matrix macromolecules including PGs and collagen fibers. We speculate that the intra-tissue strains and displacements during uniaxial compressive loading could be higher in the deep zone of immature or neonatal tissue, which is devoid of radial fibers and possesses approximately a non-structural organization with most fibers parallel to the articular surface. So, structurally a homogeneous tissue (neonatal) with no change in intrinsic stiffness of collagen fibers (0.4 MPa) through depth and with no change or increase in FCD to depth (Fig 5.7) will have a smaller compressive modulus than structurally inhomogeneous tissue (mature), which is consistent with Gannon et al.'s (2015) findings. In general, it is useful to study the local strains in the tissue as they may regulate cell function and metabolism (Torzilli et al., 2006).

5.4.1 Assumptions and Limitations

Applied stress in our model is global stress and the slope of a linear fit to stress vs strain does not represent a real quantification of zonal modulus but gives qualitative information about the local modulus based on the contribution of FCD and collagen fibril pre-stress. In addition, the relationship between the stress and the mean zonal strain appears linear within the model limits (smaller strains) and our choice of parameters. If a nonlinear relationship exists between stress and strain in the tissue, the predicted zonal modulus will change.

The compositional and ultrastructural features of cartilage lead to inhomogeneity and anisotropy in mechanical properties; sometimes it is difficult to distinguish the independent effect of one rather than the other. The functional properties of cartilage

depend on its non-homogeneous extracellular matrix molecular composition and structure. Besides normal depth-wise variations in composition and structure, the proteoglycan and collagen vary significantly in content during growth and maturation along with strong structural adaptations. Currently, the clear answer to the question of what component of collagen fibers determines the intrinsic stiffness (resistance to pre-stretch in case of osmotic swelling i.e., in pre-strain condition) and how it varies along with the depth is not clear. In general, the intrinsic properties of the collagen network can depend on its collagen content, type, size/diameters of collagen fibers, crosslinking, fiber-to-fiber interaction, fiber orientation, and strength of macromolecular interactions modulated by the collagen network. It should ideally be independent of GAG/FCD concentration but can be affected by the interactions involving the collagen network and PG together.

It has also been reported that articular cartilage obtained from different joints of the same animal can be different in its composition and similarly, the cartilage obtained from weight-bearing and non-weight-bearing regions of the same joint can offer different stiffness under the same loading conditions. Therefore, for the theoretical analysis and comparisons of the compressive behavior under the same loading conditions, the choice of parameters including collagen network stiffness depends upon the sample and its conditions under consideration, which requires sophisticated and careful measurements of biochemical and biomechanical gradients.

Modern models are complex and require several parameters to describe the overall mechanical behavior. With a great number of tissue components and material parameters, the models become prone to uncertainties caused by the assumptions, for

example, in the interactions between the model components. Although the model may be plausible in theory, these uncertainties need to be addressed and the model implementation and function should be verified before the model can be applied.

Figure 5.1

Schematics of the modeling

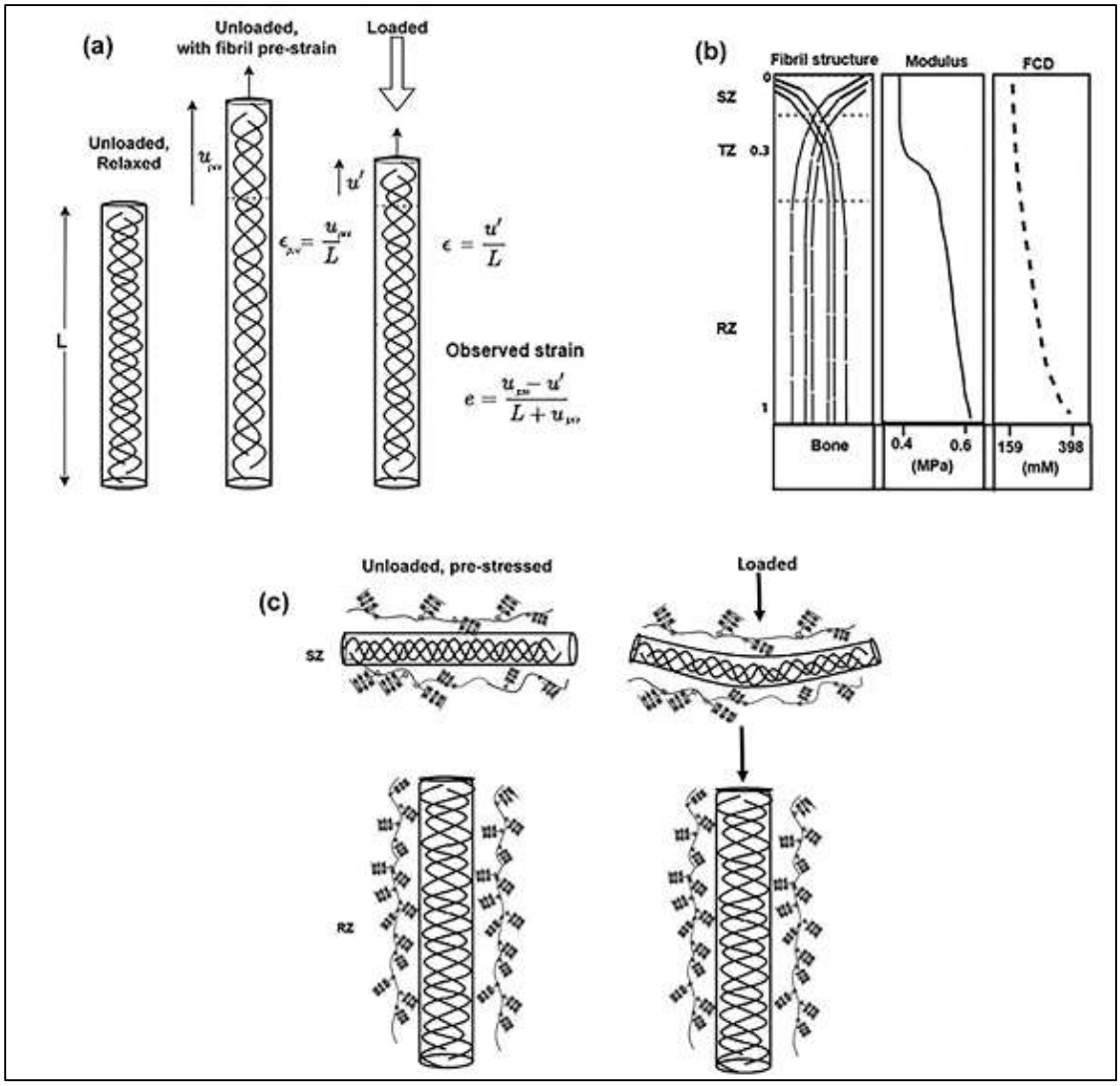

Note. Consider a 1D tissue of length L (embedded with collagen fibrils), without any pre-strain (Relaxed, zero pre-strain condition). Then an unloaded tissue with 1D pre-strain ε_{pre}, which is due to the internal FCD that causes 1D displacement u_{pre}. When the pre-stressed tissue is under loading (i.e., a confined compression), the 1D tissue length changes from u_{pre} to u', where the subsequent strain is represented by ε. The e represents the observed strain because of the difference between two strains (ε_{pre} and ε).

(b) The depth-dependent variations in articular cartilage, where the collagen fibers have a tri-zonal organization, the 1D depth-dependent modulus (μ) of the collagen fibers, and the depth-dependent FCD that represents the concentration changes of proteoglycans. The values shown in the modulus and FCD are used in the simulation.

(c) The schematics of collagen fibers (loaded and un-loaded) in SZ (parallel and thinner in diameters ~ 50 μm) and RZ (perpendicular and thicker in diameters ~ 100-200 μm). The PGs entangle around the fibers (lesser in content in SZ than RZ) and cause the fibril pre-strain which depends on both FCD and μ. Fibers in SZ are easier to compress than the fibers in RZ under uniaxial loading (the third panel). No significant structural changes happen to the radial zone collagen fibers under loading.

Figure 5.2

The relationship between applied stress τ and observed strain e for an assumed pre-strain $\varepsilon_{pre} = 1$.

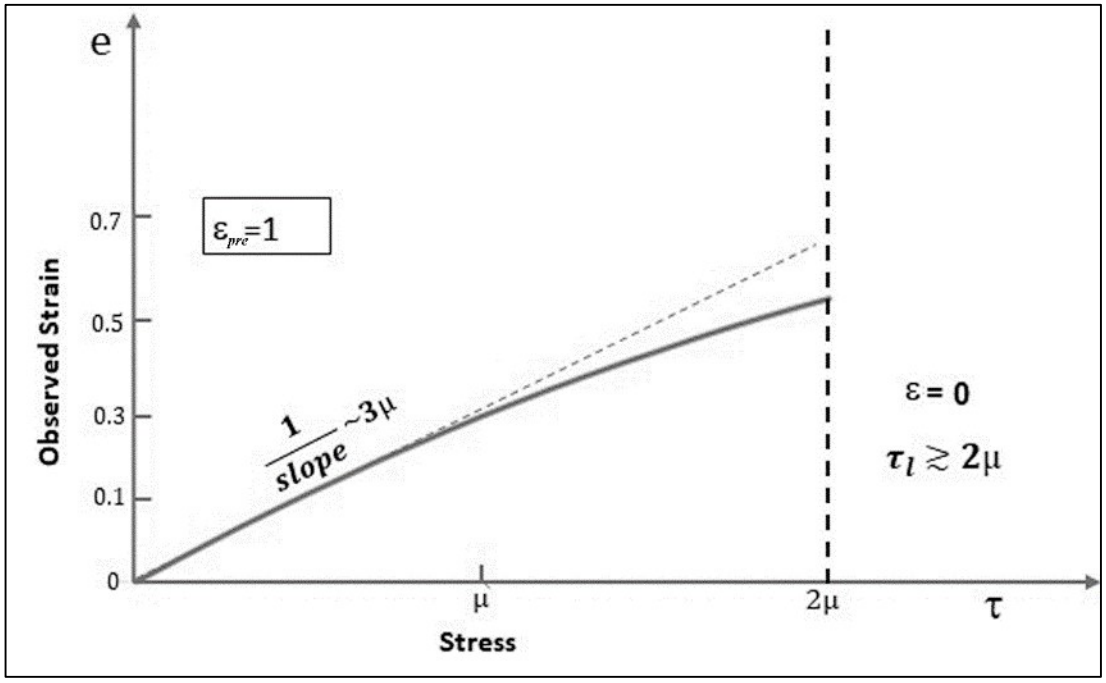

Note. Originally the collagen pre-stress (μ) was assumed linear, and the stress-strain relationship appears nonlinear when τ becomes larger than μ. At smaller stress, the effective modulus (1/slope) is 3μ; the collagen fibers lose pre-strain ($\varepsilon = 0$), and can no longer support compressive load if the applied stress becomes greater than 2μ.

Figure 5.3

Effect of varying FCD and μ on simulated strains for a given stress (τ = *0.2 MPa)*

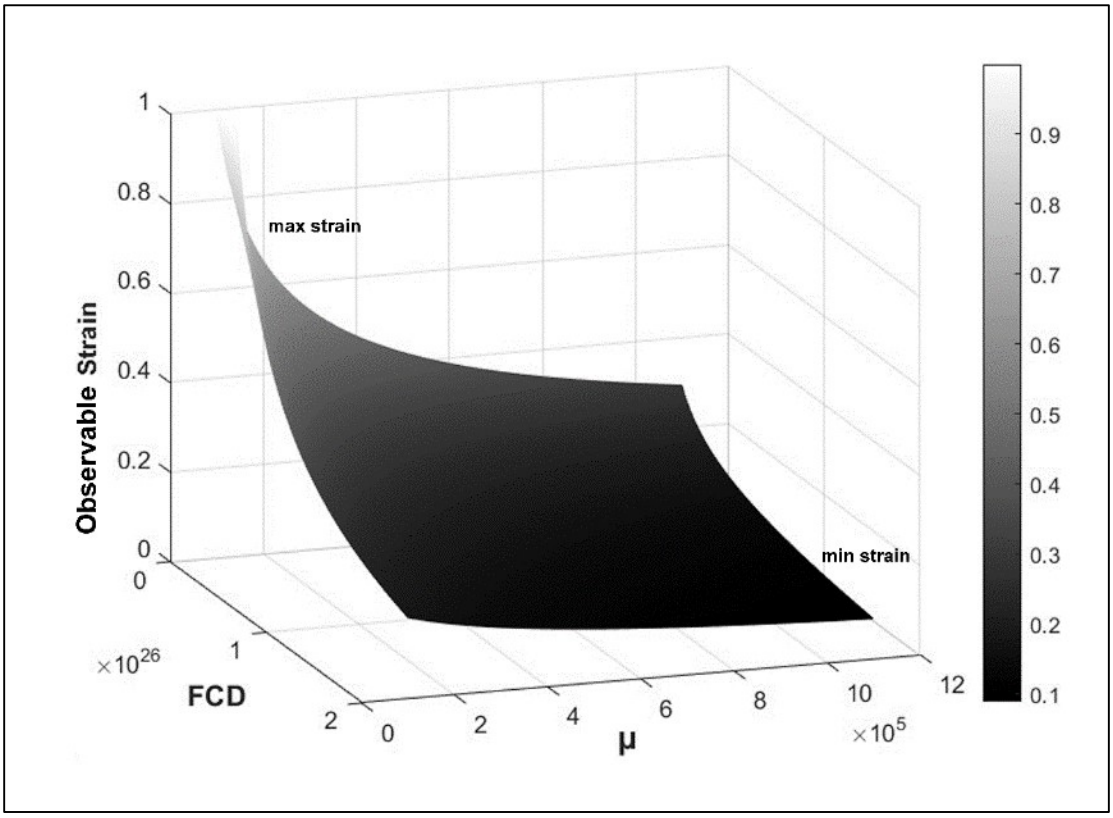

Note. When both FCD and μ are towards the smaller end, the strains are larger (a known trend for SZ of cartilage under compression), while for larger FCD and μ, the strains appear smaller (RZ trend).

Figure 5.4

The simulated observed strain e over depth when both FCD and μ are-varying with depth.

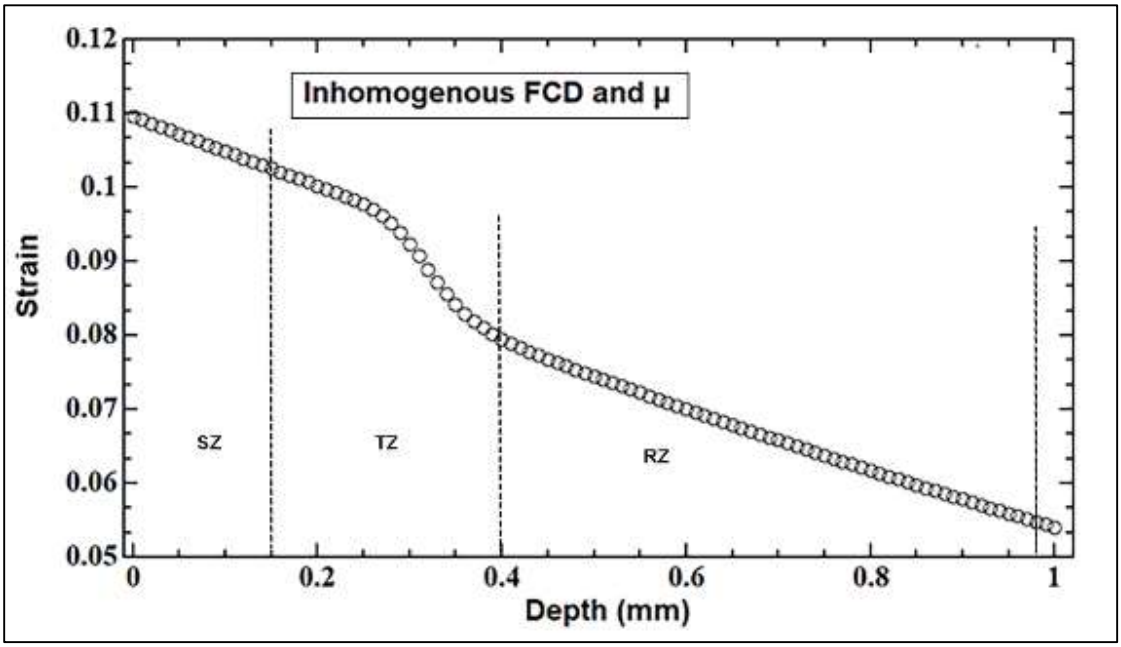

Note. The tri-zonal tissue has a length L = 1 mm ($m1$ = 0.3 mm, $m2$ = 0.09 mm), and under the applied stress $\tau = 0.1$ MPa. The tissue strain is the highest at the articular surface and decreases from the surface zone (SZ) to the deep radial zone (RZ).

.

Figure 5.5

The equilibrium force vs intra-tissue displacement plots for three pre-defined zones (SZ, TZ, RZ).

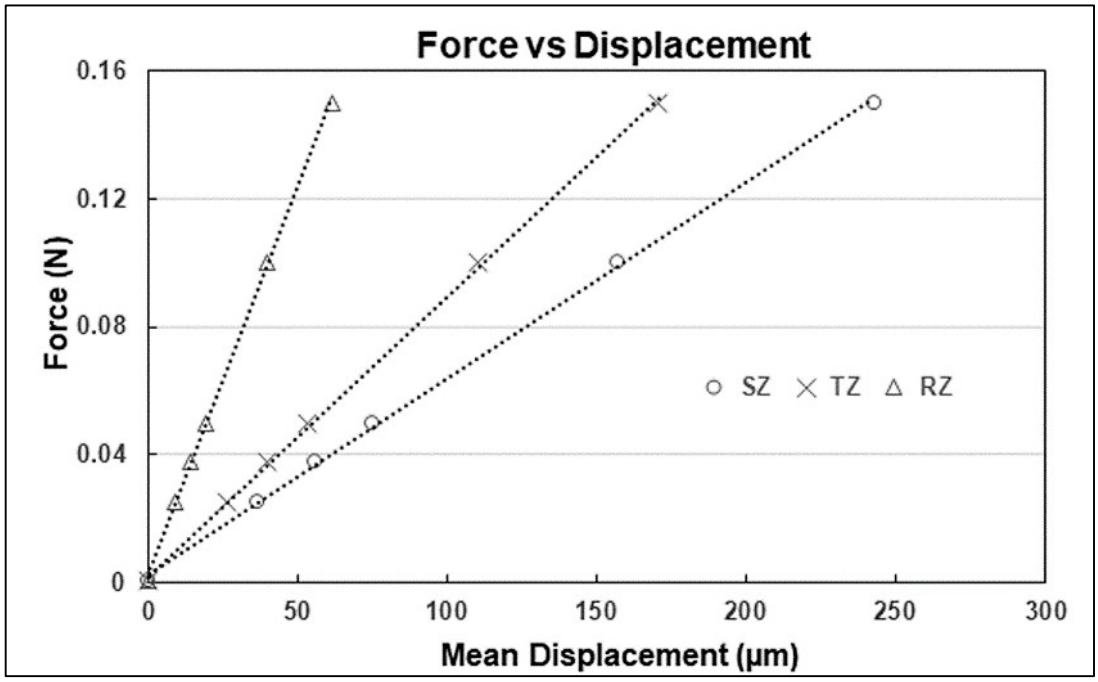

Note. The intra-tissue displacements increased linearly with increasing force/stress for all three zones but the increase in intra-tissue displacements for SZ and TZ is significantly higher as compared to RZ. The zonal strains (SZ, TZ, and RZ) in cartilage are obtained by averaging the depth-dependent strain values for the respective zones defined by Eq. (5.13), where SZ is 15% of the total thickness, TZ is 25% of the total thickness, and RZ is the ~ 60% of the total thickness. The total depth of tissue used in the simulation is 0.5 mm.

Figure 5.6

The effective compressive modulus, μ_{eff}, in three zones in a simulated 'mature healthy and 'mature degraded cartilage'

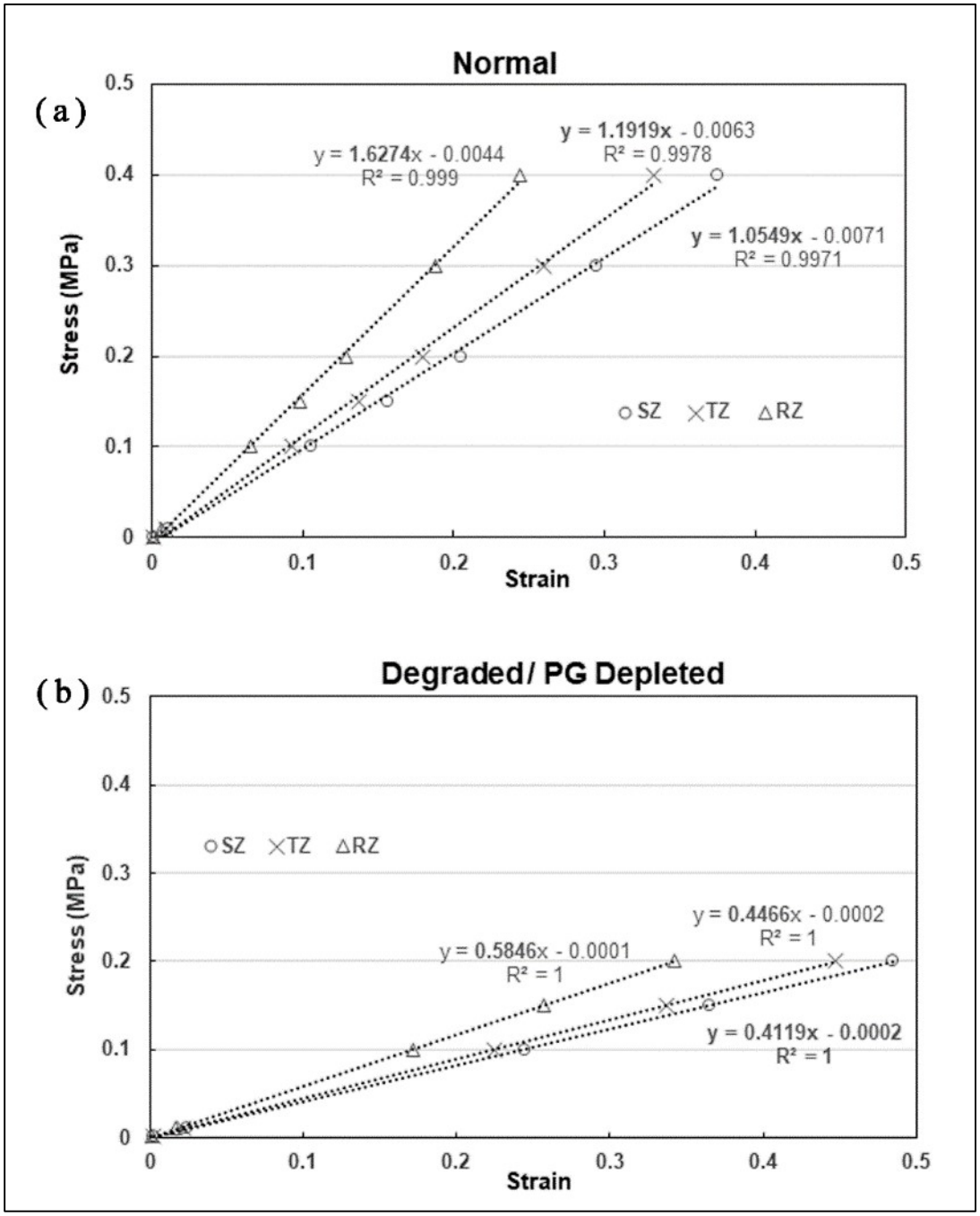

Note. The slope of linear fit using stress-strain relationship represents the μ_{eff}. (a) For the SZ the modulus is ~ 1 MPa (consistent with several experimental studies) and increases to ~1.6 MPa (smaller than what is reported by other studies) in the deep region (RZ). The discrepancy in RZ modulus was attributed to the choice of elastic stiffness (μ) for RZ fibers (which could be higher than 0.6 MPa). (b) Loss of PG or FCD results in a decrease in pre-strain ε_{pre}, an increase in the intra-tissue strains (~50%) for the given stress, and consequently a decrease in effective modulus (slope of linear fit) for each zone (60% for SZ, 62% for TZ, and 64% for RZ). In other words, the amount of force required to compress the tissue is smaller than the normal tissue. The depth-wise loss of FCD was introduced in the model by adjusting SZ FCD (C_0) from 159 mM to 1.59 mM (~99% decrease), and in RZ from 398 mM to 79.6 mM, (~80% decrease), while the μ (0.4 MPa-0.6 MPa) is the same as used for the normal case.

Figure 5.7

The simulated strains for the given stress ($\tau = 0.1$ MPa) at different parameter conditions (FCD, μ, homogenous and non-homogenous) as the function of the tissue depth

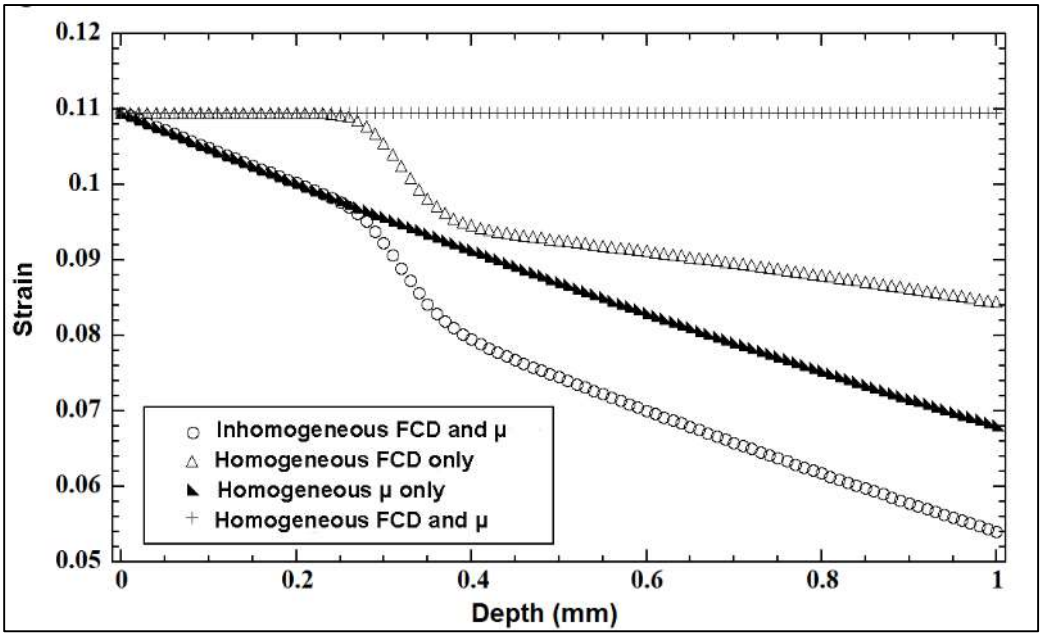

Note. A constant FCD (159 mM) and constant intrinsic modulus of collagen fibers (0.4 MPa) were used for the homogenous tissue. Homogenous distributions of both FCD and μ along the depth generated constant strain values. When non-homogenous distributions of both FCD and μ were added to the model, the intra-tissue strain decreases significantly with increasing depth.

CHAPTER SIX

SUMMARY AND FUTURE DIRECTIONS

6.1 Summary

This dissertation contains three individual projects; two of them have been published in peer-reviewed journals and the third one will be submitted to a journal.

In the first project, we successfully established the baseline characteristics of the rabbits' humeral and femoral cartilage, using quantitative MRI relaxation times (T2, T1ρ, T1) and quantitative PLM measures (retardation, angle). To the best of our knowledge, these μMRI results are the first quantitative characterization of the entire depth of humeral and femoral cartilage in rabbits at a sub-10 μm resolution; the highest MRI resolution in cartilage research. Comparing the sub-10 μm μMRI results with low-resolution MRI results (70–82 μm) demonstrates the importance of having the sufficient resolution in MRI for the zonal assessment of articular cartilage. The quantitative PLM imaging (retardation, angle) at 1.0 μm and 4.0 μm pixel resolution further verify and enhance the high-resolution MRI results, which provides the anatomic knowledge that can be correlated with non-invasive MRI results. This project provides the baseline data for any future use of the rabbit model in the bench-top investigation of OA.

In the second project, we studied the topographical variations among different locations on the medial femoral condyle of juvenile rabbits. Distinctly different characteristics of tissue properties especially the arrangement of collagen fibers and chondrocytes that were found in the cartilage at different locations on the femoral condyle, likely related to the structural variations of different matrices in cartilage. Such

structural variations were not present in mature rabbit articular cartilage (>1 year). Such variations have a direct impact on the quantitative measurements of T2 relaxation times and PLM measurements (angle, orientation). Our high-resolution imaging findings in the location-specific differences in knee joint's collagen fiber organization can help to better understand juvenile tissue diagnostic imaging, developmental biology, localized mechanobiology, tissue engineering, and design of more successful repair strategies.

In the third project, a mathematical model was used to calculate the anisotropic collagen fibril mechanics in articular cartilage under 1D axial compression (perpendicular-to-surface direction). Under the assumption that collagen fibers are stiffer parallel to their length than perpendicular to it when combined with a depth-varying concentration of FCD, the model successfully predicted the typical depth-dependent trends of zone-specific strains and displacements (both decreasing with depth). In general, the model supports the hypothesis that the depth-dependent compressive response of articular is not only dependent upon the concentration of proteoglycans but also the anisotropic mechanical properties of the pre-strained collagen fibril network. A better understanding of anisotropy in biological tissues is important for predicting material properties and designing novel engineering structures.

6.2 Future directions

To study the depth-dependent characteristics of rabbit cartilage, sub-10 μm pixel resolution is sufficient and necessary in quantitative MRI. One of the limitations of using a magnetization-prepared spin-echo sequence to achieve sufficient SNR at high resolution is the long scan time. We plan to introduce compressed sensing techniques combined with our currently used pulse sequences to accelerate the acquisition process of

T2, T1ρ, and T1 quantification on cartilage imaging without sacrificing accuracy. Recent new approaches (Geethanath et al., 2013; Madelin et al., 2012; Pandit et al., 2016) with compressed sensing (CS) have a reasonable potential to provide accurate and fast quantitative cartilage assessment and provide a way to make quantitative imaging techniques more accessible for clinical applications.

We have identified distinct variations in terms of collagen fibril structure and chondrocyte arrangement in juvenile rabbit femur cartilage. In the future, we intend to use this topographical knowledge to design location-specific biochemical, and biomechanical studies on rabbit femur cartilage to obtain more insights into their microenvironment and their role in development and biomechanics. We are interested to know why some sites (usually central in joint) attain trizonal architecture earlier than others (peripheral) and which factors are responsible for converting mono-zonal homogenous fibril architecture to mature trizonal architecture. New studies can include mapping the metabolic activity of chondrocytes and biochemical compositional differences present on the joint surface. We would further like to explore whether the difference in the structural development of collagen fiber at different locations of joints during growth and maturation can have any implication in case of tissue degradation and can this knowledge be useful in improving cartilage repair. Our location specific T2 anisotropy and PLM retardation and orientation data can be correlated with biomechanical behavior (modulus, stiffness, etc.) of structurally different locations.

We intend to use our mathematical model in conjunction with biomechanical testing on cartilage, to explore the role of structural anisotropy in tissue loading response and to separate the structure-composition effect. When compressed, tissue strains are

predicted to be higher in the deep zone in the absence of radial fibers (no trizonal architecture). This prediction can be tested using mechanical compression tests on sites with and without zonal arrangement and measuring the zonal strains.

APPENDIX A

COPYRIGHT LETTERS OF PERMISSION TO REPRODUCE

Fig 2.1

JOHN WILEY AND SONS LICENSE
TERMS AND CONDITIONS
Dec 13, 2022

This Agreement between Syeda Batool ("You") and John Wiley and Sons ("John Wiley and Sons") consists of your license details and the terms and conditions provided by John Wiley and Sons and Copyright Clearance Center.

License Number	5447250849775
License date	Dec 13, 2022
Licensed Content Publisher	John Wiley and Sons
Licensed Content Publication	JOURNAL OF BIOMEDICAL MATERIALS RESEARCH PART A
Licensed Content Title	Functional biomaterials for cartilage regeneration
Licensed Content Author	Zigang Ge, Chao Li, Boon Chin Heng, et al
Licensed Content Date	Apr 10, 2012
Licensed Content Volume	100A
Licensed Content Issue	9
Licensed Content Pages	11
Type of use	Dissertation/Thesis
Requestor type	University/Academic
Format	Electronic
Portion	Figure/table
Number of figures/tables	1
Will you be translating?	No
Title	Dissertation
Institution name	Oakland university
Expected presentation date	Jan 2023

Portions	Figure1
	Syeda Batool 244 Meadow Brook Road Room #165 Hannah Hall
Requestor Location	
	ROCHESTER, MI 48309 United States Attn: Syeda Batool
Publisher Tax ID	EU826007151
Total	0.00 USD
Terms and Conditions	

TERMS AND CONDITIONS

This copyrighted material is owned by or exclusively licensed to John Wiley & Sons, Inc. or one of its group companies (each a"Wiley Company") or handled on behalf of a society with which a Wiley Company has exclusive publishing rights in relation to a particular work (collectively "WILEY"). By clicking "accept" in connection with completing this licensing transaction, you agree that the following terms and conditions apply to this transaction (along with the billing and payment terms and conditions established by the Copyright Clearance Center Inc., ("CCC's Billing and Payment terms and conditions"), at the time that you opened your RightsLink account (these are available at any time at http://myaccount.copyright.com).

Terms and Conditions

- The materials you have requested permission to reproduce or reuse (the "Wiley Materials") are protected by copyright.
- You are hereby granted a personal, non-exclusive, non-sub licensable (on a stand-alone basis), non-transferable, worldwide, limited license to reproduce the Wiley Materials for the purpose specified in the licensing process. This license, **and any CONTENT (PDF or image file) purchased as part of your order,** is for a one-time use only and limited to any maximum distribution number specified in the license. The first instance of republication or reuse granted by this license must be completed within two years of the date of the grant of this license (although copies prepared before the end date may be distributed thereafter). The Wiley Materials shall not be used in any other manner

or for any other purpose, beyond what is granted in the license. Permission is granted subject to an appropriate acknowledgement given to the author, title of the material/book/journal and the publisher. You shall also duplicate the copyright notice that appears in the Wiley publication in your use of the Wiley Material. Permission is also granted on the understanding that nowhere in the text is a previously published source acknowledged for all or part of this Wiley Material. Any third party content is expressly excluded from this permission.

- With respect to the Wiley Materials, all rights are reserved. Except as expressly granted by the terms of the license, no part of the Wiley Materials may be copied, modified, adapted (except for minor reformatting required by the new Publication), translated, reproduced, transferred or distributed, in any form or by any means, and no derivative works may be made based on the Wiley Materials without the prior permission of the respective copyright owner.**For STM Signatory Publishers clearing permission under the terms of the STM Permissions Guidelines only, the terms of the license are extended to include subsequent editions and for editions in other languages, provided such editions are for the work as a whole in situ and does not involve the separate exploitation of the permitted figures or extracts,** You may not alter, remove or suppress in any manner any copyright, trademark or other notices displayed by the Wiley Materials. You may not license, rent, sell, loan, lease, pledge, offer as security, transfer or assign the Wiley Materials on a stand-alone basis, or any of the rights granted to you hereunder to any other person.

- The Wiley Materials and all of the intellectual property rights therein shall at all times remain the exclusive property of John Wiley & Sons Inc, the Wiley Companies, or their respective licensors, and your interest therein is only that of having possession of and the right to reproduce the Wiley Materials pursuant to Section 2 herein during the continuance of this Agreement. You agree that you own no right, title or interest in or to the Wiley Materials or any of the intellectual property rights therein. You shall have no rights hereunder other than the license as provided for above in Section 2. No right, license or interest to any trademark, trade name, service mark or other branding ("Marks") of WILEY or its licensors is granted hereunder, and you agree that you shall not assert any such right, license or interest with respect thereto

- NEITHER WILEY NOR ITS LICENSORS MAKES ANY WARRANTY OR REPRESENTATION OF ANY KIND TO YOU OR ANY THIRD PARTY, EXPRESS, IMPLIED OR STATUTORY, WITH RESPECT TO THE MATERIALS OR THE ACCURACY OF ANY INFORMATION CONTAINED IN THE MATERIALS, INCLUDING, WITHOUT LIMITATION, ANY IMPLIED WARRANTY OF MERCHANTABILITY, ACCURACY, SATISFACTORY QUALITY, FITNESS FOR A PARTICULAR PURPOSE, USABILITY, INTEGRATION OR NON-INFRINGEMENT AND ALL SUCH WARRANTIES ARE HEREBY EXCLUDED BY WILEY AND ITS LICENSORS AND WAIVED BY YOU.

- WILEY shall have the right to terminate this Agreement immediately upon breach of this Agreement by you.

- You shall indemnify, defend and hold harmless WILEY, its Licensors and their respective directors, officers, agents and employees, from and against any actual or threatened claims, demands, causes of action or proceedings arising from any breach of this Agreement by you.

- IN NO EVENT SHALL WILEY OR ITS LICENSORS BE LIABLE TO YOU OR ANY OTHER PARTY OR ANY OTHER PERSON OR ENTITY FOR ANY SPECIAL, CONSEQUENTIAL, INCIDENTAL, INDIRECT, EXEMPLARY OR PUNITIVE DAMAGES, HOWEVER CAUSED, ARISING OUT OF OR IN CONNECTION WITH THE DOWNLOADING, PROVISIONING, VIEWING OR USE OF THE MATERIALS REGARDLESS OF THE FORM OF ACTION, WHETHER FOR BREACH OF CONTRACT, BREACH OF WARRANTY, TORT, NEGLIGENCE, INFRINGEMENT OR OTHERWISE (INCLUDING, WITHOUT LIMITATION, DAMAGES BASED ON LOSS OF PROFITS, DATA, FILES, USE, BUSINESS OPPORTUNITY OR CLAIMS OF THIRD PARTIES), AND WHETHER OR NOT THE PARTY HAS BEEN ADVISED OF THE POSSIBILITY OF SUCH DAMAGES. THIS LIMITATION SHALL APPLY NOTWITHSTANDING ANY FAILURE OF ESSENTIAL PURPOSE OF ANY LIMITED REMEDY PROVIDED HEREIN.

- Should any provision of this Agreement be held by a court of competent jurisdiction to be illegal, invalid, or unenforceable, that provision shall

be deemed amended to achieve as nearly as possible the same economic effect as the original provision, and the legality, validity and enforceability of the remaining provisions of this Agreement shall not be affected or impaired thereby.

- The failure of either party to enforce any term or condition of this Agreement shall not constitute a waiver of either party's right to enforce each and every term and condition of this Agreement. No breach under this agreement shall be deemed waived or excused by either party unless such waiver or consent is in writing signed by the party granting such waiver or consent. The waiver by or consent of a party to a breach of any provision of this Agreement shall not operate or be construed as a waiver of or consent to any other or subsequent breach by such other party.

- This Agreement may not be assigned (including by operation of law or otherwise) by you without WILEY's prior written consent.

- Any fee required for this permission shall be non-refundable after thirty (30) days from receipt by the CCC.

- These terms and conditions together with CCC's Billing and Payment terms and conditions (which are incorporated herein) form the entire agreement between you and WILEY concerning this licensing transaction and (in the absence of fraud) supersedes all prior agreements and representations of the parties, oral or written. This Agreement may not be amended except in writing signed by both parties. This Agreement shall be binding upon and inure to the benefit of the parties' successors, legal representatives, and authorized assigns.

- In the event of any conflict between your obligations established by these terms and conditions and those established by CCC's Billing and Payment terms and conditions, these terms and conditions shall prevail.

- WILEY expressly reserves all rights not specifically granted in the combination of (i) the license details provided by you and accepted in the course of this licensing transaction, (ii) these terms and conditions and (iii) CCC's Billing and Payment terms and conditions.

- This Agreement will be void if the Type of Use, Format, Circulation, or Requestor Type was misrepresented during the licensing process.

- This Agreement shall be governed by and construed in accordance with the laws of the State of New York, USA, without regards to such state's conflict of law rules. Any legal action, suit or proceeding arising out of or relating to these Terms and Conditions or the breach thereof shall be instituted in a court of competent jurisdiction in New York County in the State of New York in the United States of America and each party hereby consents and submits to the personal jurisdiction of such court, waives any objection to venue in such court and consents to service of process by registered or certified mail, return receipt requested, at the last known address of such party.

WILEY OPEN ACCESS TERMS AND CONDITIONS

Wiley Publishes Open Access Articles in fully Open Access Journals and in Subscription journals offering Online Open. Although most of the fully Open Access journals publish open access articles under the terms of the Creative Commons Attribution (CC BY) License only, the subscription journals and a few of the Open Access Journals offer a choice of Creative Commons Licenses. The license type is clearly identified on the article.

The Creative Commons Attribution License

The Creative Commons Attribution License (CC-BY) allows users to copy, distribute and transmit an article, adapt the article and make commercial use of the article. The CC-BY license permits commercial and non-

Creative Commons Attribution Non-Commercial License

The Creative Commons Attribution Non-Commercial (CC-BY-NC)License permits use, distribution and reproduction in any medium, provided the original work is properly cited and is not used for commercial purposes.(see below)

Creative Commons Attribution-Non-Commercial-NoDerivs License

The Creative Commons Attribution Non-Commercial-NoDerivs License (CC-BY-NC-ND) permits use, distribution and reproduction in any medium,

Fig 2.4

CCC Marketplace

This is a License Agreement between Syeda Batool ? Oakland University ("User") and Copyright Clearance Center, Inc. ("CCC") on behalf of the Rightsholder identified in the order details below. The license consists of the order details, the Marketplace Order General Terms and Conditions below, and any Rightsholder Terms and Conditions which are included below.

All payments must be made in full to CCC in accordance with the Marketplace Order General Terms and Conditions below.

Order Date	30-Dec-2022	Type of Use	Republish in a thesis/dissertation
Order License ID	1305762-1	Publisher	IOP Publishing
ISSN	0031-9155	Portion	Chart/graph/table/figure

LICENSED CONTENT

Publication Title	Physics in Medicine & Biology	Country	United Kingdom of Great Britain and Northern Ireland
Author/Editor	American Association of Physicists in Medicine, Canadian Association of Physicists.Medical and Biological Physics Division, Institute of Physics (Great Britain), Hospital Physicists' Association, Deutsche Gesellschaft für Medizinische Physik., International Organization for Medical Physics	Rightsholder	IOP Publishing, Ltd
		Publication Type	Journal
Date	01/01/1956		
Language	English		

REQUEST DETAILS

Portion Type	Chart/graph/table/figure	Distribution	United States
Number of Charts / Graphs / Tables / Figures Requested	1	Translation	Original language of publication
		Copies for the Disabled?	No
Format (select all that apply)	Electronic	Minor Editing Privileges?	Yes
Who Will Republish the Content?	Academic institution	Incidental Promotional Use?	No
Duration of Use	Life of current edition	Currency	USD
Lifetime Unit Quantity	Up to 499		
Rights Requested	Main product and any product related to main product		

NEW WORK DETAILS

Title	SUB-10 μm REOLUTIONS STUDY OF YOUNG RABBIT CARTILAGE BY QUANTITATIVE μMRI AND POLARIZED MICROSCOPY	Institution Name	Oakland University
		Expected Presentation Date	2022-12-30
Instructor Name	Yang Xia		

ADDITIONAL DETAILS

Order Reference Number	N/A	The Requesting Person/Organization to Appear on the License	Syeda Batool ? Oakland University

REUSE CONTENT DETAILS

Title, Description or Numeric Reference of the Portion(s)	Fig 5. The The schematics of collagen fibril structure and GAG distribution in both healthy (a) and degraded cartilage (b)	Title of the Article/Chapter the Portion Is From	MRI properties of a unique hypo-intense layer in degraded articular cartilage
		Author of Portion(s)	Nian Wang, Farid Badar and Yang Xia1
Editor of Portion(s)	N/A	Issue, if Republishing an Article From a Serial	N/A
Volume of Serial or Monograph	N/A		
Page or Page Range of Portion	N/A	Publication Date of Portion	1956-01-01

RIGHTSHOLDER TERMS AND CONDITIONS

These special terms and conditions are in addition to the standard terms and conditions for CCC's Republication Service and, together with those standard terms and conditions, govern the use of the Works. As the User you will make all reasonable efforts to contact the author(s) of the article which the Work is to be reused from, to seek consent for your intended use. Contacting one author who is acting expressly as authorised agent for their co-author(s) is acceptable. User will reproduce the following wording prominently alongside the Work: the source of the Work, including author, article title, title of journal, volume number, issue number (if relevant), page range (or first page if this is the only information available) and date of first publication; and a link back to the article (via DOI); and if practicable, and IN ALL CASES for new works published under any of the Creative Commons licences, the words "© Institute of Physics and Engineering in Medicine. Reproduced by permission of IOP Publishing Ltd. All rights reserved" Without the express permission of the author(s) and the Rightsholder of the article from which the Work is to be reused, User shall not use it in any way which, in the opinion of IOP Publishing Ltd, could: (i) distort or alter the author(s)' original intention(s) and meaning; (ii) be prejudicial to the honour or reputation of the author(s); and/or (iii) imply endorsement by the author(s) and/or the Rightsholder and/or IOP Publishing Ltd. This licence does not apply to any article which is credited to another source and which does not have the copyright line '© Institute of Physics and Engineering in Medicine'. User must check the copyright line of the article from which the Work is to be reused to check that the Rightsholder and IOP Publishing Ltd have all the necessary rights to be able to grant permission. User is solely responsible for identifying and obtaining separate licences and permissions from the copyright owner for reuse of any such third party material/figures which the Rightsholder is not the copyright owner of. The Rightsholder shall not reimburse any fees which User pays for a republication license for such third party content. This licence does not apply to any material/figure which is credited to another source in the Rightsholder's publication or has been obtained from a third party. User must check the Version of Record of the article from which the Work is to be reused, to check whether any of the material in the Work is third party material. Third party citations and/or copyright notices and/or permissions statements may not be included in any other version of the article from which the Work is to be reused and so cannot be relied upon by the User. User is solely responsible for identifying and obtaining separate licences and permissions from the copyright owner for reuse of any such third party material/figures where the Rightsholder is not the copyright owner. The Rightsholder shall not reimburse any fees which User pays for a republication license for such third party content. User and CCC acknowledge that IOP Publishing Ltd and/or the Rightsholder may, from time to time, make changes or additions to these special terms and conditions without express notification, provided that these shall not apply to permissions already secured and paid for by User prior to such change or addition. User acknowledges that the Rightsholder and IOP Publishing Ltd (which includes companies within its group and third parties for whom it publishes its titles) may make use of personal data collected through the service in the course of their business. If User is the author of the Work, User may automatically have the right to reuse it under the rights granted back when User transferred the copyright in the article to the Rightsholder. User should check the copyright form and the relevant author rights policy to check whether permission is required. If User is the author of the Work and does require permission for proposed reuse of the Work, User should select 'Author of requested content' as the Requestor Type. The Rightsholder shall not reimburse any fees which User pays for a republication license. If User is the author of the article which User wishes to reuse in User's thesis or dissertation, the republication licence covers the right to include the Version of Record of the article, provided it is not then published commercially. User must include citation details and, for online use, a link to the Version of Record of the article on the IOPscience website. User may need to obtain separate permission for any third party content included within the article. User must check this with the copyright owner of such third party content. User may not include the article in a thesis or dissertation which is published by ProQuest. Any other commercial use of User's thesis or dissertation containing the article would also need to be expressly notified in writing to the Rightsholder at the time of request and would require separate written permission from the Rightsholder. As well as CCC, the Rightsholder and IOP Publishing Ltd shall have the right to bring any legal action that they deem necessary to enforce their rights should they consider that the Work infringes those rights in any way. For content reuse requests that qualify for permission under the STM Permissions Guidelines, which may be updated from time to time, the STM Permissions Guidelines supplement the terms and conditions contained in this license.

Marketplace Order General Terms and Conditions

The following terms and conditions ("General Terms"), together with any applicable Publisher Terms and Conditions, govern User's use of Works pursuant to the Licenses granted by Copyright Clearance Center, Inc. ("CCC") on behalf of the applicable Rightsholders of such Works through CCC's applicable Marketplace transactional licensing services (each, a "Service").

1) **Definitions.** For purposes of these General Terms, the following definitions apply:

"License" is the licensed use the User obtains via the Marketplace platform in a particular licensing transaction, as set forth in the Order Confirmation.

"Order Confirmation" is the confirmation CCC provides to the User at the conclusion of each Marketplace transaction. "Order Confirmation Terms" are additional terms set forth on specific Order Confirmations not set forth in the General Terms that can include terms applicable to a particular CCC transactional licensing service and/or any Rightsholder-specific terms.

"Rightsholder(s)" are the holders of copyright rights in the Works for which a User obtains licenses via the Marketplace platform, which are displayed on specific Order Confirmations.

"Terms" means the terms and conditions set forth in these General Terms and any additional Order Confirmation Terms collectively.

"User" or "you" is the person or entity making the use granted under the relevant License. Where the person accepting the Terms on behalf of a User is a freelancer or other third party who the User authorized to accept the General Terms on the User's behalf, such person shall be deemed jointly a User for purposes of such Terms.

"Work(s)" are the copyright protected works described in relevant Order Confirmations.

2) **Description of Service.** CCC's Marketplace enables Users to obtain Licenses to use one or more Works in accordance with all relevant Terms. CCC grants Licenses as an agent on behalf of the copyright rightsholder identified in the relevant Order Confirmation.

3) **Applicability of Terms.** The Terms govern User's use of Works in connection with the relevant License. In the event of any conflict between General Terms and Order Confirmation Terms, the latter shall govern. User acknowledges that Rightsholders have complete discretion whether to grant any permission, and whether to place any limitations on any grant, and that CCC has no right to supersede or to modify any such discretionary act by a Rightsholder.

4) **Representations; Acceptance.** By using the Service, User represents and warrants that User has been duly authorized by the User to accept, and hereby does accept, all Terms.

5) **Scope of License; Limitations and Obligations.** All Works and all rights therein, including copyright rights, remain the sole and exclusive property of the Rightsholder. The License provides only those rights expressly set forth in the terms and conveys no other rights in any Works

6) **General Payment Terms.** User may pay at time of checkout by credit card or choose to be invoiced. If the User chooses to be invoiced, the User shall: (i) remit payments in the manner identified on specific invoices, (ii) unless otherwise specifically stated in an Order Confirmation or separate written agreement, Users shall remit payments upon receipt of the relevant invoice from CCC, either by delivery or notification of availability of the invoice via the Marketplace platform, and (iii) if the User does not pay the invoice within 30 days of receipt, the User may incur a service charge of 1.5% per month or the maximum rate allowed by applicable law, whichever is less. While User may exercise the rights in the License immediately upon receiving the Order Confirmation, the License is automatically revoked and is null and void, as if it had never been issued, if CCC does not receive complete payment on a timely basis.

7) **General Limits on Use.** Unless otherwise provided in the Order Confirmation, any grant of rights to User (i) involves only the rights set forth in the Terms and does not include subsequent or additional uses, (ii) is non-exclusive and non-transferable, and (iii) is subject to any and all limitations and restrictions (such as, but not limited to, limitations on duration of use or circulation) included in the Terms. Upon completion of the licensed use as set forth in the Order Confirmation, User shall either secure a new permission for further use of the Work(s) or immediately cease any new use of the Work(s) and shall render inaccessible (such as by deleting or by removing or severing links or other locators) any further copies of the Work. User may only make alterations to the Work if and as expressly set forth in the Order Confirmation. No Work may be used in any way that is defamatory, violates the rights of third parties (including such third parties' rights of copyright, privacy, publicity, or other tangible or intangible property), or is otherwise illegal, sexually explicit, or obscene. In addition, User may not conjoin a Work with any other material that may result in damage to the reputation of the Rightsholder. User agrees to inform CCC if it becomes aware of any infringement of any rights in a Work and to cooperate with any reasonable request of CCC or the Rightsholder in connection therewith.

8) **Third Party Materials.** In the event that the material for which a License is sought includes third party materials (such as photographs, illustrations, graphs, inserts and similar materials) that are identified in such material as having been used by permission (or a similar indicator), User is responsible for identifying, and seeking separate licenses (under this Service, if available, or otherwise) for any of such third party materials; without a separate license, User may not use such third party materials via the License.

9) **Copyright Notice.** Use of proper copyright notice for a Work is required as a condition of any License granted under the Service. Unless otherwise provided in the Order Confirmation, a proper copyright notice will read substantially as follows: "Used with permission of [Rightsholder's name], from [Work's title, author, volume, edition number and year of copyright]; permission conveyed through Copyright Clearance Center, Inc." Such notice must be provided in a reasonably legible font size and must be placed either on a cover page or in another location that any person, upon gaining access to the material which is the subject of a permission, shall see, or in the case of republication Licenses, immediately adjacent to the Work as used (for example, as part of a by-line or footnote) or in the place where substantially all other credits or notices for the new work containing the republished Work are located. Failure to include the required notice results in loss to the Rightsholder and CCC, and the User shall be liable to pay liquidated damages for each such failure equal to twice the use fee specified in the Order Confirmation, in addition to the use fee itself and any other fees and charges specified.

10) **Indemnity.** User hereby indemnifies and agrees to defend the Rightsholder and CCC, and their respective employees and directors, against all claims, liability, damages, costs, and expenses, including legal fees and expenses, arising out of any use of a Work beyond the scope of the rights granted herein and in the Order Confirmation, or any use of a Work which has been altered in any unauthorized way by User, including claims of defamation or infringement of rights of copyright, publicity, privacy, or other tangible or intangible property.

11) **Limitation of Liability.** UNDER NO CIRCUMSTANCES WILL CCC OR THE RIGHTSHOLDER BE LIABLE FOR ANY DIRECT, INDIRECT, CONSEQUENTIAL, OR INCIDENTAL DAMAGES (INCLUDING WITHOUT LIMITATION DAMAGES FOR LOSS OF BUSINESS PROFITS OR INFORMATION, OR FOR BUSINESS INTERRUPTION) ARISING OUT OF THE USE OR INABILITY TO USE A WORK, EVEN IF ONE OR BOTH OF THEM HAS BEEN ADVISED OF THE POSSIBILITY OF SUCH DAMAGES. In any event, the total liability of the Rightsholder and CCC (including their respective employees and directors) shall not exceed the total amount actually paid by User for the relevant License. User assumes full liability for the actions and omissions of its principals, employees, agents, affiliates, successors, and assigns.

12) **Limited Warranties.** THE WORK(S) AND RIGHT(S) ARE PROVIDED "AS IS." CCC HAS THE RIGHT TO GRANT TO USER THE RIGHTS GRANTED IN THE ORDER CONFIRMATION DOCUMENT. CCC AND THE RIGHTSHOLDER DISCLAIM ALL OTHER WARRANTIES RELATING TO THE WORK(S) AND RIGHT(S), EITHER EXPRESS OR IMPLIED, INCLUDING WITHOUT LIMITATION IMPLIED WARRANTIES OF MERCHANTABILITY OR FITNESS FOR A PARTICULAR PURPOSE. ADDITIONAL RIGHTS MAY BE REQUIRED TO USE ILLUSTRATIONS, GRAPHS, PHOTOGRAPHS, ABSTRACTS, INSERTS, OR OTHER PORTIONS OF THE WORK (AS OPPOSED TO THE ENTIRE WORK) IN A MANNER CONTEMPLATED BY USER; USER UNDERSTANDS AND AGREES THAT NEITHER CCC NOR THE RIGHTSHOLDER MAY HAVE SUCH ADDITIONAL RIGHTS TO GRANT.

13) **Effect of Breach.** Any failure by User to pay any amount when due, or any use by User of a Work beyond the scope of the License set forth in the Order Confirmation and/or the Terms, shall be a material breach of such License. Any breach not cured within 10 days of written notice thereof shall result in immediate termination of such License without further notice. Any unauthorized (but licensable) use of a Work that is terminated immediately upon notice thereof may be liquidated by payment of the Rightsholder's ordinary license price therefor; any unauthorized (and unlicensable) use that is not terminated immediately for any reason (including, for example, because materials containing the Work cannot reasonably be recalled) will be subject to all remedies available at law or in equity, but in no event to a payment of less than three times the Rightsholder's ordinary license price for the most closely analogous licensable use plus Rightsholder's and/or CCC's costs and expenses incurred in collecting such payment.

14) **Additional Terms for Specific Products and Services.** If a User is making one of the uses described in this Section 14, the additional terms and conditions apply:

a) ***Print Uses of Academic Course Content and Materials (photocopies for academic coursepacks or classroom handouts).*** For photocopies for academic coursepacks or classroom handouts the following additional terms apply:

i) The copies and anthologies created under this License may be made and assembled by faculty members individually or at their request by on-campus bookstores or copy centers, or by off-campus copy shops and other similar entities.

ii) No License granted shall in any way: (i) include any right by User to create a substantively non-identical copy of the Work or to edit or in any other way modify the Work (except by means of deleting material immediately preceding or following the entire portion of the Work copied) (ii) permit "publishing ventures" where any particular anthology would be systematically marketed at multiple institutions.

iii) Subject to any Publisher Terms (and notwithstanding any apparent contradiction in the Order Confirmation arising from data provided by User), any use authorized under the academic pay-per-use service is limited as follows:

A) any License granted shall apply to only one class (bearing a unique identifier as assigned by the institution, and thereby including all sections or other subparts of the class) at one institution;

B) use is limited to not more than 25% of the text of a book or of the items in a published collection of essays, poems or articles;

D) no User may sell or distribute any particular anthology, whether photocopied or electronic, at more than one institution of learning;

E) in the case of a photocopy permission, no materials may be entered into electronic memory by User except in order to produce an identical copy of a Work before or during the academic term (or analogous period) as to which any particular permission is granted. In the event that User shall choose to retain materials that are the subject of a photocopy permission in electronic memory for purposes of producing identical copies more than one day after such retention (but still within the scope of any permission granted), User must notify CCC of such fact in the applicable permission request and such retention shall constitute one copy actually sold for purposes of calculating permission fees due; and

F) any permission granted shall expire at the end of the class. No permission granted shall in any way include any right by User to create a substantively non-identical copy of the Work or to edit or in any other way modify the Work (except by means of deleting material immediately preceding or following the entire portion of the Work copied).

iv) Books and Records; Right to Audit. As to each permission granted under the academic pay-per-use Service, User shall maintain for at least four full calendar years books and records sufficient for CCC to determine the numbers of copies made by User under such permission. CCC and any representatives it may designate shall have the right to audit such books and records at any time during User's ordinary business hours, upon two days' prior notice. If any such audit shall determine that User shall have underpaid for, or underreported, any photocopies sold or by three percent (3%) or more, then User shall bear all the costs of any such audit; otherwise, CCC shall bear the costs of any such audit. Any amount determined by such audit to have been underpaid by User shall immediately be paid to CCC by User, together with interest thereon at the rate of 10% per annum from the date such amount was originally due. The provisions of this paragraph shall survive the termination of this License for any reason.

b) ***Digital Pay-Per-Uses of Academic Course Content and Materials (e-coursepacks, electronic reserves, learning management systems, academic institution intranets).*** For uses in e-coursepacks, posts in electronic reserves, posts in learning management systems, or posts on academic institution intranets, the following additional terms apply:

i) The pay-per-uses subject to this Section 14(b) include:

A) **Posting e-reserves, course management systems, e-coursepacks for text-based content,** which grants authorizations to import requested material in electronic format, and allows electronic access to this material to members of a designated college or university class, under the direction of an instructor designated by the college or university, accessible only under appropriate electronic controls (e.g., password);

B) **Posting e-reserves, course management systems, e-coursepacks for material consisting of photographs or other still images not embedded in text,** which grants not only the authorizations described in Section 14(b)(i)(A) above, but also the following authorization: to include the requested material in course materials for use consistent with Section 14(b)(i)(A) above, including any necessary resizing, reformatting or modification of the resolution of such requested material (provided that such modification does not alter the underlying editorial content or meaning of the requested material, and provided that the resulting modified content is used solely within the scope of, and in a manner consistent with, the particular authorization described in the Order Confirmation and the Terms), but not including any other form of manipulation, alteration or editing of the requested material;

C) **Posting e-reserves, course management systems, e-coursepacks or other academic distribution for audiovisual content,** which grants not only the authorizations described in Section 14(b)(i)(A) above, but also the following authorizations: (i) to include the requested material in course materials for use consistent with Section 14(b)(i)(A) above; (ii) to display and perform the requested material to such members of such class in the physical classroom or remotely by means of streaming media or other video formats; and (iii) to "clip" or reformat the requested material for purposes of time or content management or ease of delivery, provided that such "clipping" or reformatting does not alter the underlying editorial content or meaning of the requested material and that the resulting material is used solely within the scope of, and in a manner consistent with, the particular authorization described in the Order Confirmation and the Terms. Unless expressly set forth in the relevant Order Conformation, the License does not authorize any other form of manipulation, alteration or editing of the requested material.

ii) Unless expressly set forth in the relevant Order Confirmation, no License granted shall in any way: (i) include any right by User to create a substantively non-identical copy of the Work or to edit or in any other way modify the Work (except by means of deleting material immediately preceding or following the entire portion of the Work copied or, in the case of Works subject to Sections 14(b)(1)(B) or (C) above, as described in such Sections) (ii) permit "publishing ventures" where any particular course materials would be systematically marketed at multiple institutions.

iii) Subject to any further limitations determined in the Rightsholder Terms (and notwithstanding any apparent contradiction in the Order Confirmation arising from data provided by User), any use authorized under the electronic course content pay-per-use service is limited as follows:

A) any License granted shall apply to only one class (bearing a unique identifier as assigned by the institution, and thereby including all sections or other subparts of the class) at one institution;

B) use is limited to not more than 25% of the text of a book or of the items in a published collection of essays, poems or articles;

C) use is limited to not more than the greater of (a) 25% of the text of an issue of a journal or other periodical or (b) two articles from such an issue;

D) no User may sell or distribute any particular materials, whether photocopied or electronic, at more than one institution of learning;

E) electronic access to material which is the subject of an electronic-use permission must be limited by means of electronic password, student identification or other control permitting access solely to students and instructors in the class;

F) User must ensure (through use of an electronic cover page or other appropriate means) that any person, upon gaining electronic access to the material, which is the subject of a permission, shall see:

- a proper copyright notice, identifying the Rightsholder in whose name CCC has granted permission,
- a statement to the effect that such copy was made pursuant to permission,
- a statement identifying the class to which the material applies and notifying the reader that the material has been made available electronically solely for use in the class, and
- a statement to the effect that the material may not be further distributed to any person outside the class, whether by copying or by transmission and whether electronically or in paper form, and User must also ensure that such cover page or other means will print out in the event that the person accessing the material chooses to print out the material or any part thereof.

G) any permission granted shall expire at the end of the class and, absent some other form of authorization, User is thereupon required to delete the applicable material from any electronic storage or to block electronic access to the applicable material.

iv) Uses of separate portions of a Work, even if they are to be included in the same course material or the same university or college class, require separate permissions under the electronic course content pay-per-use Service. Unless otherwise provided in the Order Confirmation, any grant of rights to User is limited to use completed no later than the end of the academic term (or analogous period) as to which any particular permission is granted.

v) Books and Records; Right to Audit. As to each permission granted under the electronic course content Service, User shall maintain for at least four full calendar years books and records sufficient for CCC to determine the numbers of copies made by User under such permission. CCC and any representatives it may designate shall have the right to audit such books and records at any time during User's ordinary business hours, upon two days' prior notice. If any such audit shall determine that User shall have underpaid for, or underreported, any electronic copies used by three percent (3%) or more, then User shall bear all the costs of any such audit; otherwise, CCC shall bear the costs of any such audit. Any amount determined by such audit to have been underpaid by User shall immediately be paid to CCC by User, together with interest thereon at the rate of 10% per annum from the date such amount was originally due. The provisions of this paragraph shall survive the termination of this license for any reason.

c) ***Pay-Per-Use Permissions for Certain Reproductions (Academic photocopies for library reserves and interlibrary loan reporting) (Non-academic internal/external business uses and commercial document delivery).*** The License expressly excludes the uses listed in Section (c)(i)-(v) below (which must be subject to separate license from the applicable Rightsholder) for: academic photocopies for library reserves and interlibrary loan reporting; and non-academic internal/external business uses and commercial document delivery.

i) electronic storage of any reproduction (whether in plain-text, PDF, or any other format) other than on a transitory basis;

ii) the input of Works or reproductions thereof into any computerized database;

iii) reproduction of an entire Work (cover-to-cover copying) except where the Work is a single article;

iv) reproduction for resale to anyone other than a specific customer of User;

v) republication in any different form. Please obtain authorizations for these uses through other CCC services or directly from the rightsholder.

Any license granted is further limited as set forth in any restrictions included in the Order Confirmation and/or in these Terms.

d) ***Electronic Reproductions in Online Environments (Non-Academic-email, intranet, internet and extranet).*** For "electronic reproductions", which generally includes e-mail use (including instant messaging or other electronic transmission to a defined group of recipients) or posting on an intranet, extranet or Intranet site (including any display or performance incidental thereto), the following additional terms apply:

i) Unless otherwise set forth in the Order Confirmation, the License is limited to use completed within 30 days for any use on the Internet, 60 days for any use on an intranet or extranet and one year for any other use, all as measured from the "republication date" as identified in the Order Confirmation, if any, and otherwise from the date of the Order Confirmation.

ii) User may not make or permit any alterations to the Work, unless expressly set forth in the Order Confirmation (after request by User and approval by Rightsholder); provided, however, that a Work consisting of photographs or other still images not embedded in text may, if necessary, be resized, reformatted or have its resolution modified without additional express permission, and a Work consisting of audiovisual content may, if necessary, be "clipped" or reformatted for purposes of time or content management or ease of delivery (provided that any such resizing, reformatting, resolution modification or "clipping" does not alter the underlying editorial content or meaning of the Work used, and that the resulting material is used solely within the scope of, and in a manner consistent with, the particular License described in the Order Confirmation and the Terms.

15) **Miscellaneous.**

a) User acknowledges that CCC may, from time to time, make changes or additions to the Service or to the Terms, and that Rightsholder may make changes or additions to the Rightsholder Terms. Such updated Terms will replace the prior terms and conditions in the order workflow and shall be effective as to any subsequent Licenses but shall not apply to Licenses already granted and paid for under a prior set of terms.

b) Use of User-related information collected through the Service is governed by CCC's privacy policy, available online at www.copyright.com/about/privacy-policy/.

c) The License is personal to User. Therefore, User may not assign or transfer to any other person (whether a natural person or an organization of any kind) the License or any rights granted thereunder; provided, however, that, where applicable, User may assign such License in its entirety on written notice to CCC in the event of a transfer of all or substantially all of User's rights in any new material which includes the Work(s) licensed under this Service.

d) No amendment or waiver of any Terms is binding unless set forth in writing and signed by the appropriate parties, including, where applicable, the Rightsholder. The Rightsholder and CCC hereby object to any terms contained in any writing prepared by or on behalf of the User or its principals, employees, agents or affiliates and purporting to govern or otherwise relate to the License described in the Order Confirmation, which terms are in any way inconsistent with any Terms set forth in the Order Confirmation, and/or in CCC's standard operating procedures, whether such writing is prepared prior to, simultaneously with or subsequent to the Order Confirmation, and whether such writing appears on a copy of the Order Confirmation or in a separate instrument.

e) The License described in the Order Confirmation shall be governed by and construed under the law of the State of New York, USA, without regard to the principles thereof of conflicts of law. Any case, controversy, suit, action, or proceeding arising out of, in connection with, or related to such License shall be brought, at CCC's sole discretion, in any federal or state court located in the County of New York, State of New York, USA, or in any federal or state court whose geographical jurisdiction covers the location of the Rightsholder set forth in the Order Confirmation. The parties expressly submit to the personal jurisdiction and venue of each such federal or state court.

Fig 2.6

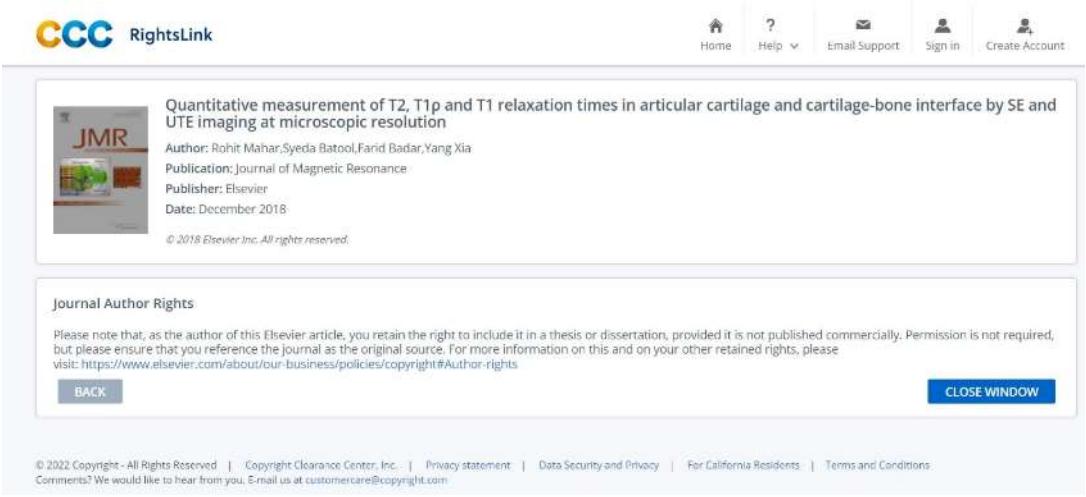
CCC RightsLink
Home
Help
Email Support
Sign in
Create Account
JMR
Quantitative measurement of T2, T1ρ and T1 relaxation times in articular cartilage and cartilage-bone interface by SE and UTE imaging at microscopic resolution
Author: Rohit Mahar,Syeda Batool,Farid Badar,Yang Xia
Publication: Journal of Magnetic Resonance
Publisher: Elsevier
Date: December 2018
© 2018 Elsevier Inc. All rights reserved.
Journal Author Rights
Please note that, as the author of this Elsevier article, you retain the right to include it in a thesis or dissertation, provided it is not published commercially. Permission is not required, but please ensure that you reference the journal as the original source. For more information on this and on your other retained rights, please visit: https://www.elsevier.com/about/our-business/policies/copyright#Author-rights
BACK
CLOSE WINDOW
© 2022 Copyright - All Rights Reserved | Copyright Clearance Center, Inc. | Privacy statement | Data Security and Privacy | For California Residents | Terms and Conditions
Comments? We would like to hear from you. E-mail us at customercare@copyright.com

Fig 2.7

Creative Commons Attribution-NonCommercial 4.0 International Public License

By exercising the Licensed Rights (defined below), You accept and agree to be bound by the terms and conditions of this Creative Commons Attribution-NonCommercial 4.0 International Public License ("Public License"). To the extent this Public License may be interpreted as a contract, you are granted the Licensed Rights in consideration of Your acceptance of these terms and conditions, and the Licensor grants You such rights in consideration of benefits the Licensor receives from making the Licensed Material available under these terms and conditions.

Section 1 – Definitions.

a. **Adapted Material** means material subject to Copyright and Similar Rights that is derived from or based upon the Licensed Material and in which the Licensed Material is translated, altered, arranged, transformed, or otherwise modified in a manner requiring permission under the Copyright and Similar Rights held by the Licensor. For purposes of this Public License, where the Licensed Material is a musical work, performance, or sound recording, Adapted Material is always produced where the Licensed Material is synched in timed relation with a moving image.

b. **Adapter's License** means the license You apply to Your Copyright and Similar Rights in Your contributions to Adapted Material in accordance with the terms and conditions of this Public License.

c. **Copyright and Similar Rights** means copyright and/or similar rights closely related to copyright including, without limitation, performance, broadcast, sound recording, and Sui Generis Database Rights, without regard to how the rights are labeled or categorized. For purposes of this Public License, the rights specified in Section 2(b)(1)-(2) are not Copyright and Similar Rights.

d. **Effective Technological Measures** means those measures that, in the absence of proper authority, may not be circumvented under laws fulfilling obligations under Article 11 of the WIPO Copyright Treaty adopted on December 20, 1996, and/or similar international agreements.

e. **Exceptions and Limitations** means fair use, fair dealing, and/or any other exception or limitation to Copyright and Similar Rights that applies to Your use of the Licensed Material.

f. **Licensed Material** means the artistic or literary work, database, or other material to which the Licensor applied this Public License.

g. **Licensed Rights** means the rights granted to You subject to the terms and conditions of this Public License, which are limited to all Copyright and Similar Rights that apply to Your use of the Licensed Material and that the Licensor has authority to license.

h. **Licensor** means the individual(s) or entity(ies) granting rights under this Public License.

i. **NonCommercial** means not primarily intended for or directed towards commercial advantage or monetary compensation. For purposes of this Public License, the exchange of the Licensed Material for other material subject to Copyright and Similar Rights by digital file-sharing or similar means is NonCommercial provided there is no payment of monetary compensation in connection with the exchange.

j. **Share** means to provide material to the public by any means or process that requires permission under the Licensed Rights, such as reproduction, public display, public performance, distribution, dissemination, communication, or importation, and to make material available to the public including in ways that members of the public may access the material from a place and at a time individually chosen by them.

k. **Sui Generis Database Rights** means rights other than copyright resulting from Directive 96/9/EC of the European Parliament and of the Council of 11 March 1996 on the legal protection of databases, as amended and/or succeeded, as well as other essentially equivalent rights anywhere in the world.

l. **You** means the individual or entity exercising the Licensed Rights under this Public License. **Your** has a corresponding meaning.

Section 2 – Scope.

a. **License grant**.

1. Subject to the terms and conditions of this Public License, the Licensor hereby grants You a worldwide, royalty-free, non-sublicensable, non-exclusive, irrevocable license to exercise the Licensed Rights in the Licensed Material to:

A. reproduce and Share the Licensed Material, in whole or in part, for NonCommercial purposes only; and

B. produce, reproduce, and Share Adapted Material for NonCommercial purposes only.

2. Exceptions and Limitations. For the avoidance of doubt, where Exceptions and Limitations apply to Your use, this Public License does not apply, and You do not need to comply with its terms and conditions.

3. Term. The term of this Public License is specified in Section 6(a).

4. Media and formats; technical modifications allowed. The Licensor authorizes You to exercise the Licensed Rights in all media and formats whether now known or hereafter created, and to make technical modifications necessary to do so. The Licensor waives and/or agrees not to assert any right or authority to forbid You from making technical modifications necessary to exercise the Licensed Rights, including technical modifications necessary to circumvent Effective Technological Measures. For purposes of this Public License, simply making modifications authorized by this Section 2(a)(4) never produces Adapted Material.

5. Downstream recipients.

A. Offer from the Licensor – Licensed Material. Every recipient of the Licensed Material automatically receives an offer from the Licensor to exercise the Licensed Rights under the terms and conditions of this Public License.

B. No downstream restrictions. You may not offer or impose any additional or different terms or conditions on, or apply any Effective Technological Measures to, the Licensed Material if doing so restricts exercise of the Licensed Rights by any recipient of the Licensed Material.

6. No endorsement. Nothing in this Public License constitutes or may be construed as permission to assert or imply that You are, or that Your use of the Licensed Material is, connected with, or sponsored, endorsed, or granted official status by, the Licensor or others designated to receive attribution as provided in Section 3(a)(1)(A)(i).

b. **Other rights**.

1. Moral rights, such as the right of integrity, are not licensed under this Public License, nor are publicity, privacy, and/or other similar

personality rights; however, to the extent possible, the Licensor waives and/or agrees not to assert any such rights held by the Licensor to the limited extent necessary to allow You to exercise the Licensed Rights, but not otherwise.

2. Patent and trademark rights are not licensed under this Public License.
3. To the extent possible, the Licensor waives any right to collect royalties from You for the exercise of the Licensed Rights, whether directly or through a collecting society under any voluntary or waivable statutory or compulsory licensing scheme. In all other cases the Licensor expressly reserves any right to collect such royalties, including when the Licensed Material is used other than for NonCommercial purposes.

Section 3 – License Conditions.

Your exercise of the Licensed Rights is expressly made subject to the following conditions.

a. **Attribution**.

1. If You Share the Licensed Material (including in modified form), You must:

A. retain the following if it is supplied by the Licensor with the Licensed Material:

i. identification of the creator(s) of the Licensed Material and any others designated to receive attribution, in any reasonable manner requested by the Licensor (including by pseudonym if designated);

ii. a copyright notice;

iii. a notice that refers to this Public License;

iv. a notice that refers to the disclaimer of warranties;

v. a URI or hyperlink to the Licensed Material to the extent reasonably practicable;

B. indicate if You modified the Licensed Material and retain an indication of any previous modifications; and

C. indicate the Licensed Material is licensed under this Public License, and include the text of, or the URI or hyperlink to, this Public License.

2. You may satisfy the conditions in Section 3(a)(1) in any reasonable manner based on the medium, means, and context in which You Share the Licensed Material. For example, it may be reasonable to satisfy the conditions by providing a URI or hyperlink to a resource that includes the required information.
3. If requested by the Licensor, You must remove any of the information required by Section 3(a)(1)(A) to the extent reasonably practicable.
4. If You Share Adapted Material You produce, the Adapter's License You apply must not prevent recipients of the Adapted Material from complying with this Public License.

Section 4 – Sui Generis Database Rights.

Where the Licensed Rights include Sui Generis Database Rights that apply to Your use of the Licensed Material:

a. for the avoidance of doubt, Section 2(a)(1) grants You the right to extract, reuse, reproduce, and Share all or a substantial portion of the contents of the database for NonCommercial purposes only;
b. if You include all or a substantial portion of the database contents in a database in which You have Sui Generis Database Rights, then the database in which You have Sui Generis Database Rights (but not its individual contents) is Adapted Material; and
c. You must comply with the conditions in Section 3(a) if You Share all or a substantial portion of the contents of the database.

For the avoidance of doubt, this Section 4 supplements and does not replace Your obligations under this Public License where the Licensed Rights include other Copyright and Similar Rights.

Section 5 – Disclaimer of Warranties and Limitation of Liability.

a. Unless otherwise separately undertaken by the Licensor, to the extent possible, the Licensor offers the Licensed Material as-is and as-available, and makes no representations or warranties of any kind concerning the Licensed Material, whether express, implied, statutory, or other. This includes, without limitation, warranties of title,

merchantability, fitness for a particular purpose, non-infringement, absence of latent or other defects, accuracy, or the presence or absence of errors, whether or not known or discoverable. Where disclaimers of warranties are not allowed in full or in part, this disclaimer may not apply to You.

b. To the extent possible, in no event will the Licensor be liable to You on any legal theory (including, without limitation, negligence) or otherwise for any direct, special, indirect, incidental, consequential, punitive, exemplary, or other losses, costs, expenses, or damages arising out of this Public License or use of the Licensed Material, even if the Licensor has been advised of the possibility of such losses, costs, expenses, or damages. Where a limitation of liability is not allowed in full or in part, this limitation may not apply to You.

c. The disclaimer of warranties and limitation of liability provided above shall be interpreted in a manner that, to the extent possible, most closely approximates an absolute disclaimer and waiver of all liability.

Section 6 – Term and Termination.

a. This Public License applies for the term of the Copyright and Similar Rights licensed here. However, if You fail to comply with this Public License, then Your rights under this Public License terminate automatically.

b. Where Your right to use the Licensed Material has terminated under Section 6(a), it reinstates:

1. automatically as of the date the violation is cured, provided it is cured within 30 days of Your discovery of the violation; or
2. upon express reinstatement by the Licensor.

For the avoidance of doubt, this Section 6(b) does not affect any right the Licensor may have to seek remedies for Your violations of this Public License.

c. For the avoidance of doubt, the Licensor may also offer the Licensed Material under separate terms or conditions or stop distributing the Licensed Material at any time; however, doing so will not terminate this Public License.

d. Sections 1, 5, 6, 7, and 8 survive termination of this Public License.

Section 7 – Other Terms and Conditions.

a. The Licensor shall not be bound by any additional or different terms or conditions communicated by You unless expressly agreed.

b. Any arrangements, understandings, or agreements regarding the Licensed Material not stated herein are separate from and independent of the terms and conditions of this Public License.

Section 8 – Interpretation.

a. For the avoidance of doubt, this Public License does not, and shall not be interpreted to, reduce, limit, restrict, or impose conditions on any use of the Licensed Material that could lawfully be made without permission under this Public License.

b. To the extent possible, if any provision of this Public License is deemed unenforceable, it shall be automatically reformed to the minimum extent necessary to make it enforceable. If the provision cannot be reformed, it shall be severed from this Public License without affecting the enforceability of the remaining terms and conditions.

c. No term or condition of this Public License will be waived and no failure to comply consented to unless expressly agreed to by the Licensor.

d. Nothing in this Public License constitutes or may be interpreted as a limitation upon, or waiver of, any privileges and immunities that apply to the Licensor or You, including from the legal processes of any jurisdiction or authority.

Permission to reproduce Chapter 3 in its entirety.

JOHN WILEY AND SONS LICENSE
TERMS AND CONDITIONS

Aug 10, 2022

This Agreement between Syeda Batool ("You") and John Wiley and Sons ("John Wiley and Sons") consists of your license details and the terms and conditions provided by John Wiley and Sons and Copyright Clearance Center.

License Number	5365610852261
License date	Aug 10, 2022
Licensed Content Publisher	John Wiley and Sons
Licensed Content Publication	Journal of Orthopaedic Research
Licensed Content Title	Quantitative μMRI and PLM study of rabbit humeral and femoral head cartilage at sub-10 μm resolutions
Licensed Content Author	Yang Xia, Austin Tetmeyer, Farid Badar, et al
Licensed Content Date	Dec 12, 2019
Licensed Content Volume	38
Licensed Content Issue	5
Licensed Content Pages	11
Type of use	Dissertation/Thesis
Requestor type	Author of this Wiley article
Format	Print and electronic
Portion	Full article

Will you be translating?	No
Title	Quantitative μMRI and PLM study of rabbit humeral and femoral head cartilage at sub-10 μm resolutions
Institution name	Oakland University
Expected presentation date	Oct 2022
Requestor Location	Syeda Batool 244 Meadow Brook Road Room #165 Hannah Hall ROCHESTER, MI 48309 United States Attn: Syeda Batool
Publisher Tax ID	EU826007151
Total	0.00 USD

Terms and Conditions

TERMS AND CONDITIONS

This copyrighted material is owned by or exclusively licensed to John Wiley & Sons, Inc. or one of its group companies (each a"Wiley Company") or handled on behalf of a society with which a Wiley Company has exclusive publishing rights in relation to a particular work (collectively "WILEY"). By clicking "accept" in connection with completing this licensing transaction, you agree that the following terms and conditions apply to this transaction (along with the billing and payment terms and conditions established by the Copyright Clearance Center Inc., ("CCC's Billing and Payment terms and conditions"), at the time that you opened your RightsLink account (these are available at any time at http://myaccount.copyright.com).

Terms and Conditions

- The materials you have requested permission to reproduce or reuse (the "Wiley Materials") are protected by copyright.
- You are hereby granted a personal, non-exclusive, non-sub licensable (on a stand-alone basis), non-transferable, worldwide, limited license to reproduce the Wiley Materials for the purpose specified in the licensing process. This license, **and any CONTENT (PDF or image file) purchased as part of your order,** is for a one-time use only and limited to any maximum distribution number specified in the

license. The first instance of republication or reuse granted by this license must be completed within two years of the date of the grant of this license (although copies prepared before the end date may be distributed thereafter). The Wiley Materials shall not be used in any other manner or for any other purpose, beyond what is granted in the license. Permission is granted subject to an appropriate acknowledgement given to the author, title of the material/book/journal and the publisher. You shall also duplicate the copyright notice that appears in the Wiley publication in your use of the Wiley Material. Permission is also granted on the understanding that nowhere in the text is a previously published source acknowledged for all or part of this Wiley Material. Any third-party content is expressly excluded from this permission.

- With respect to the Wiley Materials, all rights are reserved. Except as expressly granted by the terms of the license, no part of the Wiley Materials may be copied, modified, adapted (except for minor reformatting required by the new Publication), translated, reproduced, transferred or distributed, in any form or by any means, and no derivative works may be made based on the Wiley Materials without the prior permission of the respective copyright owner.**For STM Signatory Publishers clearing permission under the terms of the STM Permissions Guidelines only, the terms of the license are extended to include subsequent editions and for editions in other languages, provided such editions are for the work as a whole in situ and does not involve the separate exploitation of the permitted figures or extracts,** You may not alter, remove or suppress in any manner any copyright, trademark or other notices displayed by the Wiley Materials. You may not license, rent, sell, loan, lease, pledge, offer as security, transfer or assign the Wiley Materials on a stand-alone basis, or any of the rights granted to you hereunder to any other person.

- The Wiley Materials and all of the intellectual property rights therein shall at all times remain the exclusive property of John Wiley & Sons Inc, the Wiley Companies, or their respective licensors, and your interest therein is only that of having possession of and the right to reproduce the Wiley Materials pursuant to Section 2 herein during the continuance of this Agreement. You agree that you own no right, title or interest in or to the Wiley Materials or any of the intellectual property rights therein. You shall have no rights hereunder other than the license as provided for above in Section 2. No right, license or interest to any trademark, trade name, service mark or other branding ("Marks") of WILEY or its licensors is granted hereunder, and you agree that you shall not assert any such right, license or interest with respect thereto

- NEITHER WILEY NOR ITS LICENSORS MAKES ANY WARRANTY OR REPRESENTATION OF ANY KIND TO YOU OR ANY THIRD PARTY, EXPRESS, IMPLIED OR STATUTORY, WITH RESPECT TO THE

MATERIALS OR THE ACCURACY OF ANY INFORMATION CONTAINED IN THE MATERIALS, INCLUDING, WITHOUT LIMITATION, ANY IMPLIED WARRANTY OF MERCHANTABILITY, ACCURACY, SATISFACTORY QUALITY, FITNESS FOR A PARTICULAR PURPOSE, USABILITY, INTEGRATION OR NON-INFRINGEMENT AND ALL SUCH WARRANTIES ARE HEREBY EXCLUDED BY WILEY AND ITS LICENSORS AND WAIVED BY YOU.

- WILEY shall have the right to terminate this Agreement immediately upon breach of this Agreement by you.
- You shall indemnify, defend and hold harmless WILEY, its Licensors and their respective directors, officers, agents and employees, from and against any actual or threatened claims, demands, causes of action or proceedings arising from any breach of this Agreement by you.
- IN NO EVENT SHALL WILEY OR ITS LICENSORS BE LIABLE TO YOU OR ANY OTHER PARTY OR ANY OTHER PERSON OR ENTITY FOR ANY SPECIAL, CONSEQUENTIAL, INCIDENTAL, INDIRECT, EXEMPLARY OR PUNITIVE DAMAGES, HOWEVER CAUSED, ARISING OUT OF OR IN CONNECTION WITH THE DOWNLOADING, PROVISIONING, VIEWING OR USE OF THE MATERIALS REGARDLESS OF THE FORM OF ACTION, WHETHER FOR BREACH OF CONTRACT, BREACH OF WARRANTY, TORT, NEGLIGENCE, INFRINGEMENT OR OTHERWISE (INCLUDING, WITHOUT LIMITATION, DAMAGES BASED ON LOSS OF PROFITS, DATA, FILES, USE, BUSINESS OPPORTUNITY OR CLAIMS OF THIRD PARTIES), AND WHETHER OR NOT THE PARTY HAS BEEN ADVISED OF THE POSSIBILITY OF SUCH DAMAGES. THIS LIMITATION SHALL APPLY NOTWITHSTANDING ANY FAILURE OF ESSENTIAL PURPOSE OF ANY LIMITED REMEDY PROVIDED HEREIN.
- Should any provision of this Agreement be held by a court of competent jurisdiction to be illegal, invalid, or unenforceable, that provision shall be deemed amended to achieve as nearly as possible the same economic effect as the original provision, and the legality, validity and enforceability of the remaining provisions of this Agreement shall not be affected or impaired thereby.
- The failure of either party to enforce any term or condition of this Agreement shall not constitute a waiver of either party's right to enforce each and every term and condition of this Agreement. No breach under this agreement shall be deemed waived or excused by either party unless such waiver or consent is in writing signed by the party granting such waiver or consent. The waiver by or consent of a party to

a breach of any provision of this Agreement shall not operate or be construed as a waiver of or consent to any other or subsequent breach by such other party.

- This Agreement may not be assigned (including by operation of law or otherwise) by you without WILEY's prior written consent.
- Any fee required for this permission shall be non-refundable after thirty (30) days from receipt by the CCC.
- These terms and conditions together with CCC's Billing and Payment terms and conditions (which are incorporated herein) form the entire agreement between you and WILEY concerning this licensing transaction and (in the absence of fraud) supersedes all prior agreements and representations of the parties, oral or written. This Agreement may not be amended except in writing signed by both parties. This Agreement shall be binding upon and inure to the benefit of the parties' successors, legal representatives, and authorized assigns.
- In the event of any conflict between your obligations established by these terms and conditions and those established by CCC's Billing and Payment terms and conditions, these terms and conditions shall prevail.
- WILEY expressly reserves all rights not specifically granted in the combination of (i) the license details provided by you and accepted in the course of this licensing transaction, (ii) these terms and conditions and (iii) CCC's Billing and Payment terms and conditions.
- This Agreement will be void if the Type of Use, Format, Circulation, or Requestor Type was misrepresented during the licensing process.
- This Agreement shall be governed by and construed in accordance with the laws of the State of New York, USA, without regards to such state's conflict of law rules. Any legal action, suit or proceeding arising out of or relating to these Terms and Conditions or the breach thereof shall be instituted in a court of competent jurisdiction in New York County in the State of New York in the United States of America and each party hereby consents and submits to the personal jurisdiction of such court, waives any objection to venue in such court and consents to service of process by registered or certified mail, return receipt requested, at the last known address of such party.

WILEY OPEN ACCESS TERMS AND CONDITIONS

Wiley Publishes Open Access Articles in fully Open Access Journals and in Subscription journals offering Online Open. Although most of the fully Open Access journals publish open access articles under the terms of the Creative Commons Attribution (CC BY)

License only, the subscription journals and a few of the Open Access Journals offer a choice of Creative Commons Licenses. The license type is clearly identified on the article.

The Creative Commons Attribution License

The Creative Commons Attribution License (CC-BY) allows users to copy, distribute and transmit an article, adapt the article and make commercial use of the article. The CC-BY license permits commercial and non-.

Creative Commons Attribution Non-Commercial License

The Creative Commons Attribution Non-Commercial (CC-BY-NC)License permits use, distribution and reproduction in any medium, provided the original work is properly cited and is not used for commercial purposes.(see below)

Creative Commons Attribution-Non-Commercial-NoDerivs License

The Creative Commons Attribution Non-Commercial-NoDerivs License (CC-BY-NC-ND) permits use, distribution and reproduction in any medium, provided the original work is properly cited, is not used for commercial purposes and no modifications or adaptations are made. (see below)

Use by commercial "for-profit" organizations

Use of Wiley Open Access articles for commercial, promotional, or marketing purposes requires further explicit permission from Wiley and will be subject to a fee.

Further details can be found on Wiley Online Library http://olabout.wiley.com/WileyCDA/Section/id-410895.html

Permission to reproduce Chapter 4 in its entirety.

Location-Specific Study of Young Rabbit Femoral Cartilage by Quantitative μMRI and Polarized Light Microscopy

Syeda Batool, Mouhamad Hammami, Hannah Mantebea, more...

Show all authors

First Published March 19, 2022 | Research Article | Check for updates

https://doi.org/10.1177/19476035221085143

Article information

Article Information

Volume: 13 issue: 1,

Article first published online: March 19, 2022; Issue published: January 1, 2022

Received: May 23, 2021; Accepted: February 02, 2022

Syeda Batool[1], Mouhamad Hammami[1], Hannah Mantebea[1], Farid Badar[1], Yang Xia[1]

[1]Department of Physics, Center for Biomedical Research, Oakland University, Rochester, MI, USA

Corresponding Author:

Yang Xia, Department of Physics, Center for Biomedical Research, Oakland University, 244 Meadow Brook Road, Rochester, MI 48309, USA. Email: xia@oakland.edu

APPENDIX B

MATLAB CODE USED FOR THE STRAIN CALCULATIONS IN CHAPTER FIVE

```
%% Analysis of intra tissue strains with varying fiber orientation and FCD.
% Defining parameter
    Ny=101;                          % number of nodes
    D=0.001;                         %length of tissue 1 mm or 0.001 m
    dy=D/(Ny-1);
    for j = 1: Ny                    %y= depth.
        y(j)=(j-1) *dy;
    end
    t=zeros (Ny);
    E=zeros (Ny);
    tau=0.1*10^ (6);                 % applied stress
    K=1.380649*10^ (-23);            % Boltzmann constant j/k
    T=293;                           % 293 K, Room Temperature
    % Define angle
    for j=1: Ny
        t(j) = pi/4*(tanh((y(j)-(.0003))/.00009) +1.0);
        % t(j) =0;
    end
    % Depth dependent intrinsic stiffness of collagen fibers
    for j =1: Ny
        mu0 = (0.4*10^6);
        mu1 = (0.08*10^6) *exp(y(j)/0.00099);
        mu(j) = mu0+mu1*sin(t(j)). ^4;
        % mu(j) = mu0;               % for homogenous case
    end
    % Depth dependent concentration of FCD/GAG
```

```
C0=9.57*10^25;      % Surface GAG 40 mg/ml (wet weight), converted in to 'no
                    of particles/m^3'
for j = 1: Ny
        C(j)=C0*exp(y(j)/.0009)      %r = 0.0009.
        % C(j)=C0;                  % for homogenous case
end
% Pre-strain
for j = 1: Ny
        E(j)=0.5*(-1+sqrt(1+(4*C(j)*(K)*(T)/mu(j))));
end
% Calculation of intra-tissue strain e
for j = 1: Ny
        e(j)=(E(j)/(1+E(j))) +(0.5/(1+E(j))) *(1+(tau/mu(j))-sqrt((1-
        (tau/mu(j))).^2+4*E(j)*(1+E(j))));
end
%Calculation of displacements
for j=Ny: -1:2
        u(Ny)=0;
        u(j-1) =u(j)-dy.*e(j);
end
%figure;
%plot(y,e,'-*');
%title('Intra-Tissue Strain ')
%xlabel('Displacement (m)')
%ylabel('Strain')
%figure;
%plot(y,u)
%title('Intra-Tissue Displacement')
%xlabel('Displacement (m)')
%ylabel('Intra-Tissue Displacement(m)')
```

```
%%% Fig 5.3 (Phase diagram)
% Define parameters
tau=0.2*10^ (6);
K=1.380649*10^ (-23);
T=293;
C =0.2*10^23:2*10^23:2*10^26;
mu =0.1*10^6:0.001*10^6:1.099*10^6;
for i=1: length(C)
for j =1: length(mu)
                    E(i,j)=0.5*(1+sqrt(1+((4.*C(i).*K*T)./mu(j))));
    e(i,j)=(E(i,j)./(1+E(i,j)))+(0.5./(1+E(i,j)))*(1+(tau./mu(j))-sqrt((1-
`(tau./mu(j))).^2+4*E(i,j).*(1+E(i,j))));
    end
end
figure;
mesh(C,mu,e);
xlabel('FCD')
ylabel('μ')
zlabel('Strain')
%%%% END %%%%
```

```
%% Fig 5.3 (Phase diagram)
% Define parameters
tau=0.2*10^ (6);
K=1.380649*10^ (-23);
T=293;
C =0.2*10^23:2*10^23:2*10^26;
mu =0.1*10^6:0.001*10^6:1.099*10^6;
for i=1: length(C)
        for j =1: length(mu)
                E(i,j)=0.5*(1+sqrt(1+((4.*C(i).*K*T)./mu(j))));
                e(i,j)=(E(i,j)./(1+E(i,j)))+(0.5./(1+E(i,j)))*(1+(tau./mu(j))-sqrt((1-
        (tau./mu(j))).^2+4*E(i,j).*(1+E(i,j))));
        end
end
figure;
mesh(C,mu,e);
xlabel('FCD')
ylabel('μ')
zlabel('Strain')
```

REFERENCES

Alhadlaq, H. A., & Xia, Y. (2005). Modifications of orientational dependence of microscopic magnetic resonance imaging T2 anisotropy in compressed articular cartilage. *Journal of Magnetic Resonance Imaging, 22*(5), 665–673.

Alhadlaq, H. A., Xia, Y., Hansen, F. M., Les, C. M., & Lust, G. (2007). Morphological changes in articular cartilage due to static compression: Polarized light microscopy study. *Connective Tissue Research, 48*(2), 76–84. https://doi.org/10.1080/03008200601130950

Alhadlaq, H. A., Xia, Y., Moody, J. B., & Matyas, J. R. (2004). Detecting structural changes in early experimental osteoarthritis of tibial cartilage by microscopic magnetic resonance imaging and polarised light microscopy. *Annals of the Rheumatic Diseases, 63*(6), 709–717. https://doi.org/10.1136/ard.2003.011783

Antipova, O., & Orgel, J. P. R. O. (2010). In situ d-periodic molecular structure of type ii collagen. *The Journal of Biological Chemistry, 285*(10), 7087–7096. https://doi.org/10.1074/jbc.M109.060400

Arzi, B., Wisner, E. R., Huey, D. J., Kass, P. H., Hu, J., & Athanasiou, K. A. (2011). Naturally-occurring osteoarthritis in the domestic rabbit: Possible implications for bioengineering research. *Lab Animal, 41*(1), 20–25. https://doi.org/10.1038/laban0112-20

Aspden, R. M., & Hukins, D. W. (1981). Collagen organization in articular cartilage, determined by X-ray diffraction, and its relationship to tissue function. *Proceedings of the Royal Society of London*. *Series B, Biological Sciences, 212*(1188), 299–304. https://doi.org/10.1098/rspb.1981.0040

Ateshian, G. A. (2009). The role of interstitial fluid pressurization in articular cartilage lubrication. *Journal of Biomechanics, 42*(9), 1163–1176. https://doi.org/10.1016/j.jbiomech.2009.04.040

Ateshian, G. A., Chahine, N. O., Basalo, I. M., & Hung, C. T. (2004). The correspondence between equilibrium biphasic and triphasic material properties in mixture models of articular cartilage. *Journal of Biomechanics, 37*(3), 391–400.

Ateshian, G. A., Lai, W. M., Zhu, W. B., & Mow, V. C. (1994). An asymptotic solution for the contact of two biphasic cartilage layers. *Journal of Biomechanics, 27*(11), 1347–1360. https://doi.org/10.1016/0021-9290(94)90044-2

Ateshian, G. A., & Wang, H. (1995). A theoretical solution for the frictionless rolling contact of cylindrical biphasic articular cartilage layers. *Journal of Biomechanics, 28*(11), 1341–1355. https://doi.org/10.1016/0021-9290(95)00008-6

Bashir, A., Gray, M. L., & Burstein, D. (1996). Gd-DTPA^{2-} as a measure of cartilage degradation. *Magnetic Resonance in Medicine, 36*(5), 665–673. https://doi.org/10.1002/mrm.1910360504

Basser, P. J., Schneiderman, R., Bank, R. A., Wachtel, E., & Maroudas, A. (1998). Mechanical properties of the collagen network in human articular cartilage as measured by osmotic stress technique. *Archives of Biochemistry and Biophysics, 351*(2), 207–219. https://doi.org/10.1006/abbi.1997.0507

Batiste, D. L., Kirkley, A., & Laverty, S. (2004). Ex vivo characterization of articular cartilage and bone lesions in a rabbit ACL transection model of osteoarthritis using MRI and micro-CT. *Osteoarthritis Cartilage, 12,* 986–996.

Batool, S., Hammami, M., Mantebea, H., Badar, F., & Xia, Y. (2022). Location-specific study of young rabbit femoral cartilage by quantitative μMRI and polarized light microscopy. *Cartilage, 13*(1), 19476035221085144. https://doi.org/10.1177/19476035221085143

Batool, S., Mahar, R., Badar, F., Tetmeyer, A., & Xia, Y. (2020). Quantitative μMRI and PLM study of rabbit humeral and femoral head cartilage at sub-10 μm resolutions. *Journal of Orthopaedic Research, 38*(5), 1052–1062.

Baum, T., Joseph, G. B., Karampinos, D. C., Jungmann, P. M., Link, T. M., & Bauer, J. S. (2013). Cartilage and meniscal T2 relaxation time as non-invasive biomarker for knee osteoarthritis and cartilage repair procedures. *Osteoarthritis and Cartilage, 21*(10), 1474–1484. https://doi.org/10.1016/j.joca.2013.07.012

Bendele, A. M. (2001). Animal models of osteoarthritis. *Journal of Musculoskeletal & Neuronal Interactions, 1*(4), 363–376.

Benninghoff, A. (1925). Form und bau der gelenkknorpel in ihren beziehungen zur funktion. *Zeitschrift Fr Zellforschung Und Mikroskopische Anatomie, 2*, 783–862. https://doi.org/10.1007/BF00583443

Bergholt, M. S., St-Pierre, J.-P., Offeddu, G. S., Parmar, P. A., Albro, M. B., Puetzer, J. L., Oyen, M. L., & Stevens, M. M. (2016). Raman spectroscopy reveals new insights into the zonal organization of native and tissue-engineered articular cartilage. *ACS Central Science, 2*(12), 885–895. https://doi.org/10.1021/acscentsci.6b00222

Bland, Y. S., & Ashhurst, D. E. (1996). Development and ageing of the articular cartilage of the rabbit knee joint: Distribution of the fibrillar collagens. *Anatomy and Embryology, 194*(6), 607–619. https://doi.org/10.1007/BF00187473

Bloch, F. (1946). Nuclear induction. *Physical Review, 70*(7–8), 460–474. https://doi.org/10.1103/PhysRev.70.460

Bloch, F. (1953). The principle of nuclear induction. *Science (New York, N.Y.), 118*(3068), 425–430. https://doi.org/10.1126/science.118.3068.425

Bone and Joint Burden. (n.d.). The burden of musculoskeletal diseases in the United States (4th ed.). Retrieved October 5, 2022, from https://www.boneandjointburden.org/fourth-edition

Borrelli, J., Jr., Silva, M. J., & Zaegel, M. A. (2009). Single high-energy impact load causes posttraumatic OA in young rabbits via a decrease in cellular metabolism. *Journal Orthop Res, 27*, 347–352.

Brama, P. A., Tekoppele, J. M., Bank, R. A., Karssenberg, D., Barneveld, A., & Weeren, P. R. V. (2000a). Topographical mapping of biochemical properties of articular cartilage in the equine fetlock joint. *Equine Veterinary Journal, 32*(1), 19–26. https://doi.org/10.2746/042516400777612062

Brama, P. A., Tekoppele, J. M., Bank, R. A., Barneveld, A., & van Weeren, P. R. (2000b). Functional adaptation of equine articular cartilage: The formation of regional biochemical characteristics up to age one year. *Equine Veterinary Journal, 32*(3), 217–221. https://doi.org/10.2746/042516400776563626

Briant, P., Bevill, S., & Andriacchi, T. (2015). Cartilage strain distributions are different under the same load in the central and peripheral tibial plateau regions. *Journal of Biomechanical Engineering, 137(*12), 1210091–1210097. https://doi.org/10.1115/1.4031849

Broom, N. D., & Silyn-Roberts, H. (1990). Collagen-collagen versus collagen-proteoglycan interactions in the determination of cartilage strength. *Arthritis & Rheumatism, 33*(10), 1512–1517. https://doi.org/10.1002/art.1780331008

Buckwalter, J. A., & Mankin, H. J. (1998a). Articular cartilage: Degeneration and osteoarthritis, repair, regeneration, and transplantation. *Instructional Course Lectures, 47*, 487–504.

Buckwalter, J. A., & Mankin, H. J. (1998b). Articular cartilage: Tissue design and chondrocyte-matrix interactions. *Instructional Course Lectures, 47,* 477–486.

Buckwalter, J. A., Mankin, H. J., & Grodzinsky, A. J. (2005). Articular cartilage and osteoarthritis. *Instructional Course Lectures, 54*, 465–480.

Burr, D. B. (2002). The contribution of the organic matrix to bone's material properties. *Bone, 31,* 8–11.

Bydder, M., Rahal, A., Fullerton, G. D., & Bydder, G. M. (2007). The magic angle effect: A source of artifact, determinant of image contrast, and technique for imaging. *Journal of Magnetic Resonance Imaging, 25*(2), 290–300. https://doi.org/10.1002/jmri.20850

Calandruccio, R. A., & Gilmer, W. S. J. (1962). Proliferation, regeneration, and repair of articular cartilage of immature animals. *JBJS, 44*(3), 431–455.

Chahine, N. O., Wang, C. C.-B., Hung, C. T., & Ateshian, G. A. (2004). Anisotropic strain-dependent material properties of bovine articular cartilage in the transitional range from tension to compression. *Journal of Biomechanics, 37*(8), 1251–1261. https://doi.org/10.1016/j.jbiomech.2003.12.008

Chen, S. S., Falcovitz, Y. H., Schneiderman, R., Maroudas, A., & Sah, R. L. (2001a). Depth-dependent compressive properties of normal aged human femoral head articular cartilage: Relationship to fixed charge density. *Osteoarthritis and Cartilage, 9*(6), 561–569. https://doi.org/10.1053/joca.2001.0424

Choi, J. B., Youn, I., Cao, L., Leddy, H. A., Gilchrist, C. L., Setton, L. A., & Guilak, F. (2007). Zonal changes in the three-dimensional morphology of the chondron under compression: The relationship among cellular, pericellular, and extracellular deformation in articular cartilage. *Journal of Biomechanics, 40*(12), 2596–2603. https://doi.org/10.1016/j.jbiomech.2007.01.009

David-Vaudey, E., Ghosh, S., Ries, M., & Majumdar, S. (2004). T2 relaxation time measurements in osteoarthritis. *Magnetic Resonance Imaging, 22*(5), 673–682. https://doi.org/10.1016/j.mri.2004.01.071

Depalle, B., Qin, Z., Shefelbine, S. J., & Buehler, M. J. (2015). Influence of cross-link structure, density and mechanical properties in the mesoscale deformation mechanisms of collagen fibrils. *Journal of the Mechanical Behavior of Biomedical Materials, 52*, 1–13. https://doi.org/10.1016/j.jmbbm.2014.07.008

Duarte, A., Ruiz, A., Ferizi, U., Bencardino, J., Abramson, S. B., Samuels, J., Krasnokutsky-Samuels, S., & Raya, J. G. (2019). Diffusion tensor imaging of articular cartilage using a navigated radial imaging spin-echo diffusion (RAISED) sequence. *European Radiology, 29*(5), 2598–2607. https://doi.org/10.1007/s00330-018-5780-9

Duvvuri, U., Kudchodkar, S., Reddy, R., & Leigh, J. S. (2002). T1ρ relaxation can assess longitudinal proteoglycan loss from articular cartilage in vitro. *Osteoarthritis and Cartilage, 10*(11), 838–844. https://doi.org/10.1053/joca.2002.0826

Esteves, P. J., Abrantes, J., Baldauf, H.-M., BenMohamed, L., Chen, Y., Christensen, N., González-Gallego, J., Giacani, L., Hu, J., Kaplan, G., Keppler, O. T., Knight, K. L., Kong, X.-P., Lanning, D. K., Le Pendu, J., de Matos, A. L., Liu, J., Liu, S., Lopes, A. M., … Mage, R. (2018). The wide utility of rabbits as models of human diseases. *Experimental & Molecular Medicine, 50*(5), Article 5. https://doi.org/10.1038/s12276-018-0094-1

Eyre, D. R. (1991). The collagens of articular cartilage. *Seminars in Arthritis and Rheumatism, 21*(3 Suppl 2), 2–11. https://doi.org/10.1016/0049-0172(91)90035

Frenkel, S. R., Bradica, G., Brekke, J. H., Goldman, S. M., Ieska, K., Issack, P., Bong, M. R., Tian, H., Gokhale, J., Coutts, R. D., & Kronengold, R. T. (2005). Regeneration of articular cartilage: Evaluation of osteochondral defect repair in the rabbit using multiphasic implants. *Osteoarthritis and Cartilage, 13*(9), 798–807. https://doi.org/10.1016/j.joca.2005.04.018

Gannon, A., Nagel, T., Bell, A., Avery, N., & Kelly, D. (2015). Postnatal changes to the mechanical properties of articular cartilage are driven by the evolution of its collagen network. *European Cells and Materials, 29,* 105–123. https://doi.org/10.22203/eCM.v029a09

Institution for Health Metrics and Evaluation. (2023). *GBD results*. The University of Washington. Retrieved March 15, 2023, from https://vizhub.healthdata.org/gbd-results

Geethanath, S., Reddy, R., Konar, A., Ahmed, S. I., Sundaresan, R., Babu, R., & Venkatesan, R. (2013). Compressed sensing MRI: A review. *Critical Reviews in Biomedical Engineering, 41*, 183–204. https://doi.org/10.1615/CritRevBiomedEng.2014008058

Gottardi, R., Hansen, U., Raiteri, R., Loparic, M., Düggelin, M., Mathys, D., Friederich, N. F., Bruckner, P., & Stolz, M. (2016a). Supramolecular organization of collagen fibrils in healthy and osteoarthritic human knee and hip joint cartilage. *PLOS ONE, 11*(10), e0163552. https://doi.org/10.1371/journal.pone.0163552

Gregory, M. H., Capito, N., Kuroki, K., Stoker, A. M., Cook, J. L., & Sherman, S. L. (2012). A review of translational animal models for knee osteoarthritis. *Arthritis, 2012,* 764621. https://doi.org/10.1155/2012/764621

Guterl, C. C., Hung, C. T., & Ateshian, G. A. (2010). Electrostatic and non-electrostatic contributions of proteoglycans to the compressive equilibrium modulus of bovine articular cartilage. *Journal of Biomechanics, 43*(7), 1343–1350. https://doi.org/10.1016/j.jbiomech.2010.01.021

Haase, A., Brandl, M., & Kuchenbrod, E. (1993). Magnetization-prepared NMR microscopy. *J Magn Reson A, 105,* 230–233.

Han, E., Chen, S. S., Klisch, S. M., & Sah, R. L. (2011). Contribution of proteoglycan osmotic swelling pressure to the compressive properties of articular cartilage. *Biophysical Journal, 101*(4), 916–924. https://doi.org/10.1016/j.bpj.2011.07.006

Hänninen, N. E., Nykänen, O., Prakash, M., Hanni, M., Nieminen, M. T., & Nissi, M. J. (2021). Orientation anisotropy of quantitative MRI parameters in degenerated human articular cartilage. *Journal of Orthopaedic Research, 39*(4), 861–870. https://doi.org/10.1002/jor.24778

Heinemeier, K. M., Schjerling, P., Heinemeier, J., Møller, M. B., Krogsgaard, M. R., Grum-Schwensen, T., Petersen, M. M., & Kjaer, M. (2016). Radiocarbon dating reveals minimal collagen turnover in both healthy and osteoarthritic human

cartilage. *Science Translational Medicine, 8*(346), 346ra90. https://doi.org/10.1126/scitranslmed.aad8335

Heise, N., & Toledo, O. M. (1993). Age-related changes in glycosaminoglycan distribution in different anatomical sites on the surface of knee-joint articular cartilage in young rabbits. *Annals of Anatomy, 175*(1), 35–40. https://doi.org/10.1016/s0940-9602(11)80234-7

Horkay, F. (2012). Interactions of cartilage extracellular matrix macromolecules. *Journal of Polymer Science*. *Part B, Polymer Physics, 50*(24), 1699–1705. https://doi.org/10.1002/polb.23191

Hudelmaier, M., Glaser, C., Hohe, J., Englmeier, K.-H., Reiser, M., Putz, R., & Eckstein, F. (2001). Age-related changes in the morphology and deformational behavior of knee joint cartilage. *Arthritis & Rheumatism, 44*(11), 2556–2561. https://doi.org/10.1002/1529-0131(200111)44:11<2556::AID-ART436>3.0.CO;2-U

Hunziker, E. B., Michel, M., & Studer, D. (1997). Ultrastructure of adult human articular cartilage matrix after cryotechnical processing. *Microscopy Research and Technique, 37*(4), 271–284. https://doi.org/10.1002/(SICI)1097-0029(19970515)37:4<271::AID-JEMT3>3.0.CO;2-O

Inamdar, S. R., Barbieri, E., Terrill, N. J., Knight, M. M., & Gupta, H. S. (2019). Proteoglycan degradation mimics static compression by altering the natural gradients in fibrillar organisation in cartilage. *Acta Biomaterialia, 97*, 437–450. https://doi.org/10.1016/j.actbio.2019.07.055

Isaksson, H., Harjula, T., Koistinen, A., Iivarinen, J., Seppänen, K., Arokoski, J. P. A., Brama, P. A., Jurvelin, J. S., & Helminen, H. J. (2010). Collagen and mineral deposition in rabbit cortical bone during maturation and growth: Effects on tissue properties. *Journal of Orthopaedic Research, 28*(12), 1626–1633. https://doi.org/10.1002/jor.21186

Jeffrey, D. R., & Watt, I. (2003). Imaging hyaline cartilage. *The British Journal of Radiology, 76*(911), 777–787. https://doi.org/10.1259/bjr/51504520

Julkunen, P., Harjula, T., Iivarinen, J., Marjanen, J., Seppänen, K., Närhi, T., Arokoski, J., Lammi, M. J., Brama, P. A., Jurvelin, J. S., & Helminen, H. J. (2009). Biomechanical, biochemical and structural correlations in immature and mature rabbit articular cartilage. *Osteoarthritis and Cartilage, 17*(12), 1628–1638. https://doi.org/10.1016/j.joca.2009.07.002

Julkunen, P., Iivarinen, J., Brama, P. A., Arokoski, J., Jurvelin, J. S., & Helminen, H. J. (2010). Maturation of collagen fibril network structure in tibial and femoral cartilage of rabbits. *Osteoarthritis and Cartilage, 18*(3), 406–415. https://doi.org/10.1016/j.joca.2009.11.007

Julkunen, P., Wilson, W., Isaksson, H., Jurvelin, J., Herzog, W., & Korhonen, R. (2013). A review of the combination of experimental measurements and fibril-reinforced modeling for investigation of articular cartilage and chondrocyte response to loading. *Computational and Mathematical Methods in Medicine, 2013, 326150*. https://doi.org/10.1155/2013/326150

Kääb, M. J., Ito, K., Clark, J. M., & Nötzli, H. P. (1998). Deformation of articular cartilage collagen structure under static and cyclic loading. *Journal of Orthopaedic Research, 16*(6), 743–751. https://doi.org/10.1002/jor.1100160617

Kahn, D., Les, C., & Xia, Y. (2015). Effects of cryopreservation on the depth-dependent elastic modulus in articular cartilage and implications for osteochondral grafting. *Journal of Biomechanical Engineering, 137*(5), 054502. https://doi.org/10.1115/1.4029182

Kavanagh, E., & Ashhurst, D. (1999). Developement and aging of the articular cartilage of the rabbit knee joint: Distribution of biglycan, decorin, and matrilin-1. *The Journal of Histochemistry & Cytochemistry, 47,* 1603–1615.

Kempson, G. (1991). Age-related changes in the tensile properties of human articular cartilage: A comparative study between the femoral head of the hip joint and the talus of the ankle joint. *Biochimica et Biophysica Acta*, *1075*, 223–230. https://doi.org/10.1016/0304-4165(91)90270-Q

Korhonen, R. K., Julkunen, P., Wilson, W., & Herzog, W. (2008). Importance of collagen orientation and depth-dependent fixed charge densities of cartilage on mechanical behavior of chondrocytes. *Journal of Biomechanical Engineering, 130*(2), 021003. https://doi.org/10.1115/1.2898725

Korhonen, R. K., Laasanen, M. S., Töyräs, J., Lappalainen, R., Helminen, H. J., & Jurvelin, J. S. (2003). Fibril reinforced poroelastic model predicts specifically mechanical behavior of normal, proteoglycan depleted and collagen degraded articular cartilage. *Journal of Biomechanics, 36*(9), 1373–1379. https://doi.org/10.1016/s0021-9290(03)00069-1

Kuettner, K. E. (1992). Biochemistry of articular cartilage in health and disease. *Clinical Biochemistry, 25*(3), 155–163. https://doi.org/10.1016/0009-9120(92)90224-G

Ladd, M. E., Bachert, P., Meyerspeer, M., Moser, E., Nagel, A. M., Norris, D. G., Schmitter, S., Speck, O., Straub, S., & Zaiss, M. (2018). Pros and cons of ultra-high-field MRI/MRS for human application. *Progress in Nuclear Magnetic Resonance Spectroscopy, 109,* 1–50. https://doi.org/10.1016/j.pnmrs.2018.06.001

Lai, W. M., Hou, J. S., & Mow, V. C. (1991). A triphasic theory for the swelling and deformation behaviors of articular cartilage. *Journal of Biomechanical Engineering, 113*(3), 245–258. https://doi.org/10.1115/1.2894880

Lammentausta, E., Kiviranta, P., Nissi, M. J., Laasanen, M. S., Kiviranta, I., Nieminen, M. T., & Jurvelin, J. S. (2006). T2 relaxation time and delayed gadolinium-enhanced MRI of cartilage (dGEMRIC) of human patellar cartilage at 1.5 T and 9.4 T: Relationships with tissue mechanical properties. *Journal of Orthopaedic Research, 2*4(3), 366–374. https://doi.org/10.1002/jor.20041

Lampropoulou-Adamidou, K., Lelovas, P., Karadimas, E. V., Liakou, C., Triantafillopoulos, I. K., Dontas, I., & Papaioannou, N. A. (2014). Useful animal models for the research of osteoarthritis. *European Journal of Orthopaedic Surgery & Traumatology: Orthopedie Traumatologie, 24*(3), 263–271. https://doi.org/10.1007/s00590-013-1205-2

Lee, J. H., Badar, F., Matyas, J., Qu, X., & Xia, Y. (2016). Topographical variations in zonal properties of canine tibial articular cartilage due to early osteoarthritis: A study using 7-T magnetic resonance imaging at microscopic resolution. *Magnetic Resonance Materials in Physics, Biology and Medicine, 29*(4), 681–690. https://doi.org/10.1007/s10334-016-0528-5

Lee, J. H., & Xia, Y. (2013). Quantitative zonal differentiation of articular cartilage by microscopic magnetic resonance imaging, polarized light microscopy, and Fourier-transform infrared imaging. *Microscopy Research and Technique, 76*(6), 625–632.

Lewis, P. N., Pinali, C., Young, R. D., Meek, K. M., Quantock, A. J., & Knupp, C. (2010). Structural interactions between collagen and proteoglycans are elucidated by three-dimensional electron tomography of bovine cornea. *Structure, 18*(2), 239–245. https://doi.org/10.1016/j.str.2009.11.013

Li, X., Benjamin Ma, C., Link, T. M., Castillo, D.-D., Blumenkrantz, G., Lozano, J., Carballido-Gamio, J., Ries, M., & Majumdar, S. (2007). In vivo T1ρ and T2 mapping of articular cartilage in osteoarthritis of the knee using 3T MRI. *Osteoarthritis and Cartilage, 15*(7), 789–797. https://doi.org/10.1016/j.joca.2007.01.011

Little, C. B., & Zaki, S. (2012). What constitutes an "animal model of osteoarthritis": The need for consensus? *Osteoarthritis and Cartilage, 20*(4), 261–267. https://doi.org/10.1016/j.joca.2012.01.017

Lyyra, T., Arokoski, J., Oksala, N., Vihko, A., Hyttinen, M., Jurvelin, J., & Kiviranta, I. (1999). Experimental validation of arthroscopic cartilage stiffness measurement using enzymatically degraded cartilage samples. *Physics in Medicine and Biology, 44,* 525–535. https://doi.org/10.1088/0031-9155/44/2/017

Madelin, G., Chang, G., Otazo, R., Jerschow, A., & Regatte, R. R. (2012). Compressed sensing sodium MRI of cartilage at 7T: Preliminary study. *Journal of Magnetic Resonance, 214*(1), 360–365. https://doi.org/10.1016/j.jmr.2011.12.005

Mahar, R., Batool, S., Badar, F., & Xia, Y. (2018). Quantitative measurement of T2, T1ρ and T1 relaxation times in articular cartilage and cartilage-bone interface by SE and UTE imaging at microscopic resolution. *Journal of Magnetic Resonance, 297,* 76–85. https://doi.org/10.1016/j.jmr.2018.10.008

Malda, J., Grauw, J. C. de, Benders, K. E. M., Kik, M. J. L., Lest, C. H. A. van de, Creemers, L. B., Dhert, W. J. A., & Weeren, P. R. van. (2013). Of mice, men and elephants: The relation between articular cartilage thickness and body mass. *PLOS ONE, 8*(2), e57683. https://doi.org/10.1371/journal.pone.0057683

Mankin, H. J. (1994, October 6). Chondrocyte transplantation: One answer to an old question (world) [Editorial]. *New England Journal of Medicine*, *331*(14):940–941. https://doi.org/10.1056/NEJM199410063311410

Mantebea, H., Batool, S., Singh, A., Hammami, M., Badar, F., & Xia, Y. (2022). Structural differences between immature and mature articular cartilage of rabbits by microscopic MRI and polarized light microscopy. *Journal of Anatomy.* 240(6), 1141–1151. https://doi.org/10.1111/joa.13620

Maroudas, A. (1968). Physicochemical properties of cartilage in the light of ion exchange theory. *Biophysical Journal, 8*(5), 575–595. https://doi.org/10.1016/S0006-3495(68)86509-9

Maroudas, A. (1970). Distribution and diffusion of solutes in articular cartilage. *Biophysical Journal, 10*(5), 365–379. https://doi.org/10.1016/S0006-3495(70)86307-X

Maroudas, A. (1975a). Biophysical chemistry of cartilaginous tissues with special reference to solute and fluid transport. *Biorheology, 12*(3–4), 233–248. https://doi.org/10.3233/bir-1975-123-416

Maroudas, A. (1975b). Glycosaminoglycan turn-over in articular cartilage. *Philosophical transactions of the Royal Society of London. Series B, Biological Sciences, 271*(912), 293–313. https://doi.org/10.1098/rstb.1975.0054

Maroudas, A. (1975c). Fluid transport in cartilage. *Annals of the Rheumatic Diseases, 34* Suppl 2, Suppl 77-81.

Maroudas, A., & Bannon, C. (1981). Measurement of swelling pressure in cartilage and comparison with the osmotic pressure of constituent proteoglycans. *Biorheology, 18(*3–6), 619–632. https://doi.org/10.3233/bir-1981-183-624

Maroudas, A., & Venn, M. (1977). Chemical composition and swelling of normal and osteoarthrotic femoral head cartilage II swelling. *Annals of the Rheumatic Diseases, 36*(5), 399–406. https://doi.org/10.1136/ard.36.5.399

Maroudas, A., Wachtel, E., Grushko, G., Katz, E. P., & Weinberg, P. (1991). The effect of osmotic and mechanical pressures on water partitioning in articular cartilage. *Biochimica Et Biophysica Acta, 1073*(2), 285–294. https://doi.org/10.1016/0304-4165(91)90133-2

Mattson, J. M., Turcotte, R., & Zhang, Y. (2017). Glycosaminoglycans contribute to extracellular matrix fiber recruitment and arterial wall mechanics. *Biomechanics and Modeling in Mechanobiology, 16*(1), 213–225. https://doi.org/10.1007/s10237-016-0811-4

Mark C van Turnhout, Henk Schipper, Bas Engel, Willem Buist, Sander Kranenbarg, Johan L van Leeuwen.. Postnatal development of collagen structure in ovine articular cartilage. *BMC Developmental Biology, 10*(1), 62.

McLeod, M. A., Wilusz, R. E., & Guilak, F. (2013). Depth-dependent anisotropy of the micromechanical properties of the extracellular and pericellular matrices of articular cartilage evaluated via atomic force microscopy. *Journal of Biomechanics, 46*(3), 586–592. https://doi.org/10.1016/j.jbiomech.2012.09.003

Mehta, S. B., Shribak, M., & Oldenbourg, R. (2013). Polarized light imaging of birefringence and diattenuation at high resolution and high sensitivity. *Journal of Optics, 15*(9), 094007.

Mittelstaedt, D., & Xia, Y. (2015). Depth-dependent glycosaminoglycan concentration in articular cartilage by quantitative contrast-enhanced micro–computed tomography. *CARTILAGE, 6*(4), 216–225. https://doi.org/10.1177/1947603515596418

Mlynárik, V., Trattnig, S., Huber, M., Zembsch, A., & Imhof, H. (1999). The role of relaxation times in monitoring proteoglycan depletion in articular cartilage. *Journal of Magnetic Resonance Imaging, 10*(4), 497–502. https://doi.org/10.1002/(SICI)1522-2586(199910)10:4<497::AID-JMRI1>3.0.CO;2-T

Moger, C. J., Arkill, K. P., Barrett, R., Bleuet, P., Ellis, R. E., Green, E. M., & Winlove, C. P. (2009). Cartilage collagen matrix reorientation and displacement in response to surface loading. *Journal of Biomechanical Engineering, 131*(3), 031008. https://doi.org/10.1115/1.3049478

Moo, E. K., Tanska, P., Federico, S., Al-Saffar, Y., Herzog, W., & Korhonen, R. K. (2021). Collagen fibres determine the crack morphology in articular cartilage. *Acta Biomaterialia, 126,* 301–314. https://doi.org/10.1016/j.actbio.2021.03.031

Mow, V. C., Kuei, S. C., Lai, W. M., & Armstrong, C. G. (1980). Biphasic creep and stress relaxation of articular cartilage in compression? Theory and experiments. *Journal of Biomechanical Engineering, 102*(1), 73–84. https://doi.org/10.1115/1.3138202

Mow, V. C., Wang, C. C., & Hung, C. T. (1999). The extracellular matrix, interstitial fluid and ions as a mechanical signal transducer in articular cartilage. *Osteoarthritis and Cartilage, 7*(1), 41–58. https://doi.org/10.1053/joca.1998.0161

Nancy Garrick, D. D. (2016, January 1). MRI findings reveal early changes to joint that predict development of knee osteoarthritis. *National Institute of Arthritis and Musculoskeletal and Skin Diseases.* https://www.niams.nih.gov/newsroom/spotlight-on-research/mri-findings-reveal-early-changes

National Health & Nutrition Examination Survey (NHANES). (n.d.). *National Institute of Environmental Health Sciences.* Retrieved October 5, 2022, from https://www.niehs.nih.gov/research/clinical/studies/nhanes/index.cfm

Nieminen, M. T., Rieppo, J., Töyräs, J., Hakumäki, J. M., Silvennoinen, J., Hyttinen, M. M., Helminen, H. J., & Jurvelin, J. S. (2001). T2 relaxation reveals spatial collagen architecture in articular cartilage: A comparative quantitative MRI and polarized light microscopic study. *Magnetic Resonance in Medicine, 46*(3), 487–493. https://doi.org/10.1002/mrm.1218

Nissi, M. J., Rieppo, J., Töyräs, J., Laasanen, M. S., Kiviranta, I., Nieminen, M. T., & Jurvelin, J. S. (2007). Estimation of mechanical properties of articular cartilage with MRI – dGEMRIC, T2 and T1 imaging in different species with variable stages of maturation. *Osteoarthritis and Cartilage, 15*(10), 1141–1148. https://doi.org/10.1016/j.joca.2007.03.018

OA Prevalence and Burden. (n.d.). *Osteoarthritis action alliance.* Retrieved October 5, 2022, from https://oaaction.unc.edu/oa-module/oa-prevalence-and-burden/.

Oldenbourg, R., & Mei, G. (1995). New polarized light microscope with precision universal compensator. *Journal of Microscopy, 180*(2), 140–147.

Owman, H., Tiderius, C. J., Neuman, P., Nyquist, F., & Dahlberg, L. E. (2008). Association between findings on delayed gadolinium-enhanced magnetic resonance imaging of cartilage and future knee osteoarthritis. *Arthritis & Rheumatism, 58*(6), 1727–1730. https://doi.org/10.1002/art.23459

Paatsama, S. (1992). *Ligament injuries in the canine stifle joint: A clinical and experimental study.* Dissertation. College of Veterinary Medicine.

Pandit, P., Rivoire, J., King, K., & Li, X. (2016). Accelerated T1ρ acquisition for knee cartilage quantification using compressed sensing and data-driven parallel imaging: A feasibility study. *Magnetic Resonance in Medicine, 75*(3), 1256–1261. https://doi.org/10.1002/mrm.25702

Peters, A. E., Akhtar, R., Comerford, E. J., & Bates, K. T. (2018). The effect of aging and osteoarthritis on the mechanical properties of cartilage and bone in the human knee joint. *Scientific Reports*, 8(1), 5931. https://doi.org/10.1038/s41598-018-24258-6

Pfeiffer, E., Vickers, S. M., Frank, E., Grodzinsky, A. J., & Spector, M. (2008). The effects of glycosaminoglycan content on the compressive modulus of cartilage engineered in type II collagen scaffolds. *Osteoarthritis and Cartilage, 16(*10), 1237–1244. https://doi.org/10.1016/j.joca.2008.02.014

Pierce, D. M., Ricken, T., & Holzapfel, G. A. (2013). A hyperelastic biphasic fibre-reinforced model of articular cartilage considering distributed collagen fibre orientations: Continuum basis, computational aspects and applications. *Computer Methods in Biomechanics and Biomedical Engineering, 16*(12), 1344–1361. https://doi.org/10.1080/10255842.2012.670854

Pond, M. J., & Nuki, G. (1973). Experimentally-induced osteoarthritis in the dog. *Annals of the Rheumatic Diseases, 32*(4), 387–388.

Poole, R., Blake, S., Buschmann, M., Goldring, S., Laverty, S., Lockwood, S., Matyas, J., McDougall, J., Pritzker, K., Rudolphi, K., Berg, W. van den, & Yaksh, T. (2010). Recommendations for the use of preclinical models in the study and treatment of osteoarthritis. *Osteoarthritis and Cartilage, 18,* S10–S16. https://doi.org/10.1016/j.joca.2010.05.027

Purcell, E. M., Torrey, H. C., & Pound, R. V. (1946). Resonance absorption by nuclear magnetic moments in a solid. *Physical Review*, *69*(1–2), 37–38. https://doi.org/10.1103/PhysRev.69.37

Quinn, T. M., Häuselmann, H.-J., Shintani, N., & Hunziker, E. B. (2013). Cell and matrix morphology in articular cartilage from adult human knee and ankle joints suggests depth-associated adaptations to biomechanical and anatomical roles. *Osteoarthritis and Cartilage, 21*(12), 1904–1912.

Reddy, S., Pedowitz, D. I., Parekh, S. G., Sennett, B. J., & Okereke, E. (2007). The morbidity associated with osteochondral harvest from asymptomatic knees for the treatment of osteochondral lesions of the talus. *The American Journal of Sports Medicine, 35*(1), 80–85. https://doi.org/10.1177/0363546506290986

Rieppo, J., Hyttinen, M. M., Halmesmaki, E., Ruotsalainen, H., Vasara, A., Kiviranta, I., Jurvelin, J. S., & Helminen, H. J. (2009). Changes in spatial collagen content and collagen network architecture in porcine articular cartilage during growth and maturation. *Osteoarthritis and Cartilage, 17*(4), 448–455. https://doi.org/10.1016/j.joca.2008.09.004

Risch, M., Easley, J. T., McCready, E. G., Troyer, K. L., Johnson, J. W., Gadomski, B. C., McGilvray, K. C., Kisiday, J. D., & Nelson, B. B. (2021). Mechanical, biochemical, and morphological topography of ovine knee cartilage. *Journal of Orthopaedic Research*, *39*(4), 780–787. https://doi.org/10.1002/jor.24835

Römgens, A. M., van Donkelaar, C. C., & Ito, K. (2013). Contribution of collagen fibers to the compressive stiffness of cartilaginous tissues. *Biomechanics and Modeling in Mechanobiology, 12*(6), 1221–1231. https://doi.org/10.1007/s10237-013-0477-0

Roughley, P. J., & Mort, J. S. (2014). The role of aggrecan in normal and osteoarthritic cartilage. *Journal of Experimental Orthopaedics, 1, 8.* https://doi.org/10.1186/s40634-014-0008-7

Roth, V., & Mow, V. C. (1980). The intrinsic tensile behavior of the matrix of bovine articular cartilage and its variation with age. *The Journal of Bone and Joint Surgery. American Volume*, *62*(7), 1102–1117.

Rubenstein, J. D., Kim, J. K., Morova-Protzner, I., Stanchev, P. L., & Henkelman, R. M. (1993). Effects of collagen orientation on MR imaging characteristics of bovine articular cartilage. *Radiology, 188*(1), 219–226. https://doi.org/10.1148/radiology.188.1.8511302

Sah, R. L., Yang, A. S., Chen, A. C., Hant, J. J., Halili, R. B., Yoshioka, M., Amiel, D., & Coutts, R. D. (1997). Physical properties of rabbit articular cartilage after transection of the anterior cruciate ligament. *Journal of Orthopaedic Research, 15*(2), 197–203. https://doi.org/10.1002/jor.1100150207.

Schinagl, R. M., Ting, M. K., Price, J. H., & Sah, R. L. (1996). Video microscopy to quantitate the inhomogeneous equilibrium strain within articular cartilage during confined compression. *Annals of Biomedical Engineering, 24*(4), 500–512. https://doi.org/10.1007/BF02648112

Schwartz, M. H., Leo, P. H., & Lewis, J. L. (1994). A microstructural model for the elastic response of articular cartilage. *Journal of Biomechanics, 27*(7), 865–873. https://doi.org/10.1016/0021-9290(94)90259-3

Setton, L. A., Elliott, D. M., & Mow, V. C. (1999). Altered mechanics of cartilage with osteoarthritis: Human osteoarthritis and an experimental model of joint degeneration. *Osteoarthritis and Cartilage, 7*(1), 2–14. https://doi.org/10.1053/joca.1998.0170

Shapiro, E. M., Borthakur, A., Gougoutas, A., & Reddy, R. (2002). 23Na MRI Accurately Measures Fixed Charge Density in Articular Cartilage. *Magnetic Resonance in Medicine, 47*(2), 284–291.

Smith, D. W., Gardiner, B. S., Davidson, J. B., & Grodzinsky, A. J. (2016). Computational model for the analysis of cartilage and cartilage tissue constructs. *Journal of Tissue Engineering and Regenerative Medicine, 10*(4), 334–347. https://doi.org/10.1002/term.1751

Sophia Fox, A. J., Bedi, A., & Rodeo, S. A. (2009). The basic science of articular cartilage. *Sports Health, 1*(6), 461–468. https://doi.org/10.1177/1941738109350438

Soulhat, J., Buschmann, M. D., & Shirazi-Adl, A. (1999). A fibril-network-reinforced biphasic model of cartilage in unconfined compression. *Journal of Biomechanical Engineering, 121*(3), 340–347. https://doi.org/10.1115/1.2798330

Stammers, M., Ivanova, I. M., Niewczas, I. S., Segonds-Pichon, A., Streeter, M., Spiegel, D. A., & Clark, J. (2020). Age-related changes in the physical properties, cross-linking, and glycation of collagen from mouse tail tendon. *The Journal of Biological Chemistry, 295*(31), 10562–10571. https://doi.org/10.1074/jbc.RA119.011031

Osteoarthritis Research Society International. (2015, April 13). *Standardization of osteoarthritis definitions.* https://oarsi.org/research/standardization-osteoarthritis-definitions

Institute for Health Metrics and Evaluation. *Osteoarthritis—Level 3 cause*. (2020, October 15). https://www.healthdata.org/results/gbd_summaries/2019/osteoarthritis-level-3-cause.

Thonar, E. J.-M. A., & Sweet, M. B. E. (1981). Maturation-related changes in proteoglycans of fetal articular cartilage. *Archives of Biochemistry and Biophysics, 208*(2), 535–547. https://doi.org/10.1016/0003-9861(81)90542-7

Torzilli, P. A., Deng, X.-H., & Ramcharan, M. (2006). Effect of compressive strain on cell viability in statically loaded articular cartilage. *Biomechanics and Modeling in Mechanobiology, 5*(2–3), 123–132. https://doi.org/10.1007/s10237-006-0030-5

Turunen, M. J., Saarakkala, S., & Rieppo, L. (2011). Comparison between infrared and Raman spectroscopic analysis of maturing rabbit cortical bone. *Appl Spectrosc, 65,* 595–603.

Vos, T., Lim, S. S., Abbafati, C., Abbas, K. M., Abbasi, M., Abbasifard, M., Abbasi-Kangevari, M., Abbastabar, H., Abd-Allah, F., Abdelalim, A., Abdollahi, M., Abdollahpour, I., Abolhassani, H., Aboyans, V., Abrams, E. M., Abreu, L. G., Abrigo, M. R. M., Abu-Raddad, L. J., Abushouk, A. I., … Murray, C. J. L. (2020). Global burden of 369 diseases and injuries in 204 countries and territories, 1990–2019: A systematic analysis for the Global Burden of Disease Study 2019. *The Lancet, 396*(10258), 1204–1222. https://doi.org/10.1016/S0140-6736(20)30925-9

Wakitani, S., Goto, T., Young, R. G., Mansour, J. M., Goldberg, V. M., & Caplan, A. I. (1998). Repair of large full-thickness articular cartilage defects with allograft articular chondrocytes embedded in a collagen gel. *Tissue Engineering, 4*(4), 429–444. https://doi.org/10.1089/ten.1998.4.429

Wang, C., Chahine, N. O., Hung, C. T., & Ateshian, G. (2003). Optical determination of anisotropic material properties of bovine articular cartilage in compression. *Journal of Biomechanics, 36*(3), 339–353.

Wang, C., Guo, X. E., Sun, D., Mow, V., Ateshian, G., & Hung, C. (2002). The functional environment of chondrocytes with cartilage subjected to compressive loading: A theoretical and experimental approach. *Biorheology, 39,* 11–25.

Wang, N., Kahn, D., Badar, F., & Xia, Y. (2015). Molecular origin of a loading-induced black layer in the deep region of articular cartilage at the magic angle. *Journal of Magnetic Resonance Imaging, 41*(5), 1281–1290. https://doi.org/10.1002/jmri.24658

Wang, N., & Xia, Y. (2011). Dependencies of multi-component T2 and T1ρ relaxation on the anisotropy of collagen fibrils in bovine nasal cartilage. *Journal of Magnetic Resonance, 212*(1), 124–132. https://doi.org/10.1016/j.jmr.2011.06.031

Wang, N., & Xia, Y. (2013). Anisotropic analysis of multi-component T2 and T1ρ relaxations in achilles tendon by NMR spectroscopy and microscopic MRI. *Journal of Magnetic Resonance Imaging, 38*(3), 625–633. https://doi.org/10.1002/jmri.24012

Wei, X., Gao, J., & Messner, K. (1997). Maturation-dependent repair of untreated osteochondral defects in the rabbit knee joint. *Journal of Biomedical Materials Research, 34*(1), 63–72. https://doi.org/10.1002/(sici)1097-4636(199701)34:1<63::aid-jbm9>3.0.co;2-l

Wijesinghe, D., & Roth, B. J. (2019). Mechanical bidomain model of cardiac muscle with unequal anisotropy ratios. *Physical Review E, 100*(6), 062417. https://doi.org/10.1103/PhysRevE.100.062417

Wilson, W., Huyghe, J. M., & van Donkelaar, C. C. (2007). Depth-dependent compressive equilibrium properties of articular cartilage explained by its composition. *Biomechanics and Modeling in Mechanobiology, 6*(1–2), 43–53. https://doi.org/10.1007/s10237-006-0044-z

Wilson, W., van Donkelaar, C. C., van Rietbergen, B., & Huiskes, R. (2005). A fibril-reinforced poroviscoelastic swelling model for articular cartilage. *Journal of Biomechanics, 38*(6), 1195–1204. https://doi.org/10.1016/j.jbiomech.2004.07.003

Wong, M. W. N., Qin, L., Lee, K. M., & Leung, K. S. (2009). Articular cartilage increases transition zone regeneration in bone-tendon junction healing. *Clinical Orthopaedics and Related Research, 467*(4), 1092–1100. https://doi.org/10.1007/s11999-008-0606-8

Xia, Y. (1997). Relaxation anisotropy in cartilage by microscopic MRI (μMRI) at 14 μm resolution. *The 5th Meeting of International Society of Magnetic Resonance in Medicine* (ISMRM), 339.

Xia, Y. (1998). Relaxation anisotropy in cartilage by NMR microscopy (μMRI) at 14-μm resolution. *Magnetic Resonance in Medicine, 39*(6), 941–949. https://doi.org/10.1002/mrm.1910390612

Xia, Y. (2000a). Heterogeneity of Cartilage Laminae in MR Imaging. *Journal of Magnetic Resonance Imaging, 11,* 686–693.

Xia, Y. (2000b). Magic-angle effect in magnetic resonance imaging of articular cartilage: A review. *Investigative Radiology, 35(*10), 602–621.

Xia, Y. (2007). Resolution 'scaling law' in MRI of articular cartilage. *Osteoarthritis and Cartilage, 15*(4), 363–365. https://doi.org/10.1016/j.joca.2006.12.004

Xia, Y. (2013). MRI of articular cartilage at microscopic resolution. *Bone & Joint Research, 2*(1), 9–17. https://doi.org/10.1302/2046-3758.21.2000135

Xia, Y., Alhadlaq, H., & Ramakrishnan, N. (2008). Molecular and morphological adaptations in compressed articular cartilage by polarized light microscopy and Fourier-transform infrared imaging. *Journal of Structural Biology, 164,* 88–95.

Xia, Y., & Momot, K. (2016). *Biophysics and Biochemistry of Cartilage by NMR and MRI.* Royal Society of Chemistry.

Xia, Y., Momot, K. I., Chen, Z., Chen, C. T., Kahn, D., & Badar, F. (2016). *Biophysics and Biochemistry of Cartilage by NMR and MRI*. Chapter 1: Introduction to cartilage, 1–43. https://doi.org/10.1039/9781782623663-00001

Xia, Y., Moody, J. B., & Alhadlaq, H. (2002). Orientational dependence of T2 relaxation in articular cartilage: A microscopic MRI (μMRI) study. *Magnetic Resonance in Medicine, 48*(3), 460–469.

Xia, Y., Moody, J. B., Alhadlaq, H., Burton-Wurster, N., & Lust, G. (2002). Characteristics of topographical heterogeneity of articular cartilage over the joint surface of a humeral head. *Osteoarthritis and Cartilage, 10*(5), 370–380.

Xia, Y., Moody, J. B., Alhadlaq, H., & Hu, J. (2003). Imaging the physical and morphological properties of a multi-zone young articular cartilage at microscopic resolution. *Journal of Magnetic Resonance Imaging, 17*(3), 365–374.

Xia, Y., Moody, J. B., Burton-Wurster, N., & Lust, G. (2001a). Quantitative in situ correlation between microscopic MRI and polarized light microscopy studies of articular cartilage. *Osteoarthritis and Cartilage, 9*(5), 393–406. https://doi.org/10.1053/joca.2000.0405

Xia, Y., Moody, J. B., Burton-Wurster, N., & Lust, G. (2001b). Quantitative in situ correlation between microscopic MRI and polarized light microscopy studies of articular cartilage. *Osteoarthritis and Cartilage, 9(*5), 393–406.

Xia, Y., Zheng, S., & Bidthanapally, A. (2008). Depth-dependent profiles of glycosaminoglycans in articular cartilage by μMRI and histochemistry. *Journal of Magnetic Resonance Imaging, 28*(1), 151–157. https://doi.org/10.1002/jmri.21392

Xia, Y., Zheng, S., Szarko, M., & Lee, J. (2012). Anisotropic properties of bovine nasal cartilage. *Microscopy Research and Technique, 75*(3), 300–306. https://doi.org/10.1002/jemt.21058

Yin, J.-H., Xia, Y., & Ramakrishnan, N. (2011). Depth-dependent anisotropy of proteoglycan in articular cartilage by fourier transform infrared imaging. *Vibrational Spectroscopy, 57*(2), 338–341. https://doi.org/10.1016/j.vibspec.2011.08.005

Zheng, S., & Xia, Y. (2009a). Multi-components of T2 relaxation in ex vivo cartilage and tendon. *Journal of Magnetic Resonance, 198,* 188–196.

Zheng, S., & Xia, Y. (2009b). The collagen fibril structure in the superficial zone of articular cartilage by μMRI. *Osteoarthritis Cartilage, 17,* 1519–1528.

Zheng, S., Xia, Y., & Badar, F. (2011). Further studies on the anisotropic distribution of collagen in articular cartilage by muMRI. *Magnetic Resonanc Medicine, 65,* 656–663.

Zheng, S., Xia, Y., Bidthanapally, A., Badar, F., Ilsar, I., & Duvoisin, N. (2009). Damages to the extracellular matrix in articular cartilage due to cryopreservation by microscopic magnetic resonance imaging and biochemistry. *Magnetic Resonance Imaging, 27*(5), 648–655. https://doi.org/10.1016/j.mri.2008.10.003